Title
A Study on Active/Passive Pneumatic Actuators for Assistive Systems

Author
Kaneishi, Daisuke

Publication Date
2019

Peer reviewed|Thesis/dissertation

A Study on Active/Passive Pneumatic Actuators for Assistive Systems

by

Daisuke Kaneishi

A dissertation submitted in partial satisfaction of the

requirements for the degree of

Doctor of Philosophy

in

Engineering - Mechanical Engineering

in the

Graduate Division

of the

University of California, Berkeley

Committee in charge:

Professor Masayoshi Tomizuka, Chair
Professor Roberto Horowitz
Professor Robert Full

Fall 2019

A Study on Active/Passive Pneumatic Actuators for Assistive Systems

Abstract

A Study on Active/Passive Pneumatic Actuators for Assistive Systems

by

Daisuke Kaneishi

Doctor of Philosophy in Engineering - Mechanical Engineering

University of California, Berkeley

Professor Masayoshi Tomizuka, Chair

The need for intelligent assistive devices is growing. Due to advances in medicine, people are living longer and able to recover from severe neurological incidents, resulting in an increased population with neuromuscular weakness. In workplaces such as assembly lines, there is a high possibility of work-related fatigue or injury, such as when workers squat down or lift their arms during their work tasks. Assistive devices could help remedy loss of strength on their extremities as well as keep the work environment safe and productive, allowing these growing segments of the population in need of the devices to live more self-sufficient, productive, and higher-quality lives.

In the design of assistive systems, an important design goal is prolonged operational time, which requires the minimum usage of energy. Energy consumption can be reduced by modifying the mechanical characteristics of assistive systems according to the dynamic characteristics of the human body, which vary considerably between tasks. This dissertation investigates 1) the design of actuators with adjustable mechanical impedance, 2) control strategies to search for, and adjust to, a suitable mechanical impedance for assistance and 3) sensing technologies for classifying the tasks in which the human engages.

The first part of this dissertation characterizes a pneumatic variable stiffness actuator named an Active/Passive Pneumatic Actuator (AP2A). The actuator consists of an air cylinder and an array of solenoid valves. These valves and the corresponding switching algorithms tune the chamber pressures and make the AP2A function as a mechanical spring with desired stiffness. The actuator has a low mechanical impedance compared to geared motors, which enables it to achieve efficient interaction. Control strategies of an assistive system with the AP2A are discussed in the second part. This control framework utilizes the characteristics of the AP2A to provide assistance when necessary and to operate transparently (i.e., neither to assist nor to disturb the users) otherwise. Energy consumed by the AP2A and the assisted system is minimized by solving an optimal control problem. Finally, an estimator is introduced to detect assistive timing for the assistive system

with the AP2A. This estimator utilizes physiological signals such as surface electromyogram and prior knowledge of a muscular model, classifying if the user is under the specified condition to be assisted by the AP2A. It demonstrates that the user's effort can be saved, also reducing the number of procedures to collect training data for the estimator before using assistive systems. The performance of the actuator, the controller, and the estimator proposed in this dissertation are verified through experiments.

From the above, this dissertation contributes to developing the AP2A that provides assistance and saves energy usage of assistive systems by working as a mechanical spring with stiffness optimized for achieving effective interaction under specific conditions. This actuator supports assistive devices that can be deployed in the real world, properly assisting the users when needed.

To Lily, George, Charlie,

my sister,
Yoshiko Kaneishi

and my parents
Rie and Masahiro Kaneishi

Contents

List of Figures

List of Tables

Acknowledgments

First of all, I would like to express my earnest gratitude and sincere respect to my research advisor, Professor Masayoshi Tomizuka. I am thankful for the guidance and patience to develop my knowledge about the research approach, control theories, and so forth. What I have studied under the guidance of you expanded my viewpoint and enhanced my abilities to work independently. I also would like to thank Ms. Miwako Tomizuka for your thoughtfulness and hospitality.

I am very grateful to Professor Roberto Horowitz, Professor Kameshwar Poolla, Professor Edward A. Lee, and Professor Robert Full for your willingness to serve as my dissertation committee and/or qualifying examination committee. I am also thankful for your insight on my research work and discussion in the courses to learn from your perspectives and methodologies. To Professor Ruzena Bajcsy, I am very grateful for the approval to work as one of the members of Human-Assistive Robotic Technologies (HART) laboratory. I am also grateful to Professor Hannah Stuart for the opportunity to work with Skye again.

Among all of my colleagues, I would like to give special thanks to Robert P. Matthew. I would not have been able to pursue my Ph.D. degree without your help and support. I am thankful for your kind words and sincere encouragement. I am impressed by your energetic engineering mind towards research and enjoyed sharing ideas with you. To Kevin Haninger, I am grateful for your elaborate feedback and support to improve my research work, including this dissertation. I am thankful to other Human-mechatronics group members, Wenlong Zhang, Junkai Lu, Changliu Liu, and Chen-Yu Chan, for your valuable advice on my research and so forth. I would like to thank Joel, Eric, Waiman, Shun, Katrina, Patrick, Elizabeth, Michael, and Bike for your help me with the research projects. To Jessica, Julia, and Drew, I am thankful for your support to proceed with the work we have done.

To members in Mechanical Control System (MSC) and HART laboratories, I am grateful for being part of my life in Berkeley. I was fortunate to join these laboratories and work with talented colleagues. To Yongxiang, Cheng, and Wei, thank you for your support from the first year. Thank you to my labmates in the MSC and HART lab: Cong, Yizhou, Liting, Victor, Chung-yen, Minghui, Alice, Te, Dennis, Yu, Hsien-Chung, Shuyang, Shiying, Sarah, Kiwoo, Zining, Jianyu, Laura, Yujiao, Chen, Jiachen, Yeping, Zhuo, Shiyu, Hengbo, Changhao, Yiyang, Grace, Mona, Lingfeng, Xinghao. I am grateful to all the other friends; especially to Shinya, Hyung-Taek, Kosuke, Taiki, Ryo, Takeshi, Fumika, Yuki, Hikaru, Yuya, Satoshi, Yasuyuki, Masafumi, and SMS softball members. I am also thankful to Susanne Kaspar and all the roommates for keeping me balanced throughout my Ph.D. life.

To the National Science Foundation and Funai Foundation for Information Technology, I gratefully acknowledge the financial support and the opportunity to pursue my interests through the exciting research project at the University of California, Berkeley.

Finally, I would like to express my gratitude and most profound love to my family, Yoshiko, Rie, and Masahiro Kaneishi.

Chapter 1

Introduction

1.1 Background

1.1.1 Demand for Assistive Devices

Among various types of assistive technologies, such as a pacemaker and an assistive listening device, the development of assistive devices to enhance motor function is becoming an important problem for a variety of reasons. One of the reasons is that, thanks to advanced medical technologies, death rates of diseases in the United States (US) have declined slowly; for example, age-standardized stroke death rates have declined by 38% among individuals over the age of 35 [1]. Accordingly, there are around 7 million stroke survivors in the US and 610,000 new stroke survivors every year [2]. There are approximately 288,000 people with spinal cord injury (SCI) living in the US; about 40% of the population has survived from vehicle crashes [3]. People with after-effects of stroke or SCI may suffer from motor paresis or hemiplegia which mostly limit their activities of daily living.

Another reason is the increase in the elderly population in the US, as age can be a risk factor for disabilities. We can assume longer average life expectancy in developed countries, owing to the advanced medical technologies as well as a high standard of living in an affluent society. Fig. 1.1 shows a trend of the number of elderly (65 years or older) in the US and the ratio of the number to the total population [4]. There are approximately 40 million individuals over the age of 65, and this number is assumed to increase by up to 85 million by 2050. Similar trends can be confirmed in other developed countries. For an extreme example, there will be approximately 40 million elderly in Japan by 2050, which is twice as large as the population in 2010 (Fig. 1.2) [5]. When the aging population increases, as suggested in the figures, it can be easily anticipated that the number of individuals with diseases will also increase.

Growing shortages of labor population can be an additional reason. The demographics in Fig. 1.1 and 1.2 indicate the decrease of the labor population in parallel with the increase of the aging population. These facts indicate that there may not be enough medical therapists and atten-

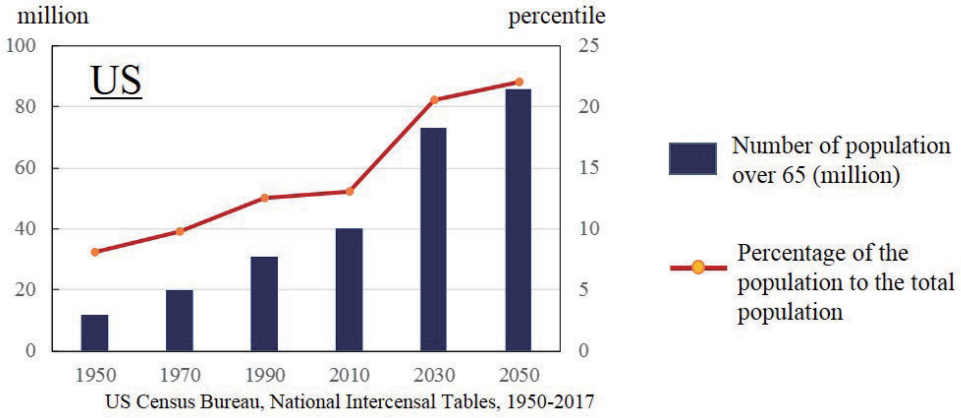

Figure 1.1: The number of elderly over 65 and the ratio to the total population in the US [4].

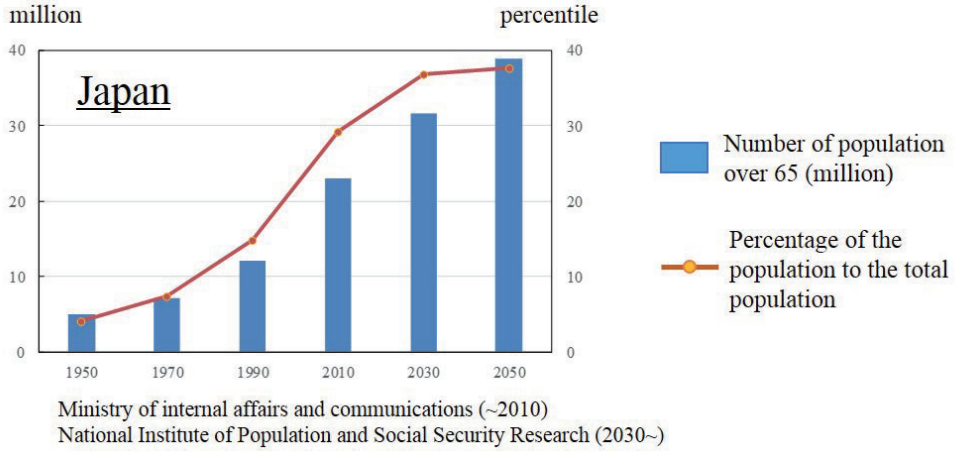

Figure 1.2: The number of elderly over 65 and the ratio to the total population in Japan [5].

dants regardless of the abilities of health care workers to provide the population with the required assistance. The elderly and people with disabilities may not be able to receive sufficient medical care in the near future, though the number of those individuals has been increasing.

National programs have accelerated in the 2000s [6], developing intelligent assistive technologies. These programs aim to help individuals with living longer through the continuing improvements in the medical technologies. Industrial companies also start introducing assistive devices in their factories (e.g., an assembly process) in the late 2010s. These devices have been used successfully to reduce the physical toll on employees and to keep the work environment safe and productive for the employees [7, 8]. Thus, the demand for physical assistive devices is growing more than ever before.

1.1.2 Modeling Intelligent Assistive Devices as Cyber-Physical Systems

One of the conventional approaches to build such assistive devices is to utilize robotic technologies. Numerous studies have been conducted for robotic therapies, smart prostheses, manipulation/mobility aids, including industrial applications [6, 9]. Fig. 1.3a and 1.3b show MIT-MANUS [10, 11] and Lokomat [12] that are well-known robotic therapy devices for the upper/lower-limbs. Aiming to replace part of physical work done by medical therapists, these devices have been used to assess the effects of robot-aided therapies on stroke/SCI patients' motor control and functional abilities (upper-limbs [13, 14], lower-limbs [15, 16]).

These intelligent assistive devices have common functions, while each device is specialized in specific tasks. Three main common functions are sensing environments, recognizing and deciding the next action based on the perceived results, and acting on the environment. Introducing ideas of the Cyber-Physical Systems (CPS, stemming from *Cybernetics* [17]), these three functions can be described as the *Cyber* part, which includes **Computational Platform** and **Network Fabric**. Fig. 1.4 shows a schematic diagram of the CPS. The computational platforms consist of sensors, computers, and actuators, and the network fabric connects those platforms (e.g., Network-based Gait Rehabilitation System [18]). The last component in Fig. 1.4, **Physical plant**, is the *Physical* part of the CPS, which includes environments (e.g., users of assistive devices) as well as hardware that is not realized by computers (e.g., mechanical parts/hardware designs of assistive devices).

From this point of view, the assistive devices are required to interact with the physical plant to address their assigned tasks. An ankle-foot prosthesis in Fig. 1.3c is aimed to provide a lower-limb amputee with sufficient mechanical power during walking. In Fig. 1.3d, a wheelchair mounted robotic arm, named iARM, is assumed to help the user with daily activities such as wearing accessories and drinking from a cup. These tasks are identical to design objectives in engineering study, specified elaborately in clear descriptions by using a *model* of the physical plant. The intelligent assistive devices are then designed based on the objectives and assessed according to how well their behavior match those models [21].

Fig. 1.5 shows one of the common models of the physical plant [22] implemented to intelligent assistive devices. The assistive devices are modeled as artificial movement control systems (AMCS) in the figure, which consist of a **controller**, an **actuator**, **sensors**, and controlled **plant**[1]. The actuator and sensors are modeled as physical interfaces sensing and acting on the physical plant. Human movement control systems (HMCS) expresses users of assistive devices. In the same way as the AMCS, the HMCS consists of the four components which correspond to the central nervous system, muscles, the physiological sensory systems, and the skeleton/passive tissues, respectively. The HMCS has an additional component called **parallel systems** (e.g., tongue, head), which model behavior generating *explicit* commands (i.e., discrete signals). The behavior includes pressing buttons [24], moving faces and eyes [25], and giving voice commands [26]. The intention may be estimated *implicitly* from physiological or kinesiological signals (i.e., continuous

[1]To distinguish the physical plant (Fig. 1.4) and the identical term in Fig. 1.5, the latter is called the *controlled* plant following [23].

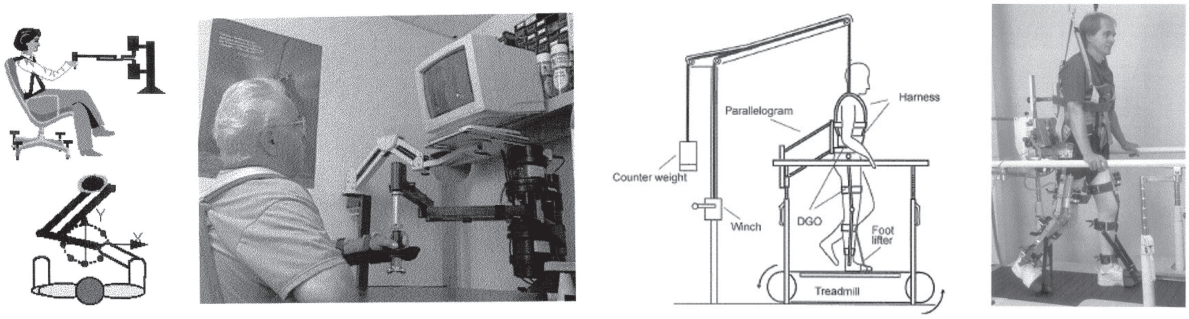

(a) Design of MIT-MANUS [13].

(b) Design of Lokomat [12].

(c) Design of a powered ankle-foot prosthesis [19].

(d) Examples of iARM usage [20].

Figure 1.3: Examples of robotic therapy devices, prostheses, and manipulation aids.

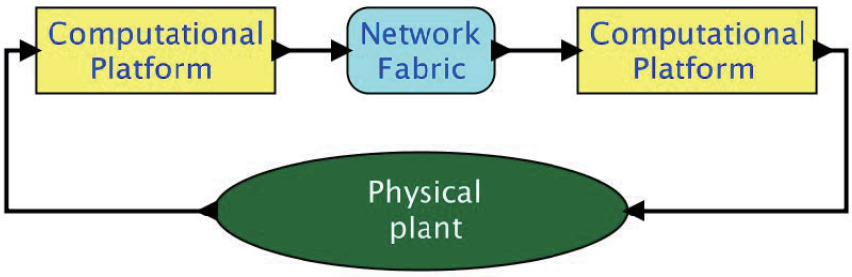

Figure 1.4: Schematic of the Cyber-Physical-System [21].

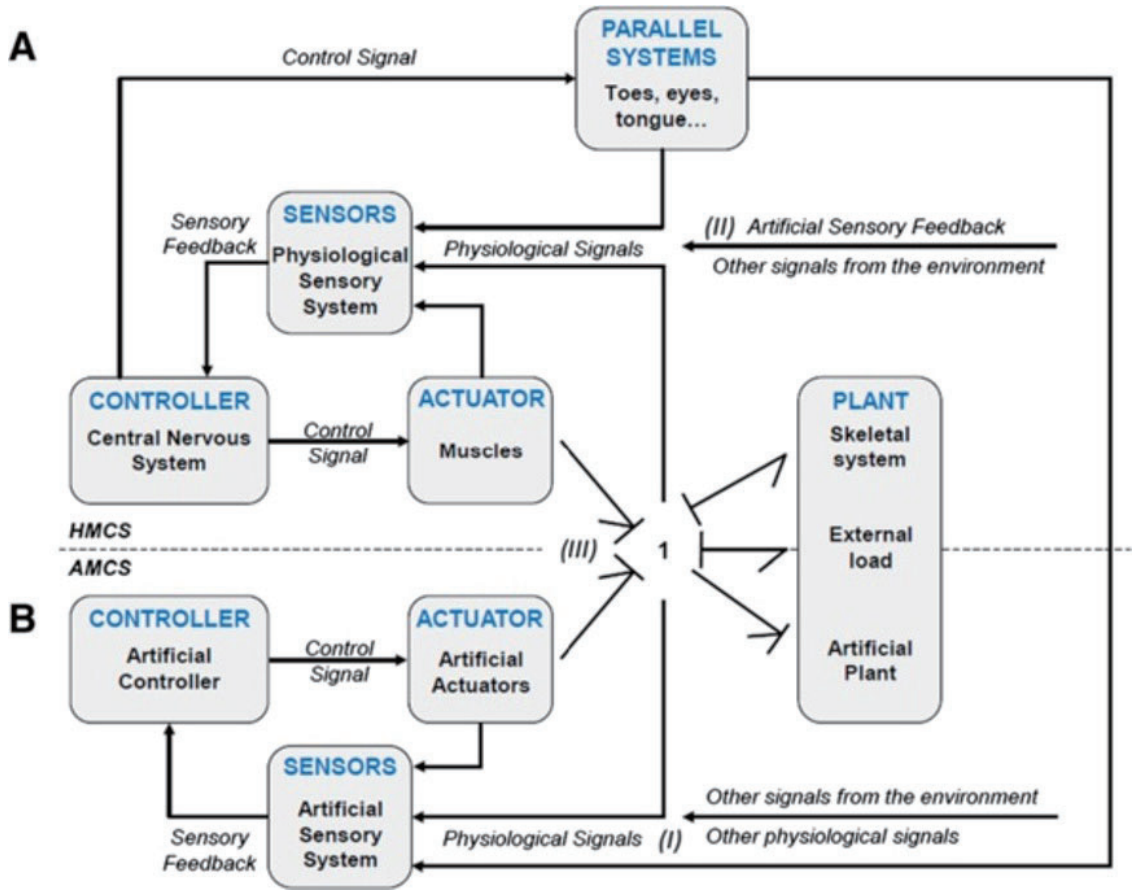

Figure 1.5: Model of (A)Human & (B)Artificial Movement Control Systems (HMCS/AMCS) [22].

bio-signals) related to the intention such as neural signals from the central nervous system (e.g., electroencephalogram (EEG) [27] and oxygenated hemoglobin [28]), activation of the muscles (e.g., electromyogram (EMG) [29]), and movements of the skeletal systems (e.g., joint angle [30] and angular velocity [31]). Characteristics of individuals, such as disabilities as well as high physical abilities, can be represented in one or several components of the HMCS. For example, disuse muscular atrophy may affect the actuator component, deafness may be described in the sensors component, and osteoporosis/limb deficiencies may be modeled in the controlled plant component. These models of the HMCS may be useful to select sensors, actuators, and controllers of the AMCS to satisfy the design objectives.

These two models, the AMCS and the HMCS, are connected with a representation of the bond graph (1-junction 5-port) [32]. Two bonds (i.e., arrows) from the two actuator components suggest that these actuators work as effort sources (i.e., force generators in mechanical systems). The **1**-junction represents that forces encountered at the junction are required to add to zero, and this junction becomes an effort source for the **Artificial Plant** in the controlled plant component. At

the same time, the 1-junction works as flow sources, which modifies velocities of **Skeletal system** and **External load** in the controlled plant component.

1.2 Motivation

1.2.1 Improvement of Energy Efficiency for Assistive Devices

Focusing on building the AMCS includes operational time, one of the critical information is missing in Fig. 1.5, energy efficiency. Robotic therapy devices in Fig. 1.3a and 1.3b are assumed to be utilized in medical facilities or laboratories, and they can be designed as large as possible. In those facilities, the devices can neglect energy efficiency with an assumption that the actuators can generate forces for an infinitely long period, as there are abundant power sources that can provide enough power to the devices. In terms of wearable assistive devices, such as exoskeletons, the size of power sources is limited due to its portability. Accordingly, the operational time of such assistive devices is generally limited due to the capacity of the power sources. This consideration may be supported by nominal operational time of current products that are at most 4 hours (e.g., HAL for well-being, single-joint type: 2 hours [33], ATOUN model Y: 4 hours [34]). The motivation of this study is thus improving the energy efficiency of intelligent, wearable assistive devices for daily activities.

1.2.2 Task Specific Assistance by Modification of Mechanical Characteristics

According to Fig. 1.5, one of the control techniques improving energy efficiency of the AMCS is to regulate a magnitude of control signals (i.e., forces) while producing enough work to satisfy the design objectives. This problem can be regarded as an optimal control problem and solved by a linear quadratic regulator (LQR) [35].

Another idea is to utilize interactions with the physical plant (i.e., taking 1-junction into consideration[2]) [37]. Studies with a biped [38] and hopping [39] robots have indicated that, during the interaction with the physical plants, consideration of mechanical characteristics of the AMCS could improve energy efficiency. In the case of intelligent assistive devices, they are required to cooperate with the users whose physical abilities determine the design objectives of the devices. *Assist-as-needed* control paradigms have been introduced to new assistive devices in the field of gait therapies as replacements for continuous assist control methods [40]. Researchers proposed the control paradigms, intending to encourage patients using their residual abilities efficiently. From the viewpoint of the actuator, compared to the continuous assistance control, the control paradigms save the amount of assistive force generated by the actuator and corresponding energy

[2]From the perspective of controller design, the Port-Hamiltonian approach [36] may be suitable to consider this problem.

consumption. The reason being that, with the control paradigms, the actuator is only required to offset a shortage of the user's force.

The assist-as-needed control paradigms are specialized for gait therapy/assistance, as gait is one of the most essential human behaviors[3] for independent living. The movement has been well investigated [44], and there exist mathematical models describing joint impedance of the HMCS during gait [45]. The assist-as-needed control paradigms utilize this knowledge of the HMCS and modify mechanical characteristics of the AMCS by controlling actuators implemented an impedance/admittance control scheme [46] or a vector field control scheme (path-control: [47], velocity-field: [48], force-field: [49]) for suitable assistance. Meanwhile, quasi-passive and passive exoskeletons have also been investigated for loaded and normal gait assistance, which could reduce the energy inputs (i.e., the metabolic cost of transport) of the HMCS. There were no actuators on the quasi-passive exoskeleton [50]. Moreover, the passive exoskeletons only consist of a mechanical system (i.e., a spring and a clutch) without power sources of the AMCS [51]. These findings suggest that, instead of controlling the mechanical impedance of the actuators, inherent mechanical characteristics of the quasi-passive and passive devices can be utilized for reducing the energy consumption of the HMCS. Energy consumed by the whole system may be reduced by selecting the devices with mechanical characteristics that are suitable for the specific task (i.e., gait). However, compared to the actuators, these passive devices necessitate a work for exchanging components in other tasks. Since the mechanical components have a limited operational range, these devices may hinder the users' performance if tasks are modified.

1.2.3 Technical Issues

The motivation of this study is to improve the energy efficiency of the AMCS for wearable assistive devices, which are supposed to assist daily activities. Daily activities are not limited to a single task, as upper-extremities are involved in many tasks in daily living, such as writing, opening door, and lifting objects. It is nearly impossible to develop a unique control law that improves the energy efficiency of the AMCS while supporting all of those activities (i.e., tasks), as the dynamic characteristics of the HMCS vary considerably between tasks. However, as stated in section 1.2.2, energy consumed by the AMCS, as well as the HMCS, may be reduced by tuning mechanical characteristics of the devices for each specific task to be assisted by the devices. It is conceivable that a control framework that integrates task-specific controllers along with a task classifier may improve the energy efficiency of the assistive devices.

This dissertation thus explored control strategies for the assistive devices in multi-tasks, both with variable dynamic characteristics. From the viewpoint of control, one of the challenges is to develop the control strategy to adapt appropriately to each task assigned by the user to ensure performance and safety. Another challenge is that the control strategy is required to detect transitions between these assigned and non-assigned tasks while all the tasks have their own unique dynamics

[3] Accordingly, biped robots have been developed since 1973 [41] and utilized to elucidate human gait mechanisms such as dynamics of passive walking [42, 43]

of the AMCS and HMCS. Above discussions inspire to develop the intelligent, wearable assistive devices for an elbow joint which address the following three technical issues:

- **Actuator** with low, variable mechanical impedance suitable for sensing of and reactions to transitions between tasks
- **Controller** to search and adjust to the suitable mechanical impedance of the assistive system including actuators for each task based on identification of the HMCS
- **Sensor & estimator** to extract features of the human movement, allowing for task identification and for tracking which tasks the user is currently performing

To approach these issues, a single-degree-of-freedom assistive device is designed to focus on the development of control strategies with the simplified AMCS and HMCS models. In particular, the effectiveness of assistance in an upper-extremity task (i.e., load-lifting) and transitions between the task and non-assigned tasks were investigated in this study.

1.3 Contributions

1.3.1 Actuator

Literature Review

When the world's first industrial robot (Unimate) emerged in the early 1960s, hydraulic and pneumatic actuators were utilized to manipulate heavy objects in factories. These actuators can produce a high power-to-weight ratio. However, the controlled plant includes non-linearity due to the characteristics of fluids. Thereafter an electrical servo motor was developed, which can produce high power similar to the hydraulic and pneumatic actuators. There are several advantages to replace the hydraulic actuators with servo motors. From the viewpoint of control, a controlled plant of the motor can be described as a linear system, which is a suitable application for classical control theory [52]. A reduction gear generally attached to the motor also enables engineers to model the controlled plant with ease [53]. The reason being that interactive forces/torques can be separated from the plant as disturbances due to its high mechanical impedance (i.e., non-backdrivablity).

The geared electrical motors have been widely utilized in assistive devices with well-designed mechanisms reducing the impedance gradually. A rotary series elastic actuator (RSEA), which is inspired by a series elastic actuator (SEA) shown in Fig. 1.6a [54], has been developed to avoid the expensive, solid system for physical human-robot interaction (pHRI) [55]. The RSEA enables to sense the interaction without a force sensor as well as adding inherent compliance to the geared motors (Fig. 1.6b). The SEA/RSEA is thus useful to compensate frictions in cable-driven systems by placing the springs close to the user [56, 57]. Further improvements have been made by designing Variable Impedance Actuators (VIAs) [58, 59, 60]. An additional control input (e.g., another geared motor in Fig. 1.6c [61]) to the system enables VIAs to control the assistive force as well as

the joint dynamics to assist their users [62]. Note that (quasi-)direct drive motors with a low gear ratio have also been investigated for assistive devices [63, 64].

Actuators are not limited to the motors. Soft/biomimetic robotics has become one of the major research topics in the field of assistive devices recently. In this field, pneumatic actuators attract attention again and have been actively investigated in place of the geared motors [65, 66]. In general, pneumatic actuators are lightweight, deliver high power output per unit mass, and have less inherent mechanical impedance compared to the motors. Pneumatic actuators can be classified into two types, soft-bodied actuators (e.g., Fig 1.6d) and the articulated soft actuators. A McKibben artificial muscle is one of the most popular soft-bodied actuators for assistive devices [67, 68]. An air cylinder is said to be one of articulated soft actuators, which has already been investigated as a variable stiffness actuator [69, 70].

Quasi-passive and passive components may be useful to modify the joint dynamics. Compared with those actively controlled actuators, these components ensure the safety (i.e., stability in this dissertation) of the system, as energy is not injected (i.e., just stored and dissipated) to the system by these devices. For example, springs or elastic bands are simple and have been used to develop a practical assistive device such as Wilmington Robotic EXoskeleton (WREX) shown in Fig. 1.7a [71]. These springs can be combined with transmission systems such as mechanical/electroadhesive clutches to achieve more complex assistance [51, 72]. A damper or a brake can be designed with magnetorheological (MR) fluids which change its behavior by modifying the magnetic field [73]. Comparing with active components, design parameters (e.g., stiffness of the spring) may become optimum only in confirmed situations. Once tasks are modified, these devices may hinder the users' performance since the mechanical elements have a limited operational range.

Contribution

Matthew et al. have investigated an Active/Passive EXoskeleton-α (APEX-α) [74], incorporating the merits of both active and passive components. As shown in Fig. 1.8, one three-port solenoid valve (V2) connects both chambers to either the pressure source or sink to control pressures to the desired values *actively*. The other two valves (V1) allow a pneumatic cylinder to be connected to V2 or sealed to maintain the amount of gas in each chamber. The sealed state can be maintained without any energy consumption for long-term operations, similar to the behavior of *passive* components. Besides, it was indicated that the sealed state with well-adjusted pressures could be utilized for augmenting the user's performance. However, kinetic parameters of the assistive device (e.g., assistive torque and joint stiffness of the APEX-α) were not taken into consideration in the prior study [74, 75].

Inspired by this actuator design, this dissertation introduces an Active/Passive Pneumatic Actuator (AP2A), which can be controlled as both *active* and *passive* components. The array of valves in Fig. 1.8 is modified to control pressures in each chamber separately. With these setups, the chamber pressures can be modified to work as a passive spring with controllable stiffness. Its characteristics are empirically evaluated and analyzed as a variable stiffness actuator in chapter 2.

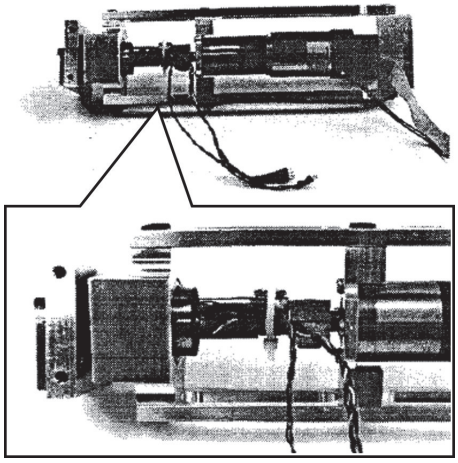

(a) Design of a SEA [54].

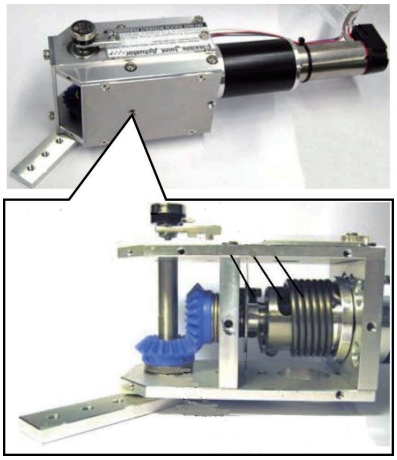

(b) Design of a RSEA [55].

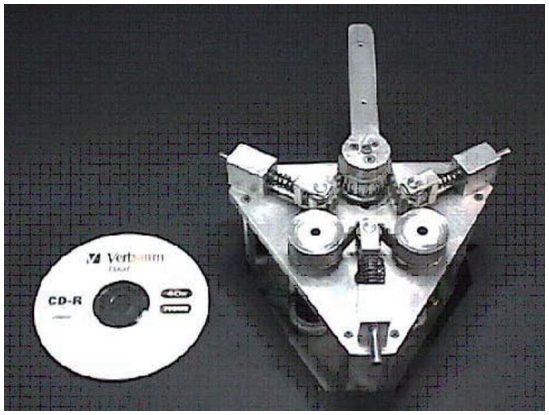

(c) Design of a VSA [61].

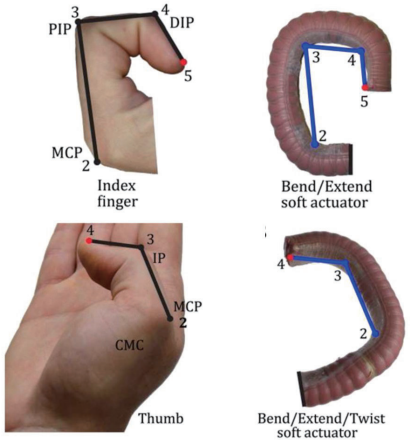

(d) Design of a soft pneumatic actuator [65].

Figure 1.6: Examples of actuators.

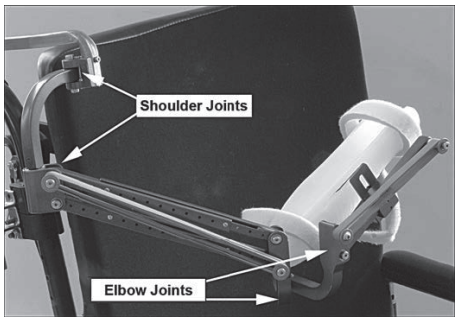

(a) Design of a WREX [71].

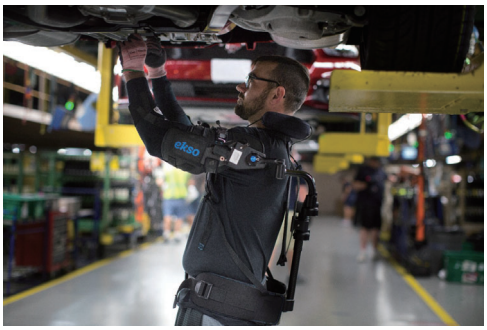

(b) Design of an EksoVest [7].

Figure 1.7: Examples of assistive devices with passive components.

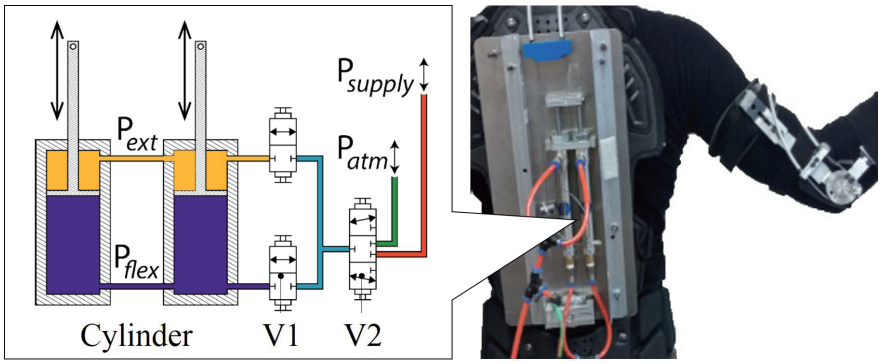

Figure 1.8: Design of an Active/Passive EXoskeleton-α (APEX-α) [74].

1.3.2 Controller

Literature Review

Fig. 1.9 shows an overview of typical force/torque controllers for assistive devices to modify the mechanical impedance. These controllers may serve as the controller component in Fig. 1.5. Though the force/torque controller is focused in the following paragraphs, a position controller can be utilized in a low-level controller. In such a case, the high-level controller can tune the admittance for assisting the user's motion [76], instead of controlling the impedance. Note that, comparing Fig. 1.9 with Fig. 1.5, $y, \hat{y}$ are assumed to be sensory feedback from the sensor component, and u is a control signal to the actuator, respectively. Many control frameworks utilize bio-signals y to infer the user's intention (e.g., a muscular force/joint torque in this paper) to achieve the desired assistance. An estimator can help the processing of y and re-design of sensory inputs $\hat{y}$ for the high-level controller if needed. Based on the bio-signals y and their derived estimates $\hat{y}$, the high-level controller designs a reference force/torque r for a low-level controller.

The design of the high-level controller is more dependent on applications compared with the estimator and the low-level controller. For power augmentation, the high-level controller can be a constant gain with a feed-forward compensator [77] to simply amplify the human torque. The controller can be designed to modify the sensitivity of the pHRI system by tuning its mechanical impedance [30, 31] (i.e., a relation between the user's torque and the joint velocity of the system). The mechanical impedance can be actively compensated according to load-side force [78] measured by a force sensor or mechanisms such as a SEA, and the impedance can be modified adaptively [79]. For rehabilitation, assist-as-needed controllers have been introduced as described in the prior section 1.2 [80, 81, 82]. One of these controllers, called a force-field controller [81], provides high impedance (i.e., sizable resistive force) only if the user deviates from the given desired motion during rehabilitation. In other words, it does not resist the user's motion when the user can successfully move according to the desired trajectory. An oscillator may be applied as a high-level controller according to the specific task [83, 84].

The controllers above are generally designed based on the HMCS models in Fig. 1.5. Re-

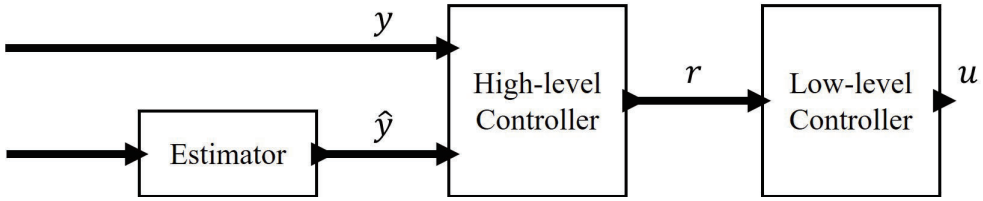

Figure 1.9: Overview of controller design for assistive devices.

cent studies suggest that the high-level controller can be designed with model-free, data scientific methods [85, 86, 87]. These methods utilize online empirical data of inputs (e.g., maximal oxygen consumption (VO2max) for $\hat{y}$) and outputs (e.g., assist torque for u), searching for the suitable control outputs to reduce a defined cost related to inputs through trial and error *efficiently*.

The control signal u in Fig. 1.9 is required at the actuator level to follow the desired trajectory r. A torque of DC motors can be controlled by tuning current inputs to the motor. Precise torque control can be achieved with a RSEA by rejecting effects caused by disturbances such as frictions of transmission cables [57]. For pneumatic actuators, nonlinear controllers have been developed to tune output forces with electrical valves [88, 89].

Contribution

This study introduces both a low-level controller of the AP2A stated in section 1.3.1 and a high-level controller. A low-level controller of the AP2A is introduced in chapter 2. The control law is designed based on a mathematical model of the AP2A as well as a model-free method. The control signal to the AP2A tunes the chamber pressures, and the actuator can start to function as a passive spring once both pressures reach the desired range.

The proposed high-level controller enables assistance only when necessary by switching between discrete modes (e.g., *no-assist* and *assist* mode). The high-level controllers developed in previous studies provide suitable assistance only for predefined scenarios. The assistance provided by the controllers may disturb the users' movement in different scenarios. With the proposed concept, when the users start to do other tasks that are beyond the scope of the *assist* mode, the controller can switch its control law by switching to the other mode to achieve transparent interaction (i.e., neither to assist nor disturb the users). Note that, with this concept, more than two discrete modes can be implemented in the high-level controller corresponding to the number of scenarios in which the user needs assistance (e.g., *assist* mode1: lifting objects, *assist* mode2: holding objects, *assist* mode3: opening a jar).

Fig. 1.10 shows a basic concept of the high-level controller for the two discrete modes. The dynamics f, the control laws of the device $\mathbf{u}$, and inputs from the user $\mathbf{d}$ are different in each discrete mode q. In each mode, different control laws $\mathbf{u}_1$ and $\mathbf{u}_2$ are implemented. The control law $\mathbf{u}_1$ in the *no-assist* mode q_1 can be designed as a zero-impedance controller, which enables the user to move the limbs without any resistive force as if there is no external device. Another

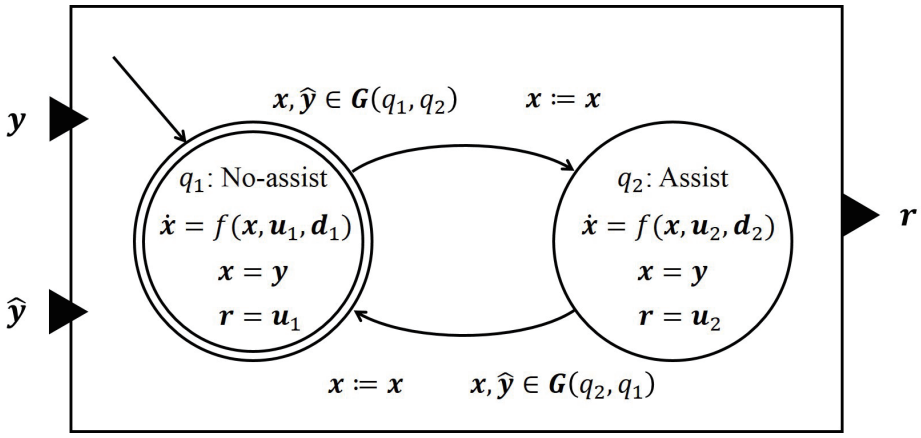

Figure 1.10: Proposed design of a high-level controller for assistive devices used in daily living.

control law $\mathbf{u}_2$ in the *assist* mode q_2 is optimized to a task in the specific scenario (e.g., a repetitive load-carrying task). The high-level controllers designed in prior work (e.g., [30]) can be utilized to design the control law $\mathbf{u}_2$ for suitable assistance. The output of the high-level controller is one of these control laws, and it becomes the reference $\mathbf{r}$ to the low-level controller in Fig. 1.9. A guard condition G in Fig. 1.10 contains inputs y and $\hat{y}$ as elements. The guard classifies the user's states based on the inputs if the user is performing the task or not. A transition occurs from *no-assist* mode to *assist* mode when the guard condition G associated with edges (q_1, q_2) is enabled, and vice versa. The state variables $\mathbf{x}$ are assumed to be measurable as sensory inputs $\mathbf{y}$ cover all the states $\mathbf{x}$.

This high-level controller design problem in Fig. 1.10 can then be broken down into two problems: design of the guard G associated with edges (q_1, q_2) and (q_2, q_1), and design of the control laws $\mathbf{u}_1$ and $\mathbf{u}_2$. Note that the motivation of this study is to develop an energy efficient assistive device that can be used in daily living. Therefore, these control laws $\mathbf{u}_1, \mathbf{u}_2$ need to be minimized with suitable system dynamics f and guard G that are related to the actuator design and the estimator, respectively. Given system dynamics and guard conditions, chapter 3 describes a computational method of the reference $\mathbf{r}$ which balances the competing goals of minimizing the energy consumption of the devices while maximizing the user assistance.

1.3.3 Sensor & Estimator

Literature Review

Physiological signals have been investigated to estimate human intention for assistive devices since the potential usage was proposed in *Cybernetics*. The world's first powered upper limb prosthesis was realized in 1955 which utilized surface electromyography (sEMG) as one of sensory feedback of the AMCS [90]. These physiological signals obtained by sensors are found to have a considerable amount of noise making it difficult to extract physical meaning as well as the intention of the

users. Several models as estimators have been investigated by machine learning (ML) algorithms with signal processing, which make prostheses recognize sEMG patterns defined by the user [91, 92, 93]. Recent studies suggest that algorithms such as a deep convolutional network [94] and reinforcement learning [95] may also be adapted to the pattern recognition problem.

ML algorithms are applied to other assistive devices to design estimators, as the algorithms can be applied for any type of data. Supervised machine learning algorithms, such as the artificial neural network (ANN) and linear discriminant analysis (LDA), have been used in combination with sEMG to develop the models of estimators detecting the user's muscular state for exoskeletons [96, 97]. In general, the following three steps are required to train the algorithms for the classifiers. First, the number of user's muscular state is defined. For example, three hand poses can be selected [97], and numbers are assigned to each pose (e.g., 1: transverse volar grip, 2: lateral pinch, and 3: extension grip). Then, specific tasks (e.g., holding a jar, holding a key, holding a plate) are chosen to collect training data corresponding to each of the defined states. In the end, users are asked to perform these tasks to obtain training data including sEMG signals, interacting with real objects if needed. The maximum voluntary contraction (MVC) may also be acquired to normalize sEMG in the last step. These procedures enable the ML algorithms to design functions as estimators that relate these experimental data to the assigned number of poses (i.e., muscular states).

In parallel with the development of estimators with ML algorithms, knowledge obtained from scientific studies, such as biology and neuroscience, is used effectively to develop the HMCS model including physiological signals in Fig. 1.5. In terms of actuators of the HMCS model, Hill introduced the well-known dynamic muscle model [98]. Being added a pennation angle, a tendon model, and properties occurred by aging [99, 100], the muscle model has been improved through several studies to match the model behavior with that of the physical plant. Utilizing the knowledge of these muscle models obtained through the scientific studies, musculoskeletal models and simulations have been developed to investigate muscular activities [101, 102, 103] from the engineering point of view[4]. These musculoskeletal models have also been utilized in the HMCS model of assistive devices, being simplified by engineers to develop the devices that satisfy the requirements accordingly. Assistive devices are thus able to track the user's limbs precisely by estimating the associated joint torques with sensory feedback of the user's joint angles and surface electromygraphy (sEMG) [76, 77, 104].

Estimators may be developed with the HMCS model (i.e., the musculoskeletal model) instead of ML algorithms, as patterns of muscular activation in each state (e.g., in three hand poses) can be simulated with the HMCS model. It can be said that the HMCS model enables to develop the estimators without any experimental data when the model matches with the physical plant. With knowledge of the HMCS model, assistive device users may be able to receive benefits of reducing

[4]According to a reference [21], "In science, the value of a *model* lies in how well its behavior matches that of the physical system. In engineering, the value of the *physical system* lies in how well its behavior matches that of the model". The model in engineering does not have to interpret the physical plant. For example, one of the simple models of laptop applications can be defined as "*if 2 is pressed on a keyboard, print 2 on a screen*". There is no physical phenomenon between the keystroke and the screen display. However, the model is well-known to laptop users while they do not have any knowledge about mechatronics.

their efforts to collect data before using the devices.

Contribution

In this dissertation, an estimator is introduced with the knowledge of the ML algorithms and the HMCS model to extract features of the human movement, allowing for task identification, and for tracking if the user is currently performing a task assigned by the user. In particular, a framework is proposed to design the binary sEMG classifier as an estimator in Fig. 1.9, which can be useful for limited applications (e.g., load-lifting) but requires fewer tasks for collecting training data. As described above, the ML algorithms can be applied for any type of training data to design a classifier. Since the algorithms are generalized, these algorithms require training data obtained in all procedures for the classification. It is not desirable for the users to deal with the procedures only for collecting the training data before using the devices. The procedures can be reduced by the proposed framework which incorporates the knowledge of the HMCS model about a relation between the muscular parameters and the associated force. The performance of the proposed framework was compared with that of the ANN and validated through experiments in chapter 6.

1.4 Summary

1.4.1 Summary of Contributions

A brief summary of the contributions are as follows:

- Characterization of an Active/Passive Pneumatic Actuator (AP2A), which can work as a passive spring with controllable stiffness to achieve suitable transitions between several assist modes [105, 106].
- Proposal of a high-level controller which segments dynamics of the assistive systems in *assist* and *no-assist* modes, and a control structure appropriate for *assist* mode to balance the competing goals of minimizing the energy consumption of the devices while maximizing the user assistance [107].
- Experimental validation and analysis of performance of the controller with the AP2A in application to a pendulum and an exoskeleton [108].
- Development of an estimator as guards of the high-level controller, which classifies tasks while reducing the users' efforts to collect training data for the use of daily assistive devices [109].

1.4.2 Dissertation Outline

Relations between each contribution are depicted in Fig. 1.11 which is designed based on Fig. 1.4 and Fig. 1.5. In chapter 2, design and a low-level controller of the AP2A are discussed. Based

on desired values, the controller modifies control signals u for solenoid valves, which determine the switching timings and the amount of valve opening times. The desired values are provided by a high-level controller of the AP2A discussed in chapter 3. This controller sets the reference r, balancing the energy consumption of the AP2A (i.e., air consumption from a compressor) and the external power source. The performance of the high-level controller is verified with two physical plants, a pendulum and human subjects (chapters 4 and 5). It is difficult to model the energy consumption of a human subject (e.g., the metabolic cost of transportation), as human modeling is still ongoing research in both science and engineering. A pendulum is relatively easy to model and to measure several parameters such as a joint torque, and it is utilized to figure out the effects of assistance provided by the AP2A in chapter 4. In chapter 5, experimental results from prior work [74, 110] were analyzed for reasoning the performance of the AP2A as assistive devices. The design of an estimator for an assistive device is described in chapter 6, which works as guards in Fig. 1.10 to inform the high-level controller of timing to start/stop assistance. Concluding remarks and open issues are discussed in the last chapter 7.

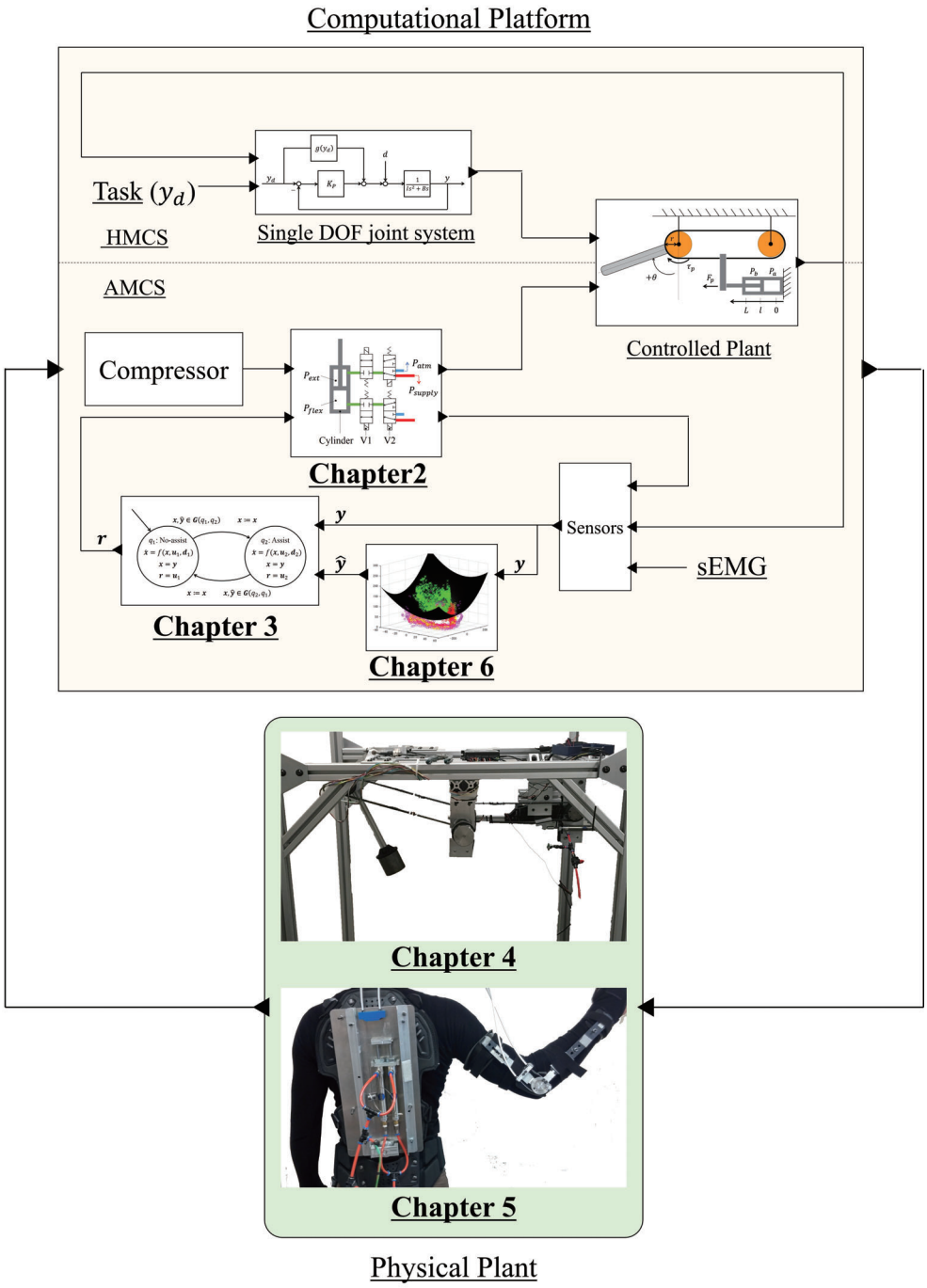

Figure 1.11: Overview of this dissertation.

Chapter 2

Control of Active/Passive Pneumatic Actuator

2.1 Chapter Overview

Assistive devices with active components (e.g., electrical geared motors) modify the dynamics adaptively at the expense of energy. Passive components (e.g., springs) change the mechanical impedance around the human joints without energy consumption. However, replacements are required to modify the impedance. This chapter contributes to developing an Active/Passive Pneumatic Actuator (AP2A) inspired by the prior work [74], which utilizes the advantages of both active and passive components for energy-efficient interaction. Design and two low-level controllers of the AP2A are proposed in sections 2.4 and 2.5, describing the control methods to tune stiffness and equilibrium of the AP2A with an array of solenoid valves. Experimental results suggest that the AP2A can work as a passive spring with controllable stiffness.

2.2 Modeling of Pneumatic Actuator and Air Mass Flow

Fig. 2.1 shows the design mechanisms of the AP2A improved from prior work [74]. In prior work, the valve array consists of one 3-way valve and two 2-way valves. By connecting to the supply pressure source (P_{supply}) or atmosphere (P_{atm}), the valve 2 (V2) determines to pressurize or depressurize gas in both chambers. The other valve (V1) opens the corresponding ports to modify the pressures in each chamber (i.e., P_{ext}, P_{flex}). Otherwise, V1 seals a chamber of the air cylinder by closing the ports, and it makes the actuator work as a passive spring.

The valve array allows the chamber pressures to be set independently. However, there will be a delay when one of the chamber pressure (P_{ext}) needs to be increased while the other (P_{flex}) is required to be decreased. It is impossible to pressurize and depressurize the chamber pressures at the same time, as there is only one V2. Thus, by adding an additional V2, the array of valves was modified to control pressures in each chamber separately. In this section, a numerical model

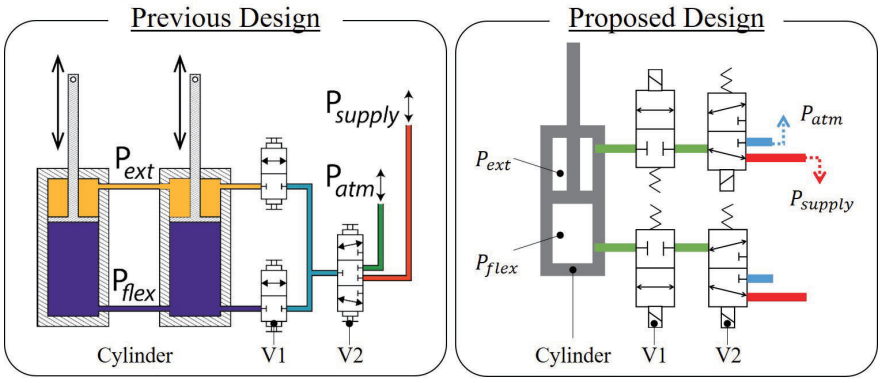

Figure 2.1: Comparison of a valve array proposed in prior work [74] and current study.

of a pneumatic cylinder and air mass flow through the valves V1 and V2 are described to design a low-level controller of the actuator.

2.2.1 Modeling of Pneumatic Cylinder

The basic dynamics of a pneumatic actuator can be modeled as Fig. 2.2. The dynamics of the system shown in Fig. 2.2 can be expressed as:

$$F_p := P_a A_a - P_b A_b - P_{atm} A_r \tag{2.1}$$
$$m\ddot{l} = F_p + F_l \tag{2.2}$$

where F_p is pneumatic force applied to the rod, P_i is air pressures in a chamber i (i.e., chamber a or b), A_a, A_b are an effective area calculated from the bore of the actuator, P_{atm} is the atmospheric pressure, A_r is a cross-sectional area of a rod, m is mass of the rod and external load, F_l is force applied to the rod. In each chamber, the following equations are derived from the ideal gas law under the assumptions of the perfect gas:

$$P_i V_i = m_i R T \tag{2.3}$$
$$V_a := V_{0_a} + A_a l \tag{2.4}$$
$$V_b := V_{0_b} + A_b (L - l) \tag{2.5}$$

where V_i is a volume of the chamber i, m_i is a mass of gas in the chamber i , R is the ideal gas constant, T is a temperature of the air, V_{0_i} is a volume at the end of stroke area for the chamber i, l is a position of the rod, L is a stroke of the actuator. When all processes occurring in the chambers are assumed to be isothermal (i.e., T to be constant) [89]:

$$\dot{P}_a = (\dot{m}_a R T - P_a A_a \dot{l}) / V_a \tag{2.6}$$
$$\dot{P}_b = (\dot{m}_b R T + P_b A_b \dot{l}) / V_b \tag{2.7}$$

where $\dot{m}_i$ is a mass flow of air entering or leaving the chamber i.

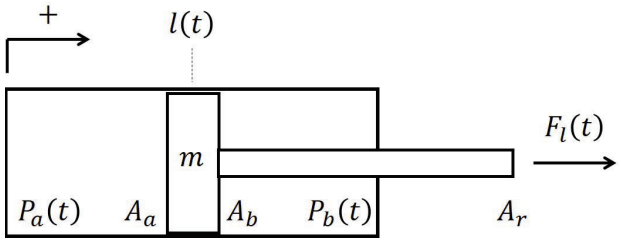

Figure 2.2: Model of a pneumatic actuator.

2.2.2 Empirical Modeling of Air Mass Flow

The air mass flow can be described as a nonlinear function of the system inputs. The flow $\dot{m}_i$ can be expressed as [70, 89]:

$$\dot{m}_i = \Psi(P_u, P_d) A_v(u) \tag{2.8}$$

$$\Psi := \begin{cases} C_f C_1 \dfrac{P_u}{\sqrt{T}} & (z \leq P_{cr}) \\ C_f C_2 \dfrac{P_u}{\sqrt{T}} z^{1/k} \sqrt{1 - z^{(k-1)/k}} & (z > P_c r) \end{cases}$$

where u is a control input (e.g., an input voltage to the valve), C_f is a non-dimensional discharge coefficient, P_u is an upstream pressure, and P_d is a downstream pressure. z is a ratio of these pressures such that:

$$z := P_d / P_u \tag{2.10}$$

C_1, C_2, and P_{cr} are constants for a given gas:

$$C_1 := \sqrt{\frac{k}{R}\left(\frac{2}{k+1}\right)^{k+1/k-1}},\ C_2 := \sqrt{\frac{2k}{R(k-1)}},\ P_{cr} := \left(\frac{2}{k+1}\right)^{k/k-1} \tag{2.11}$$

where k is a heat specific ratio of the gas. A_v is an effective valve area which is utilized to describe the mass flow through a single valve. The area is algebraically related to the valve spool position tuned by the control inputs u. The control of the area has been investigated for a solenoid valve [111] as well as a proportional valve [70, 89]. One idea is to utilize the theoretical model expressed in the equations above. However, the AP2A utilizes a series of two solenoid valves (V1, V2 in Fig. 2.1). Thus a switching algorithm of the two solenoid valves is designed to tune the air flow. An input-output function was empirically estimated, representing a relation between a valve opening time of V1 $t_{v_1 i}$ and the air mass flow $\dot{m}_i$.

Fig 2.3 shows a switching algorithm of the two solenoid valves V1 and V2 attached to the chamber a[1]. The algorithm is expressed as a finite state machine (FSM) [17]. The algorithm

[1]The switching algorithm is described only for the chamber a in the following paragraphs. However, the identical algorithm was applied to the valves for the chamber b.

outputs digital command signals v1 and v2 to the solenoid valves V1 and V2, respectively. One of the inputs $t_{v_1 a}$ is a valve opening time of V1, and the other input $v_2 a \in \{0,1\}$ is a binary control signal of V2 in Fig. 2.1. The control input for V2 is determined based on a sign of the system input (i.e., the air mass flow) as follows:

$$v_2 a = \begin{cases} 0 & (\dot{m}_a > 0) \\ 1 & (\dot{m}_a \leq 0) \end{cases}$$

Names of each discrete mode in the FSM suggest binary output signals v1 and v2, as described in Fig 2.4. For example, a discrete mode named H/L indicates v1 is High ($=1$), and v2 is Low ($=0$). Note that V1 seals the chamber a when v1 is low, and V2 pressurizes the system when v2 is low.

2.2.3 Experimental Validation

Experimental Identification Method for Air Mass Flow

Several control inputs $t_{v_1 a}$ and $v_2 a$ were applied to the FSM in Fig. 2.3 to empirically estimate an input-output function between the inputs and the air mass flow $\dot{m}_a$. For each value, the FSM was terminated once it came back to the discrete state *Ini* (i.e., in each trial, the experimental time was $t \in [0, t_{cycle}]$). The mass flow $\dot{m}_a$ resulting from the control inputs were approximated as outputs with pressure measurements as follows:

$$\dot{m}_a \approx (m_a(t_{cycle}) - m_a(0))/t_{cycle} \tag{2.13}$$

$$= (P_a(t_{cycle}) - P_a(0))V_{fix}/(t_{cycle}RT) \tag{2.14}$$

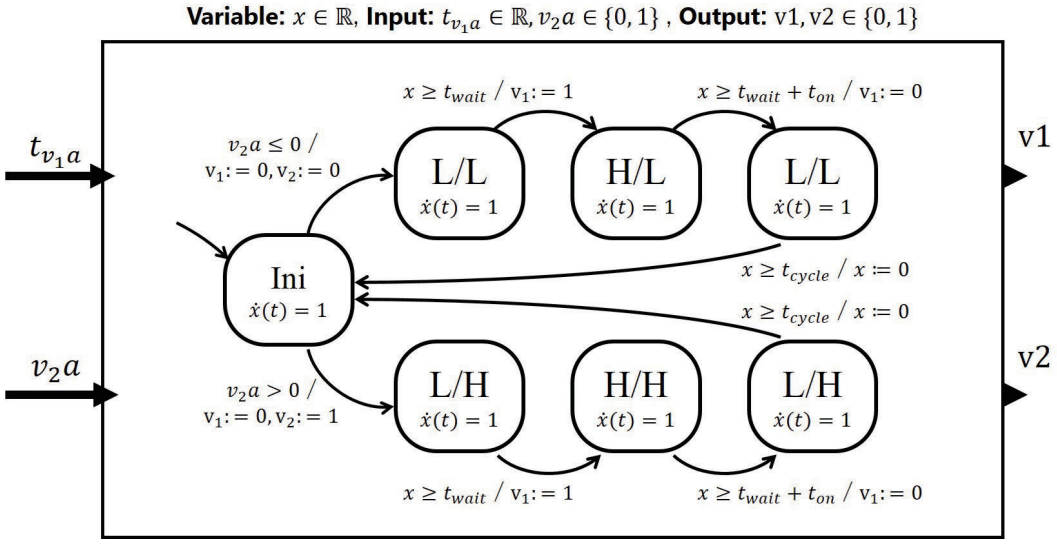

Figure 2.3: Switching algorithm of solenoid valves V1 and V2 for the chamber a.

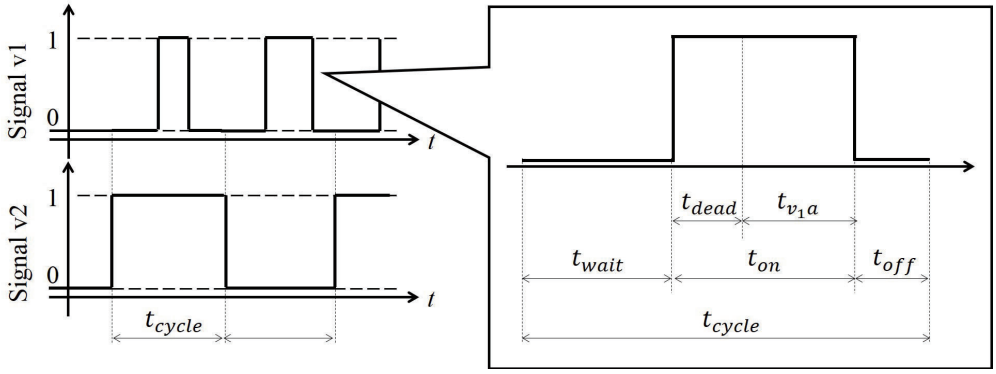

Figure 2.4: Another representation of output signals of the FSM in Fig. 2.3.

where $P_a(0)$ is the initial pressure in the chamber a, and V_{fix} is the fixed volume of V_a in each trial. The following curves were developed as empirical, nominal functions:

$$\dot{m}_a = \hat{g}_a(t_{v_1a}) = \begin{cases} \theta_{1a+}(1-\exp(-\theta_{2a+}t_{v_1a}))(P_u - P_d)^{\theta_{3a+}} \ (v_2a = 0) & \text{(2.15a)} \\ \theta_{1a-}(1-\exp(-\theta_{2a-}t_{v_1a}))(P_u - P_d)^{\theta_{3a-}} \ (v_2a = 1) & \text{(2.15b)} \end{cases}$$

By non-linear curve fitting, the coefficients $\theta_{1a\pm}, \theta_{2a\pm}, \theta_{3a\pm}$ were acquired for each condition of $P_a(0)$ and V_{fix}. Possible gaps in the empirical functions were investigated as γ_a.

Experimental Setups

Fig. 2.5 shows the experimental setup. A 0.75 inch bore, 4 inch stroke cylinder was used in the experiment (Bimba, D044). A potentiometer was attached to the rod to measure the position of the rod. The valve array in Fig. 2.5 consisted of two three-port solenoid valves (Festo, MHE3-MS1H-3/2G-QS-6-K) for each chamber. One of the valves functions as V1 (Fig. 2.1) was operated as a two-port solenoid valve. An air compressor was used to supply compressed air at 515 kPa ($= P_{supply}$) to the actuator. Two pressure sensors (Omega, PX40-100G5V) were used for each chamber to measure the supply pressure P_{supply} near V2 and the pressure inside the chamber (i.e., P_i). A linear actuator (Eco-worthy, stroke 200 mm) was introduced to regulate the rod position of the cylinder. A microcontroller (STM32, F746ZG) sampled the above sensors and logged the data to a PC via serial communication. The microcontroller controlled the linear actuator for the rod position and tuned the control inputs (i.e., t_{v_1i}, v_2i).

Experimental Conditions

The parameters $\theta_{ki\pm}$, $k \in \{1,2,3\}$ in (2.15a) and (2.15b) were identified empirically. The values of t_{v_1i} and v_2i were set as follow:

$$t_{v_1i} = 0.2, 0.4, 0.8, 1.2, 1.6, 2.0, 2.4 \quad \text{(2.16)}$$

$$v_2i = 0, 1 \quad \text{(2.17)}$$

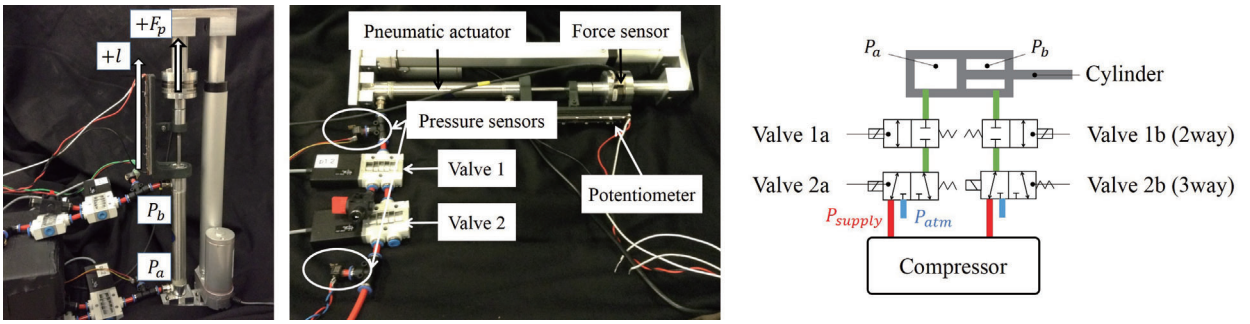

Figure 2.5: Experimental setups and a schematic of the AP2A.

The unit of $t_{v_1 i}$ is millisecond. Other variables in Fig 2.4 were implemented to the microcontroller as follows:

$$[t_{cycle}, t_{wait}, t_{dead}]^T = [10, 5, 1.25]^T \tag{2.18}$$

$$t_{off} = t_{cycle} - (t_{wait} + t_{on}) \tag{2.19}$$

All units are millisecond. $P_i(0)$ and V_{fix} in (2.14) were modified for each trial, as well as the input signals $t_{v_1 i}$ and $v_2 i$. The reason being that $P_i(0)$ and V_{fix} may affect the mass flow according to the theoretical mass flow model (2.8). Thus, experiments were conducted under combinations of different $P_i(0)$ (i.e., $z \leq P_{cr},\ z > P_{cr}$) and V_{fix} (i.e., the rod position was fixed at the bottom and top $l \approx 12.5$ and 86.5 mm, respectively). Five trials were carried out to estimate the mass flow $\dot{m}_i$ under each condition (i.e., in total 280 trials for each chamber a and b). These trials were conducted with the setups explained above. After collecting the data, the fitting problem to estimate $\theta_{k\pm}$ was solved by `lsqnonlin` solver in `MATLAB 2017a`.

Experimental Results

Fig. 2.6 and 2.7 show empirical results of an air mass flow estimated by (2.14) and fitting curves $\hat{g}_{a+}$ and $\hat{g}_{a-}$ in (2.15a) and (2.15b). Note that these figures are the empirical results of chamber a. Fig. 2.6 shows the empirical condition of air intake (i.e., pressurization, $v_2 a = 0$), and Fig. 2.7 suggests the empirical condition of air exhaust (i.e., depressurization, $v_2 a = 1$). The rod position was fixed at the bottom in Fig. 2.6a and 2.7a and at top in Fig. 2.6b and 2.7b. In those figures, red crosses and squares suggest the empirical data estimated in different pressure conditions (i.e., $P_a(0)$). Dotted black lines indicate fitting curves with computed coefficients. The computed coefficients for the condition $v_2 a = 0$ are:

$$[\theta_{1a+}, \theta_{2a+}, \theta_{3a+}]^T = [1.5 \cdot 10^{-6}, 7.3 \cdot 10^{2}, 5.0 \cdot 10^{-1}]^T \text{(bottom)} \tag{2.20}$$

$$= [3.7 \cdot 10^{-6}, 6.9 \cdot 10^{2}, 4.7 \cdot 10^{-1}]^T \text{(top)} \tag{2.21}$$

$$[\theta_{1b+}, \theta_{2b+}, \theta_{3b+}]^T = [1.7 \cdot 10^{-7}, 4.0 \cdot 10^{2}, 5.0 \cdot 10^{-1}]^T \text{(bottom)} \tag{2.22}$$

$$= [3.1 \cdot 10^{-7}, 7.1 \cdot 10^{2}, 5.0 \cdot 10^{-1}]^T \text{(top)} \tag{2.23}$$

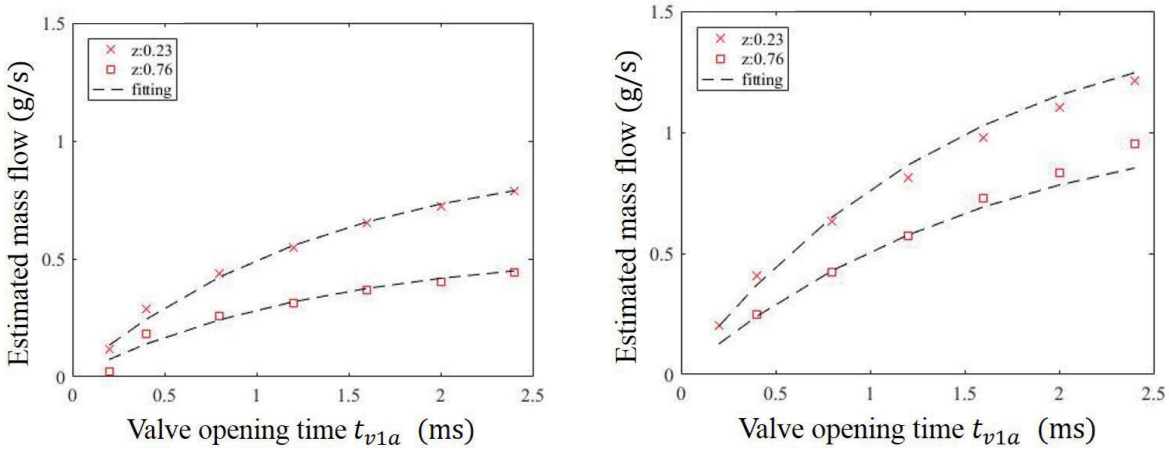

(a) Rod position at the bottom.

(b) Rod position at the top.

Figure 2.6: Experimental plots of air mass flow $\dot{m}_a$ and the fitting curves when $\dot{m}_a > 0$.

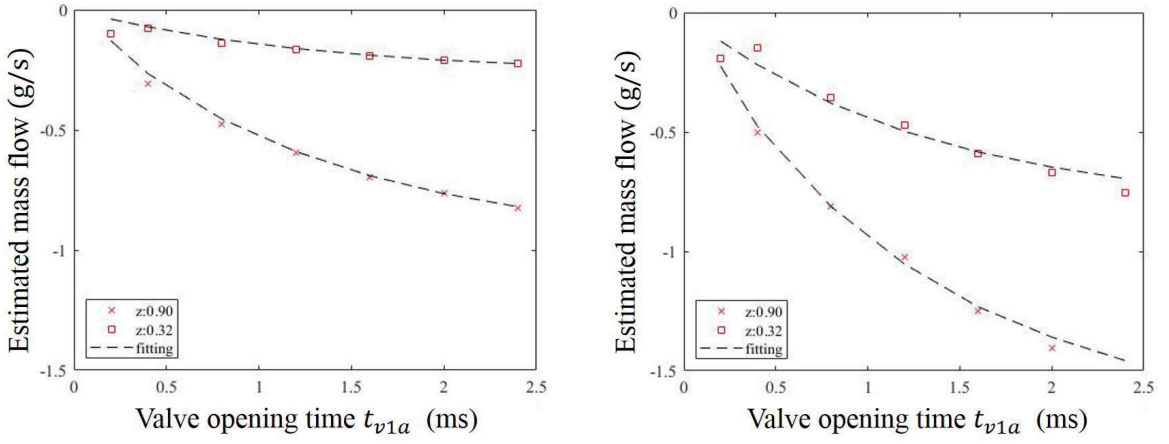

(a) Rod position at the bottom.

(b) Rod position at the top.

Figure 2.7: Experimental plots of air mass flow $\dot{m}_a$ and the fitting curves when $\dot{m}_a < 0$.

When the condition was modified to $v_2a = 1$, the coefficients of the curves are:

$$[\theta_{1a-}, \theta_{2a-}, \theta_{3a-}]^T = [3.4 \cdot 10^{-8}, 7.9 \cdot 10^2, 8.0 \cdot 10^{-1}]^T \text{(bottom)} \quad (2.24)$$
$$= [4.5 \cdot 10^{-9}, 7.9 \cdot 10^2, 1.0]^T \text{(top)} \quad (2.25)$$

$$[\theta_{1b-}, \theta_{2b-}, \theta_{3b-}]^T = [2.7 \cdot 10^{-9}, 8.0 \cdot 10^2, 8.0 \cdot 10^{-1}]^T \text{(bottom)} \quad (2.26)$$
$$= [6.5 \cdot 10^{-9}, 8.0 \cdot 10^2, 8.0 \cdot 10^{-1}]^T \text{(top)} \quad (2.27)$$

2.2.4 Discussion

All four figures indicate that the nominal function (2.15a), (2.15b) fit to the experimental data regardless of initial pressures on the chamber. As suggested in the empirical results, such as the difference between (2.20) and (2.21), the computed coefficients of the function were not identical when the initial rod position was modified.

According to these results, an average of the two fitting curves estimated at the bottom and top was utilized as an air mass flow model in the following sections. The upper bound of model errors was computed as uncertainties based on the averaged model and these empirical results. For example, the uncertainty γ_{a+} was determined by computing the errors between the average function and the empirical results (2.20), (2.21). Similarly, nominal functions $\hat{g}_{a-}$ and $\hat{g}_{b\pm}$ were investigated through the analysis. The air mass flows $\dot{m}_i$ are now assumed to be written with the function g_i and system inputs $t_{v_1 i}$, $v_2 i$ as follows:

$$\dot{m}_i = g_i(t_{v_1 i}, v_2 i) \quad (2.28)$$

In the following text, a part of the system inputs (i.e., $v_2 i$) is neglected for simplification.

2.3 Force Control of a Pneumatic Actuator

In this section, an active force controller is designed with the air mass flow model. The system can be expressed with a state vector $\mathbf{x} \in \mathbb{R}^4$, an input vector $\mathbf{u} \in \mathbb{R}^2$, and a disturbance d:

$$\mathbf{x}(t) := [l, \dot{l}, P_a, P_b]^T \quad (2.29)$$
$$\mathbf{u}(t) := [t_{v_1 a}, t_{v_1 b}]^T \quad (2.30)$$
$$d(t) := F_l \quad (2.31)$$

$$\dot{\mathbf{x}} = f(\mathbf{x}, \mathbf{u}, d) = \begin{bmatrix} \dot{l} \\ (F_p + F_l)/m \\ (g_a(t_{v_1 a})RT - P_a A_a \dot{l})/V_a \\ (g_b(t_{v_1 b})RT + P_b A_b \dot{l})/V_b \end{bmatrix} \quad (2.32)$$

Note that the first two states in (2.29) can be neglected under certain conditions. For examples, in previous studies, the rod position l seemed to be regulated by a servo motor [70] (i.e., an actuator controlled the external force F_l) or a relatively heavy load [69] (i.e., adding an external load to the rod, $m = 10$ kg). As well as the previous studies, the system is assumed to be stabilized around a fixed point, assuming that the external force F_l is well-controlled by the external controller. With this assumption, the reduced-order system with a new state vector $\bar{\mathbf{x}} \in \mathbb{R}^2$ can be expressed as:

$$\bar{\mathbf{x}}(t) := [P_a, P_b]^T \tag{2.33}$$

$$\begin{aligned} \dot{\bar{\mathbf{x}}} &= f_r(\bar{\mathbf{x}}, \mathbf{u}, d) \\ &= \begin{bmatrix} (g_a(t_{v_1 a})RT - P_a A_a \dot{l})/V_a \\ (g_b(t_{v_1 b})RT + P_b A_b \dot{l})/V_b \end{bmatrix} \end{aligned} \tag{2.34}$$

2.3.1 Force Control with Air Mass Flow Model

The chamber a was utilized to achieve force control in order to validate the air flow model. Assuming that the chamber b is kept open, the pneumatic force in (2.1) becomes:

$$F_p = P_a A_a - P_{atm}(A_b + A_r) \tag{2.35}$$

Considering the control of the force F_p by tuning the pressure P_a, a derivative of the force is computed according to (2.35) as follows:

$$\dot{F}_p = \dot{P}_a A_a = (g_a RT - P_a A_a \dot{l}) \frac{A_a}{V_a} \tag{2.36}$$

Note that the function g_a indicating the air mass flow includes the uncertainty γ_a, as it was discussed in the previous sections. Thus, the uncertainty needs to be taken into consideration for this force control. A sliding mode control (SMC) was utilized to handle the model uncertainty. A sliding surface $s_F \in \mathbb{R}$ of SMC can be written as:

$$s_F := F_p - F_{p_d} \tag{2.37}$$

Note that the relative degree of the system is one, as the control input (i.e., $t_{v_1 a}$) appears by taking the first derivative of the sliding variable. Therefore, the first-order SMC was chosen with the following control law:

$$t_{v_1 a} = \hat{g}_a^{-1} \left(\frac{1}{RT} (\dot{F}_{p,d} \frac{V_a}{A_a} + P_a A_a \dot{l}) - \gamma_a sgn(s_F) \right) \tag{2.38}$$

$$|g_a - \hat{g}_a| \leq \gamma_a \tag{2.39}$$

Stability

A Lyapunov function can be chosen as follows:

$$W := \frac{1}{2} s_F^2 \tag{2.40}$$

then,

$$\begin{aligned} \dot{W} &= s_F \dot{s}_F \\ &= s_F \left(\dot{F}_p - \dot{F}_{p,d} \right) \\ &= s_F \left(\frac{1}{V_a} ((g_a - \hat{g}_a + \hat{g}_a) RT - P_a A_a \dot{l}) - \dot{F}_{p,d} \right) \\ &= s_F \frac{A_a}{V_a} RT \left(g_a - \hat{g}_a - \gamma_a sgn(s_F) \right) \\ &\leq 0 \end{aligned} \tag{2.41}$$

which guarantees the force F_p is bounded around the sliding surfaces.

2.3.2 Experimental Validation

Experimental Setups

The same experimental setups in the previous section (Fig. 2.5) were used in this experiment. A force sensor (ATI Industrial Automation, F/T Sensor Mini45) was added to the experimental setups to measure the pneumatic force, attached between the cylinder and the linear actuator. The force data was measured at 1000 Hz with NI-DAQ USB-6363 using `MATLAB 2017a`. The data were synchronized with the data captured by the microcontroller. A low-pass filter (3rd order, Butterworth, cutoff: 10 Hz) was applied to the measured force data to remove the noise arising from the sensor.

Experimental Conditions

Two experiments were conducted to confirm the performance of the force controller. In the first experiment, two-step input signals were applied as the desired signal (i.e., $F_{p,d}$ = 20, 80 N), which are close to the minimum and maximum values of the reference in the following experiment. In this experiment, the linear actuator was set at the top of the stroke (i.e., l = 0.09 m).

In the second experiment, the desired force $F_{p,d}$ was designed as a sinusoidal signal. The frequency was set at 0.15 Hz, and the magnitude of the signal was 25 N biased by 50 N. The desired pressure P_{a_d} corresponding to the minimum and maximum values of the reference were 190 and 365 kPa, which were the values assumed to be around the atmosphere and a supply pressure (=515 kPa). The linear actuator was fixed at the bottom and top of the stroke (i.e., $l \approx 0.02, 0.09$ m) as well as the previous experiments to model the air mass flow $\dot{m}_i$.

Experimental Results

The experimental results are shown in Fig. 2.8 and 2.9. Fig. 2.8 shows a result of step responses. Solid blue and red lines indicate empirical step responses to different references (20 and 80 N, respectively). The means and standard deviations of the output forces at the steady-state were 20.1 ± 0.5 and 80.0 ± 0.8 N. Note that the system is assumed to be the first order as expressed in (2.36). However, the responses seem to be the second-order during the rise time due to the effects of the low-pass filter.

Fig. 2.9 shows responses to a sinusoidal input (0.15 Hz) in steady-state and errors between empirical results and the references. Solid blue lines and dotted black lines suggest the empirical results and the references, respectively. The rod position was fixed at the bottom in Fig. 2.9a and at the top in 2.9b of the stroke, respectively. The maximum errors in these figures were 5.1 and 10.5 N, respectively.

2.3.3 Discussion

Experimental results suggest that the AP2A with a control law (2.38) including the air flow model can perform well in steady-state, however, its bandwidth may become narrow in some cases. Responses to step inputs show the steady-state performance of the system. As shown in Fig. 2.8, the mean output errors were less than $\pm 5\%$. Though a chattering effect was confirmed due to the SMC, these empirical results suggest that the designed controller had small steady-state errors. Thus, with our system setups utilizing the developed air flow model, the actuator could be controlled to reach the desired force.

Fig. 2.9 shows responses to a sinusoidal input (0.15 Hz). Fig. 2.9a shows empirical force response when the rod position was at the bottom. The empirical force was tuned to be within

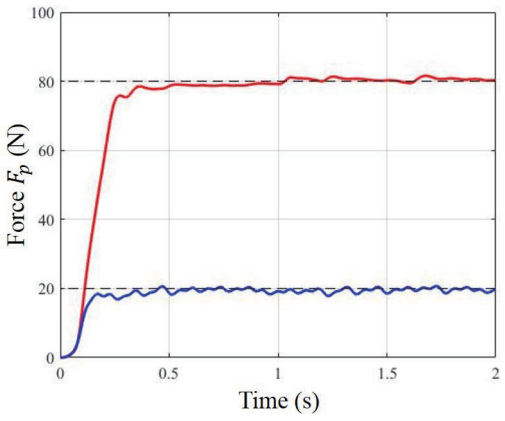

Figure 2.8: Force responses to step inputs when the rod position was set at the top.

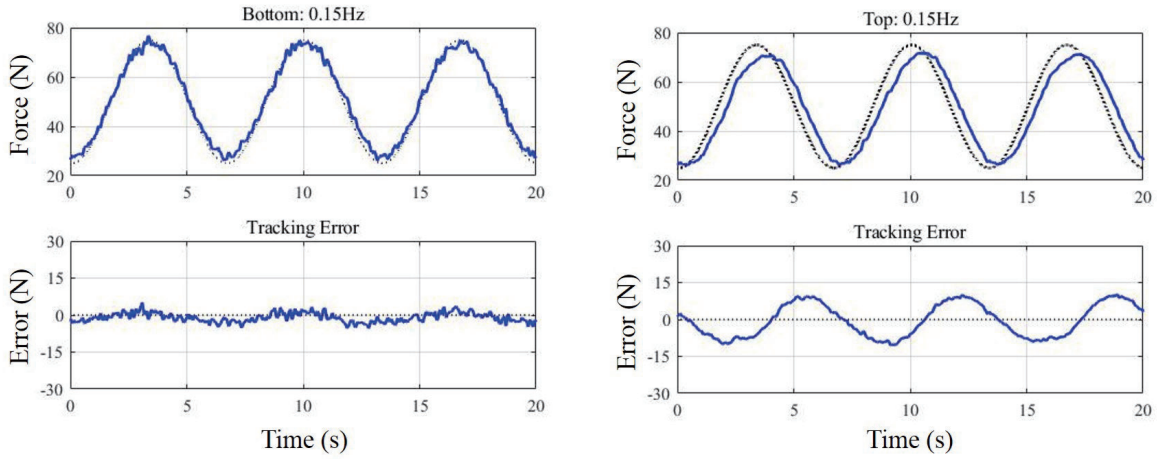

(a) Rod position at the bottom.

(b) Rod position at the top.

Figure 2.9: Force responses to sinusoidal inputs ($f = 0.15$ Hz).

$\pm 10\%$ of the desired force (i.e., the maximum error was 5.1 N). In this experimental condition, it can be said that the control law including the air flow model (2.38) worked well to control the pneumatic force. In contrast, when the position was set at the top, the maximum error increased to 10.5 N which was around $\pm 20\%$ of the desired force. Fig. 2.9b indicates that there was a delay that caused the tracking error.

These differences indicate one of the limitations of the switching algorithm in Fig 2.3. When the rod moved from the bottom to top, a volume of the chamber a became larger as the rod position determines the volume. More supply air was required to increase the pressure by filling the chamber with the compressed air if the rod position was set at the top. However, the compressed air that the chamber could intake was limited because of the maximum valve opening time which was fixed to assure the constant sampling period (i.e., feedback cycle). Thus, the pneumatic force was not responsive to the sinusoidal reference, and the tracking error in Fig. 2.9b was confirmed accordingly.

Above all, the AP2A with the model-based force controller could perform well in the steady-state. In the following sections, step responses of the AP2A in the steady-state were further validated by controlling chamber pressures (i.e., P_a and P_b) simultaneously.

2.4 Model-based Control for Variable Stiffness Actuator

The force controller utilized one of the chambers (i.e., chamber a), but the pneumatic actuator has two chambers. It is thus able to control two parameters in theory, and the desired stiffness is now introduced to response as a variable stiffness actuator [69, 70]. Moreover, a switching controller was implemented to make the AP2A work as a nonlinear passive spring.

2.4.1 Simultaneous Force and Stiffness Control

References for Variable Stiffness Actuator

An instantaneous stiffness K of the actuator towards F_l can be expressed as:

$$\begin{aligned} K &= \frac{\partial F_l}{\partial l} = \frac{\partial (m\ddot{l} - F_p)}{\partial l} \\ &= \frac{P_a A_a}{l} + \frac{P_b A_b}{(L-l)} \end{aligned} \tag{2.42}$$

Given an equilibrium point l_{eq} (i.e., the point where $F_p = 0, \forall t$) and the desired stiffness K_d at the equilibrium point of the passive nonlinear spring, the corresponding desired pressure $\hat{P}_{i_d}$ for the chamber i is calculated by solving the following simultaneous equations based on (2.1) and (2.42):

$$F_p = \hat{P}_{a_d} A_a - \hat{P}_{b_d} A_b - P_{atm} A_r = 0 \tag{2.43}$$

$$K_d = \frac{\hat{P}_{a_d} A_a}{l_{eq}} + \frac{\hat{P}_{b_d} A_b}{(L-l_{eq})} \tag{2.44}$$

Though the rod moved from the equilibrium point, the mass of air in each chamber is expected to be constant to work as the desired nonlinear spring. According to (2.4) and (2.5), the desired pressure P_{i_d} at the rod position l for the chamber i can be computed as follows:

$$P_{i_d} := \hat{P}_{i_d} V_i(l_{eq}) / V_i(l) \tag{2.45}$$

Sliding Mode Control

The controller for the AP2A is designed based on the reduced model (2.33) and references (2.43) to (2.45) with the assumptions. A sliding surface $\mathbf{s} \in \mathbb{R}^2$ is written as:

$$\mathbf{s} := \begin{bmatrix} s_a \\ s_b \end{bmatrix} = \begin{bmatrix} P_a - P_{a_d} \\ P_b - P_{b_d} \end{bmatrix} \tag{2.46}$$

The control input $t_{v_1 i}$ appears by taking the first derivative of the sliding variables. The first-order sliding mode control (SMC) is thus expressed as:

$$\begin{aligned} \mathbf{u} &= \mathbf{u}_{SMC} \\ &= \begin{bmatrix} \hat{g}_a^{-1} \left((\dot{P}_{a_d} V_a + P_a A_a \dot{l})/RT - \gamma_a sat(s_a/\phi_a) \right) \\ \hat{g}_b^{-1} \left((\dot{P}_{b_d} V_b - P_b A_b \dot{l})/RT - \gamma_b sat(s_b/\phi_b) \right) \end{bmatrix} \end{aligned} \tag{2.47}$$

$$|g_i - \hat{g}_i| \leq \gamma_i \tag{2.48}$$

where $\hat{g}_i$ is a nominal function in (2.28) for each chamber i, and ϕ_i is a constant for the SMC to avoid a large magnitude of chattering.

Now, the control law in (2.47) enables to tune the stiffness K_d and the equilibrium point l_{eq} of the AP2A. The controller is then extended to hybrid systems by adding another discrete mode q_2 as shown in Fig. 2.10. In a discrete mode q_1 as an initial mode, the controller utilizes the SMC in (2.47) to tune pressures *actively* in each chamber by controlling valves V1 and V2. When a difference between the state variables and the corresponding desired values falls within a specific range (i.e., when a guard in Fig. 2.10 is enabled), then the controller switches its mode from q_1 to q_2. In the discrete mode q_2, the controller seals the chambers by V1 and makes the actuator work as a passive component. Thus, the guard associated with an edge (q_1, q_2) (i.e., a condition to transit from q_1 to q_2) ensures the AP2A to perform as a nonlinear spring. Thresholds $\boldsymbol{\varepsilon} \in \mathbb{R}^2$ in the guard were defined as 5% of the desired pressures in this study.

Stability

With this control law, the Lyapunov function can be selected such that:

$$W := \frac{1}{2}\mathbf{s}^T\mathbf{s} \tag{2.49}$$

Then, with (2.34) to (2.48):

$$\begin{aligned} \dot{W} &= s_a\dot{s}_a + s_b\dot{s}_b \\ &= s_a\left(\frac{1}{V_a}((g_a - \hat{g}_a + \hat{g}_a)RT - P_aV_a\dot{l}) - \dot{P}_{a_d}\right) + s_b\dot{s}_b \\ &= s_a\frac{RT}{V_a}(g_a - \hat{g}_a - \gamma_a sat(s_a/\phi_a)) + s_b\dot{s}_b \\ &\leq 0 \end{aligned} \tag{2.50}$$

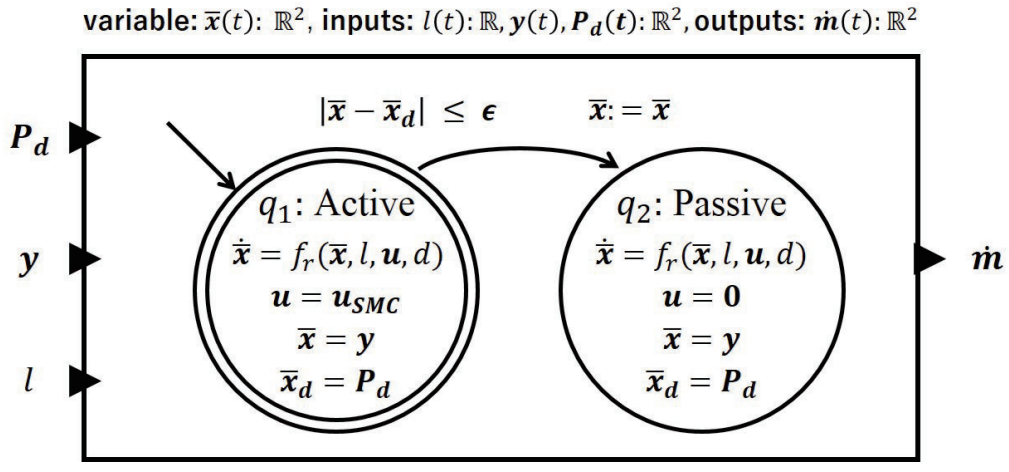

Figure 2.10: Design of a switching controller of the AP2A.

which guarantees the state vector $\bar{\mathbf{x}}$ is bounded around the sliding surfaces (i.e., pressures are bounded around the desired values).

2.4.2 Experimental Validation

Experimental Setups

The same experimental setups in the previous sections (Fig. 2.5) were used in the first experiment. Thus the descriptions are omitted to avoid duplication.

Experimental Conditions

Two experiments were conducted with the proposed SMC. In the experiments, the initial condition of the state $\mathbf{x}$ in (2.29) were set to be:

$$\mathbf{x}(0) := [l_{eq}, 0, P_{atm}, P_{atm}]^T \tag{2.51}$$

The initial rod position errors were confirmed to be within ± 1.0 mm. Both chambers were open to the atmosphere. The linear actuator remained stopped at the initial position to stabilize the rod position during each trial.

The first experiment was conducted to confirm the performance of the proposed controller. The equilibrium point l_{eq} in (2.51) was set at 30.0, 50.0, and 70.0 mm as experimental conditions. The desired stiffness K_d was set to be $2.00 \cdot 10^3$ and $4.00 \cdot 10^3$N/m. According to these conditions, the desired pressures were computed as a solution of (2.43) to (2.45) in each trial by the microcontroller. The microcontroller then tuned the pressures in the chambers according to the computed values. Five trials were conducted for each condition, and in total 30 trials were conducted in this experiment. Each trial was carried out for 10 seconds. The rod position and pressures in both chambers were measured in each trial.

Another five trials were carried out as the second experiment under the specific condition (l_{eq} = 50.0 mm, $K_d = 2.00 \cdot 10^3$N/m). The microcontroller tuned the pressures as well as the first experiment. In this experiment, after the 10 seconds, the linear actuator produced the force against the pneumatic force F_p produced by the AP2A to move the rod from $l \geq 70.0$mm to $l \leq 30.0$mm at a constant speed, as shown in Fig. 2.11. In Fig. 2.11, the solid black line shows the empirical data collected by the potentiometer. The dotted red line shows the linear approximated line based on the data with `lsline` function by `MATLAB 2017a`. The speed was estimated to be around 4.2 mm/s. The bottom curve shows errors between the black and the red line. The rod position, the pressures, and the interaction force were all measured in each trial. Table 2.1 shows the parameters of the model-based controller implemented in these experiments.

Experimental Results

The performance of the proposed controller are shown in Fig. 2.12 and 2.13 that were obtained in the first experiment. Fig. 2.12 shows the pressures in each chamber under several conditions, and

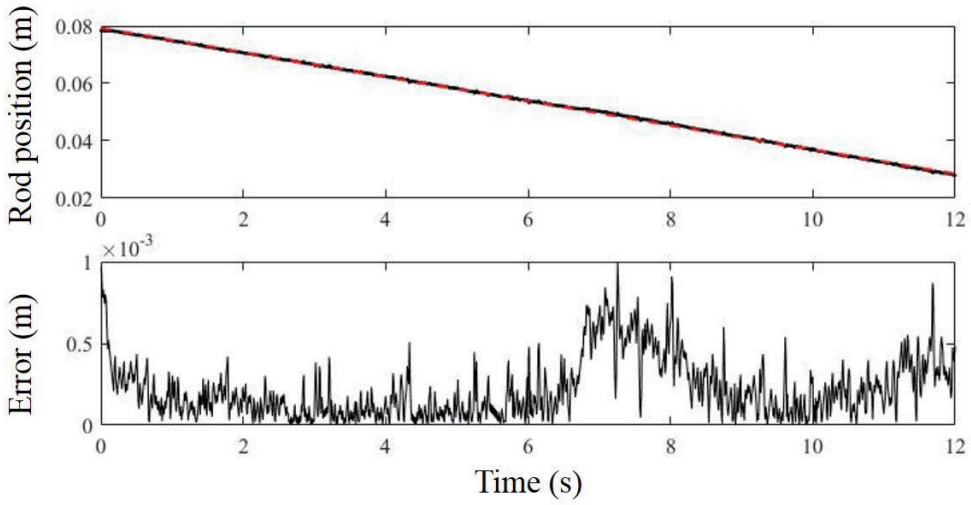

Figure 2.11: Rod position moved by the linear actuator during the second experiment.

Table 2.1: Parameters of the experimental setups in Fig 2.5

Params (unit)	**Value**	**Params (unit)**	**Value**
A_a (m^2)	$2.85 \cdot 10^{-4}$	A_b (m^2)	$2.53 \cdot 10^{-4}$
T (K)	293	R (J/kgK)	287
V_{0_a} (m^3)	$5.94 \cdot 10^{-6}$	V_{0_b} (m^3)	$5.94 \cdot 10^{-6}$
L (m)	$1.02 \cdot 10^{-1}$	A_r (m^2)	$3.22 \cdot 10^{-5}$
P_{atm} (Pa)	$1.01 \cdot 10^{5}$	P_{supply} (Pa)	$5.15 \cdot 10^{5}$
ϕ_a (Pa)	$0.20\hat{P}_{a_d}$	ϕ_b (Pa)	$0.20\hat{P}_{b_d}$
γ_a (kg/s)	$2.62 \cdot 10^{-4}$	γ_b (kg/s)	$4.22 \cdot 10^{-5}$

all the pressures were bounded around the sliding surface (i.e., desired pressures) in all trials. Each row and column show different conditions in terms of the desired stiffness and the equilibrium point, respectively. Five solid colored lines suggest sensor measurements of chamber pressures P_a and P_b in five trials conducted under each experimental condition. Blue areas suggest the range within $\pm 5\%$ of desired pressures. Part of the experimental data (i.e., 1 second from the beginning) was extracted and shown in these figures. A few trials did not stop chattering as shown in Fig. 2.12, however, we confirmed that the behavior stopped within 2 seconds in all trials.

Fig. 2.13 shows the interaction force measured by different sensors when the rod position was moved by the linear actuator as shown in Fig. 2.11. The corresponding solid lines (except a black line) in Fig. 2.13a and 2.13b were collected in the same trial but by different sensors. Fig. 2.13a shows an interaction force measured by the force sensor while Fig. 2.13b shows a pneumatic

force computed based on (2.1) by the pressure data. In both figures, the x-axis shows the rod position measured by the potentiometer. Vertical and horizontal dotted black lines suggest the desired equilibrium point (i.e., l_{eq} =0.05 mm) and the desired force at the equilibrium point (i.e., F_p =0 N), respectively. The solid black line shows the desired force based on the constant desired stiffness (i.e., $K_d = 2.00 \cdot 10^3 \mathrm{N/m}$). Note that when the rod position started to be moved by the linear actuator, rapid rises (i.e., jumps) were confirmed in the force sensor measurements. This phenomenon is not shown in the figure as it appeared at the beginning of the trials.

2.4.3 Discussion

Performance of Proposed Sliding Mode Controller

The objective of these experiments was to validate the performance of the proposed model-based controller, allowing the AP2A to respond as a passive nonlinear spring with controllable stiffness. The SMC was designed as (2.47) and implemented to the microcontroller to tune pressures safely. The guard in Fig. 2.10 switched the discrete states when the differences between the desired and measured pressures on both chambers converged to a specific range. Thus, the performance of the SMC and the guard can be interpreted as that of the proposed controller. The performance of the SMC can be confirmed in Fig. 2.12. Blue areas suggest pressure ranges within $\pm 5\%$ of the desired pressures. Chattering was confirmed around the areas, which are the typical feature of the SMC. Though the pressures chattered, they were bounded around the areas (i.e., sliding surfaces in (2.46)) under all experimental conditions. Therefore, the experimental results suggest that the SMC functioned in all experiments to control the pressures safely in each chamber. Accordingly, the AP2A can function as an active actuator as well as previous studies [69, 70] when the thresholds ε in Fig. 2.10 are set to zero to disable the transition from discrete mode q_1 to q_2. Note that pressures in each chamber chattered differently. One of the reasons may be that the mass flow through two valves (i.e., functions g_i expressed in (2.28)) was not modeled well for precise control, suggesting the need for model improvements if necessary.

Fig. 2.12 also suggests the performance of the guard in Fig. 2.10. The end of chattering can be regarded as a sign of the guard being enabled, as control inputs $\mathbf{u}$ became zero in q_2 (i.e., passive mode). According to Fig. 2.12, the chattering terminated around 0.6 seconds in most of the trials. It was confirmed that, in *all* trials, the behavior terminated within 2 seconds. Besides, the steady-state pressures were within $\pm 5\%$ of desired pressures (i.e., blue areas). Thus, the performance of the guard was validated, demonstrating that the guard was enabled to allow the AP2A to respond as a passive component at the desired pressures. Note that the guard could be enabled sooner by improving the mass flow model. The SMC certifies that each pressure stabilizes in a specific range (2.50) separately. However, the control law does not assure that both pressures remain in the range simultaneously. The switching time was not predictable as simultaneous convergence was not proven. The simultaneous convergence may be demonstrated if the automaton with the SMC (i.e., q_1 in Fig. 2.10) is divided into two discrete modes, which have a single control input $t_{v_1 a}$ and $t_{v_1 b}$ separately.

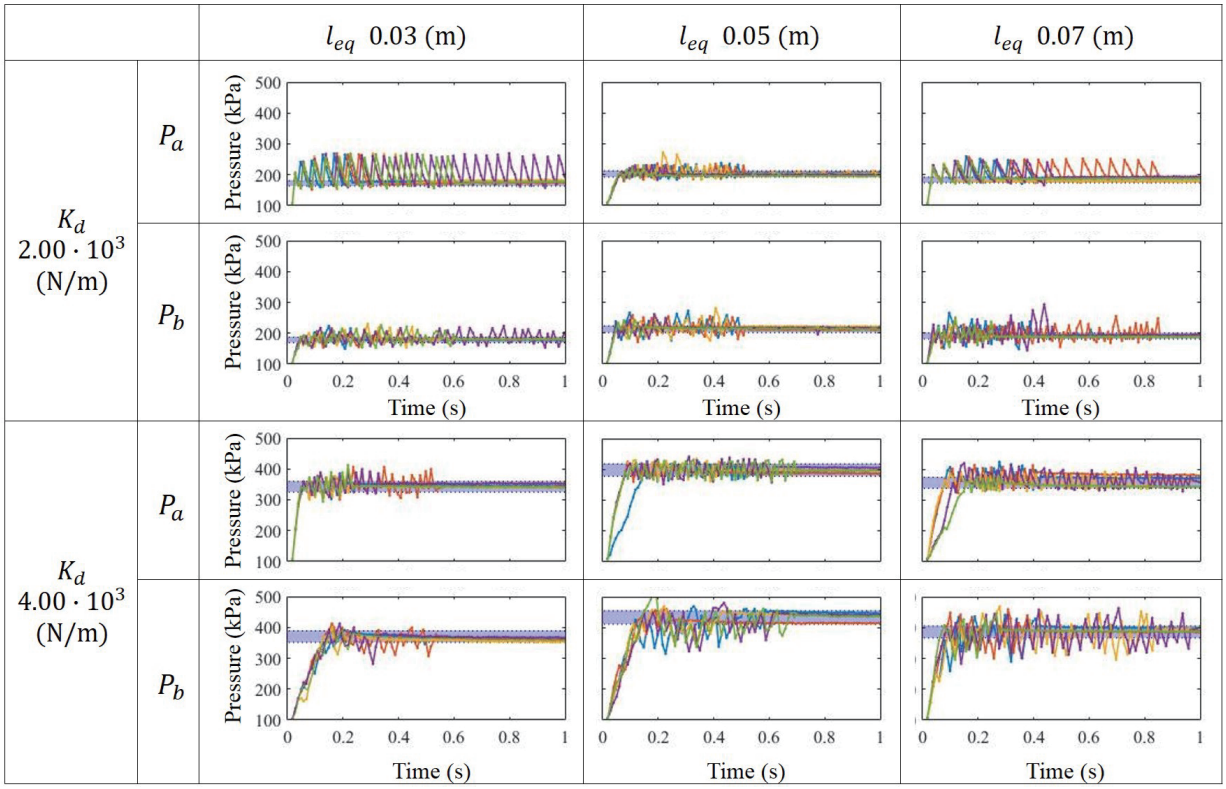

Figure 2.12: Experimental pressure data with the desired stiffness and equilibrium.

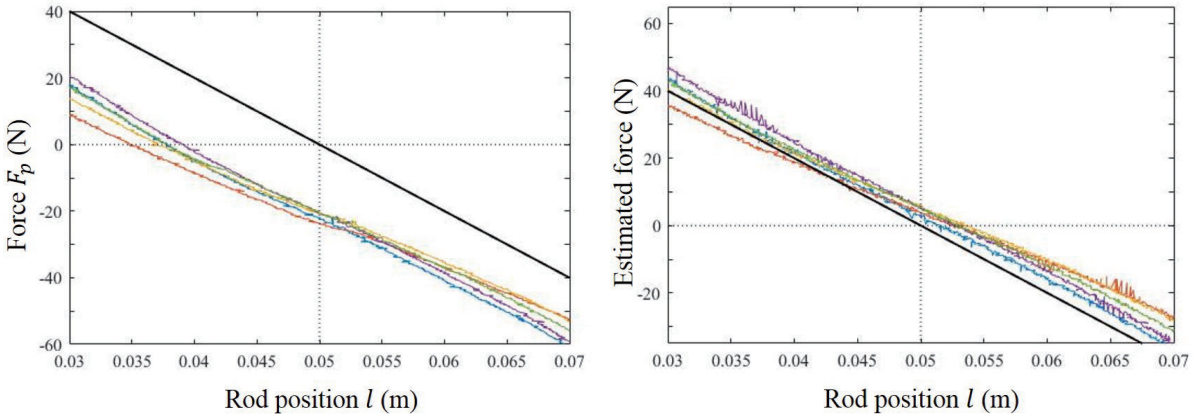

(a) Measured with a force sensor.

(b) Estimated with pressure sensors.

Figure 2.13: References and stiffness curves obtained in the experiments.

Performance as Passive Variable Stiffness Actuator

The effective stiffness of the AP2A in q_2 (i.e., passive mode) was confirmed in Fig. 2.13. The figure shows the desired stiffness as a solid black line. The force sensor measurements show similar stiffness curves between the trials in Fig. 2.13a. This result indicates that the AP2A responded as a passive spring with the desired stiffness. However, errors were found in the y-axis between the curves and the reference. These errors were not confirmed in the estimated pneumatic force by the pressure sensors Fig. 2.13b. As mentioned in section 2.4.2, jumps were measured by the force sensor at the beginning of the actuation of the linear actuator. Thus, these errors may be due to drifts of the force sensor caused by the initial actuation and/or other mechanical factors in interaction force such as frictions. Further investigations are required to confirm the overall performance.

According to the results, the AP2A may be able to handle a broader range of effective stiffness than the variable stiffness actuator (VSA) consists of electrical geared motors. As shown in Fig. 2.12, the pressures also stayed within $\pm 5\%$ of desired pressures when the desired stiffness K_d was set to be $4.00 \cdot 10^3 \mathrm{N/m}$. The desired stiffness is twice as large as that of the VSA with electrical motors [61]. Much higher stiffness may be implementable to the AP2A with a high supply pressure [69].

Limitation

A reduced model in (2.34) was utilized to control pressures with an assumption that the external force F_l is controlled to stabilize the system around the equilibrium point. This assumption may be reasonable for assistive devices with the AP2A. The user can maintain a specific posture for about 1 second, waiting for the pressures to converge. To satisfy safety in any situation, it would be better to use the full state model in (2.29). Another limitation is that the switching controller design in Fig. 2.10 was not able to tune the pressures again. A new edge (q_2, q_1) (i.e., a transition from a discrete mode q_1 to q_2) and the corresponding guard are required to maintain the passive assistance and to avoid continuous switching between the two modes. The limitations above will be further investigated to improve the performance of the AP2A as a passive, variable stiffness actuator in the next section.

2.5 Model-free Control for Passive Variable Stiffness Actuator

A model-based feedback control was introduced in the previous section, which used the SMC. The solenoid valves were utilized to tune the pressures according to the desired pressures calculated in (2.45). Instead of controlling the valve's effective area [69, 70], a valve opening time $t_{v_1 i}$ was used as a control input to tune the pressures. The valve opening time $t_{v_1 i}$ determined the air mass flow of the chamber i. The feedback controller designed the control input $t_{v_1 i}$ based on the current state of chamber pressures P_i.

Reconsidering of the switching algorithm in Fig. 2.3, the algorithm needs to take the wait time t_{wait} into account in each feedback cycle because of the two valves arranged in series. As discussed in section 2.3.3, this drawback limits the bandwidth (i.e., responsiveness) of the AP2A. In terms of a switching controller in Fig. 2.10, it does not guarantee the switching timing from discrete mode q_1 to q_2. In other words, the controller does not grantee when the inequality conditions with thresholds ε in Fig. 2.10 will be satisfied. Accordingly, there is a variation in the switching timing as shown in Fig. 2.12.

A model-free feedforward control utilizing Differential Evolution (DE) is proposed to approach this problem in this section. An overview of the proposed control method is shown in Fig. 2.14. Once the solenoid valve is activated for $t_{v_1 i}$ seconds from the initial condition (i.e., $t = 0$), then the valve is turned off to make the actuator work as a passive spring. It is a kind of one-shot method and no feedback loops, and this approach can reduce the length of time for which the actuator waits for switching to the passive mode.

2.5.1 Differential Evolution for Model-free Pressure Control

After activating the valves for $t_{v_1 i}$ seconds once, the air pressure in the chamber i is expressed as:

$$m_i(t_{v_1 i}) = m_i(0) + \int_0^{t_{v_1 i}} \dot{m}_i(P_u(t), P_d(t))dt \tag{2.52}$$

$$P_i(t_{v_1 i}) = m_i(t_{v_1 i})RT/V_i(t_{v_1 i}) \tag{2.53}$$

where the volume $V_i(t_{v_1 i})$ is dependent on the pneumatic and external forces as described in (2.1) to (2.5). The problem is to find the best valve opening time $t^*_{v_1 i}$ that minimizes differences between

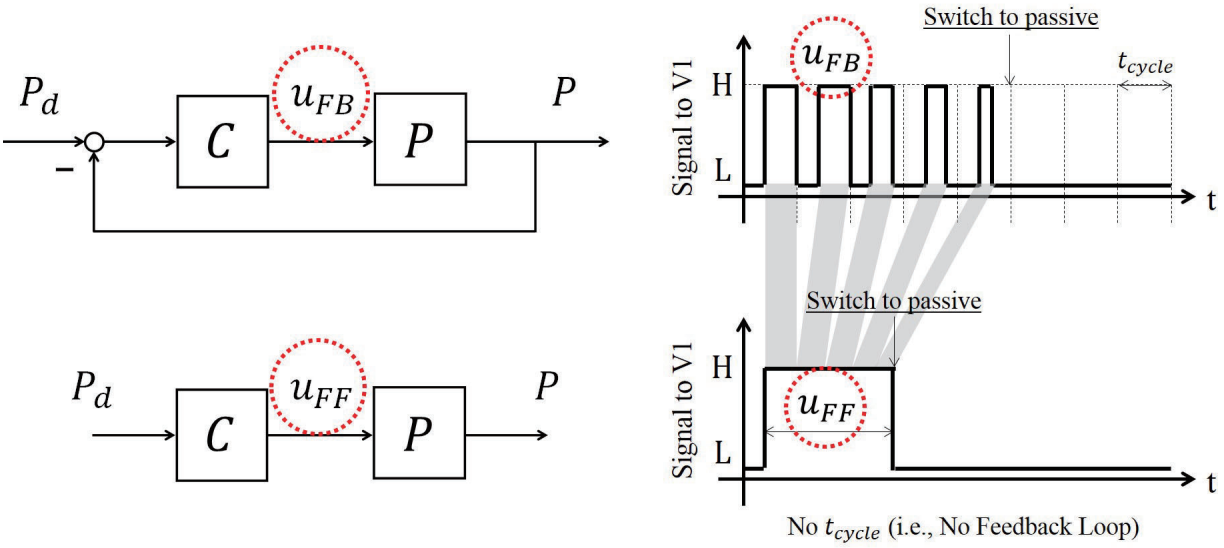

Figure 2.14: Differences between the model-based feedback control and the proposed method.

the chamber pressures P_i and the desired values that are calculated in (2.45). The air flow model in (2.8) or the empirical model such as (2.28) were required to compute suitable valve opening time $t_{v_1 i}$ in each feedback loop when the model-based control was utilized to tune the chamber pressures. Instead, an evolutionary computational algorithm is introduced in this study. These air flow models can be neglected by utilizing the algorithm, which is a model-*free* method.

Differential Evolution for Black-Box Optimization

Evolutionary computational algorithms have been investigated to solve black-box optimization problems, and these algorithms have also been applied to assistive technologies recently. For example, Zhang et al. utilized Covariance Matrix Adaptation Evolution Strategy (CMA-ES) to find the optimal control strategy for an ankle exoskeleton while executing gait assistance [87]. A relatively simple algorithm was chosen in this study, called Differential Evolution (DE) [112]. Showing comparable performance compared to CMA-ES, DE has also been utilized to search for parameters in controllers [113].

Algorithm 1 utilizing DE shows the procedure implemented in our experiments. First of all, target vectors $\mathbf{t}_1 \in \mathbb{R}^{D\times 1}$ in the first generation $\mathbf{P}_1 \in \mathbb{R}^{D\times NP}$ are chosen randomly within the constraints, covering the entire parameter space. Note that D is a dimension of decision variables (i.e., $D = 2$ for the chambers), NP is the size of a population. The k^{th} target vectors in the G^{th} generation $\mathbf{P}_G$ are expressed as:

$$\mathbf{t}_G(k) = [t_{v_1 a_k,G}, t_{v_1 b_k,G}]^T,\ k = 1,...,NP \tag{2.54}$$

$$\underline{t} \leq t_{v_1 i_k,G} \leq \bar{t} \tag{2.55}$$

where $\underline{t}$, $\bar{t} \in \mathbb{R}$ are the lower and upper limits of the valve opening time. With this representation, the initialization process can be written as:

$$\mathbf{t}_1(k) = \underline{t} \cdot \mathbf{1}_{2\times 1} + (\bar{t} - \underline{t}) \cdot \mathbf{X} \tag{2.56}$$

Algorithm 1 Differential Evolution based on [112]

```
procedure
    set parameters NP, F, and CR;
    G ← 1;
    initialize P_G = [ t_G(1), ..., t_G(NP) ] with (2.56), (2.57);
    while J(t_G(best)) > J̄ do
        for k = 1 to NP do
            generate mutants v_G(k) based on (2.59);
            generate trials u_G(k) based on (2.60);
        for k = 1 to NP do
            if J(u_G(k)) ≤ J(t_G(k)) then
                t_G(k) ← u_G(k);
        G ← G + 1;
```

$$\mathbf{X} = [X_1, X_2]^T,\ X_1, X_2 \sim U[0,1] \tag{2.57}$$

The mutant vectors $\mathbf{v}_G(k) \in \mathbb{R}^{D\times 1}$ are then generated based on each target vector as follows:

$$\mathbf{v}_G(k) = [v_{v_1 a_k, G}, v_{v_1 b_k, G}]^T,\ k = 1, ..., NP \tag{2.58}$$

$$\mathbf{v}_G(k) = \mathbf{t}_G(best) + F \cdot (\mathbf{t}_G(r_1) - \mathbf{t}_G(r_2)) \tag{2.59}$$

where $\mathbf{t}_G(best)$ is the target vector showing the best performance among the population $\mathbf{P}_G$, $r_1, r_2 \in \{1, ..., NP\}$ are random, non-equal integers, and $F \in (0,1]$ is a constant scalar. Note that if the mutant vectors do not satisfy the constraints (2.55), then the vectors are computed again using (2.59) until they satisfy the conditions. In the next step, crossover is introduced to generate trial vectors $\mathbf{u}_G(k) \in \mathbb{R}^{D\times 1}$ such that:

$$u_{v_1 i_k, G} = \begin{cases} v_{v_1 i_k, G}, & Y \leq CR \parallel i = Z_i \\ t_{v_1 i_k, G}, & Y > CR \bigwedge i \neq Z_i \end{cases} \tag{2.60}$$

where Y is a random variable with a uniform distribution computed for each i^{th} element ($i \in \{1, ..., D\}$, and in this study $D = 2$ as $i \in \{a, b\}$), $Z_i \in \{1, ..., D\}$ is a random integer for the k^{th} vector to guarantee that the trial vector includes at least one element from the corresponding mutant vector. $CR \in [0,1]$ is the crossover constant scalar. In the end, the population $\mathbf{P}_G$ is updated by comparing the performance of the target vector $\mathbf{t}_G$ with that of the trial vector $\mathbf{u}_G$. The performance is graded based on the following cost function:

$$J(\mathbf{s}_G(k)) = \sqrt{(P_a(\mathbf{s}_G(k)) - P_{a_d})^2 + (P_b(\mathbf{s}_G(k)) - P_{b_d})^2} \tag{2.61}$$

where $\mathbf{s}_G(k)$ is either the target vector $\mathbf{t}_G(k)$ or the trial vector $\mathbf{u}_G(k)$. P_i is measured chamber pressure after opening the valves for $t_{v_1 i_k, G}$, and P_{i_d} is the desired pressures computed using (2.45) with the measured rod position. If the trial vector performs better than the target vector, then the trial vector is replaced with the target vector in order to generate a new population $\mathbf{P}_{G+1}$. Otherwise, the target vector is retained in $\mathbf{P}_{G+1}$. This sequence of procedures is repeated to search for the best control inputs that meet the stated requirement (i.e., $J \leq \bar{J}$ in Algorithm 1).

2.5.2 Experimental Validation

Experimental Setups

Fig. 2.15 shows the experimental setups for the second experiment to implement the control method with DE. A 0.75 inch bore, 3 inch stroke cylinder was used in these experiments (Bimba, SR-043-D). A potentiometer was attached to the rod to measure the position of the rod. The valve array consisted of two 5-port solenoid valves (SMC, SY7340-5GZ). Note that the valve used in this experiment was different from the previous experiment in section 2.4.2. An air compressor with a regulator provided the cylinder with compressed air at 600 kPa (= P_{supply}). Three pressure sensors (Omega, PX40-100G5V) were utilized to measure the supply pressure and pressures in the

chambers (i.e., P_{supply} and P_i). A DC geared motor (Maxon, EC60flat with GP52C) with a dedicated motor driver (Maxon, Escon50/5) was introduced to control the rod position of the cylinder. A microcontroller (STM32, F746ZG) sent feedback of the rod position to control the geared motor. It also sent the control signals to the solenoid valves to activate them for a certain time according to outputs from the DE algorithm (i.e., $t_{v_1 i}$). The microcontroller sampled all the sensors and logged the data on a laptop via serial communication. The DE algorithm ran on the laptop with `MATLAB 2016b`, and a new generation $\mathbf{P}_{G+1}$ was computed based on the measured data.

Experimental Conditions

Two experiments were conducted with the model-free controller. The first experiment was conducted with a fixed rod position. In this experiment, the performance of the proposed method using DE was evaluated on its ability to tune the air pressures in the chambers precisely. The desired stiffness and equilibrium point were set at $K_d = 4.00 \cdot 10^3 \mathrm{N/m}$ and l_{eq} =38.0 mm, respectively. According to these desired values, the desired pressures were computed as a solution of (2.43) to (2.45) on the laptop. Note that the geared motor was also controlled to fix the rod position at 38.0 mm during the experiment.

The second experiment was conducted under the dynamic condition. The aim of this experiment was to confirm the performance of the proposed method under a practical situation where

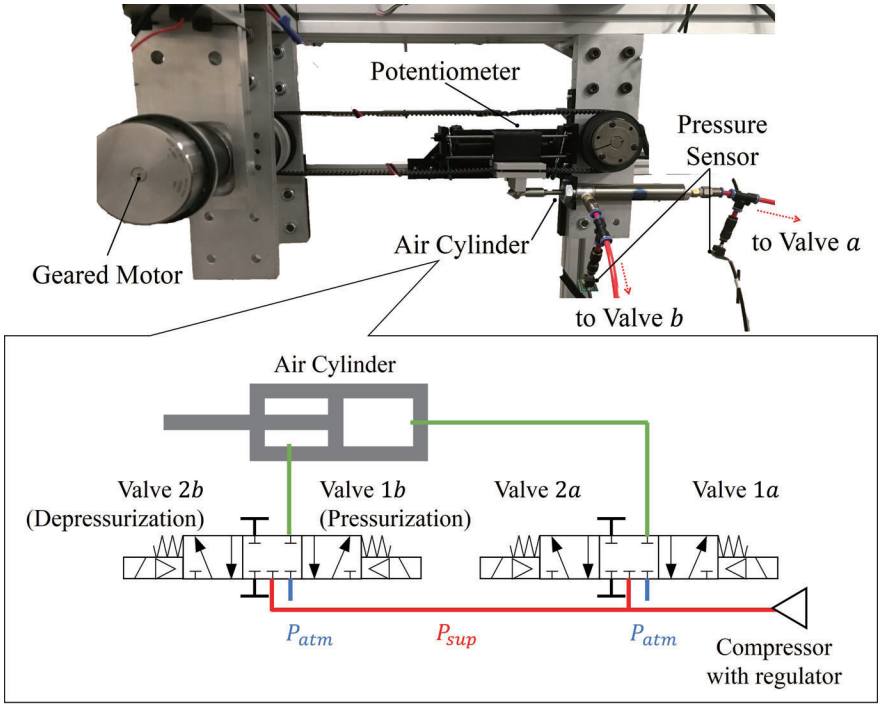

Figure 2.15: Experimental setups and a schematic of the pneumatic system.

the rod position was repeatedly modified by external forces. In this experiment, the AP2A was expected to function as a semi-active variable stiffness actuator as described in Fig. 2.16. Note that an identical state machine for chamber b was implemented in the experiment, but it is omitted from Fig. 2.16. In Mode1, both chambers were connected to atmospheric sources so that the cylinder did not experience any internal forces that would move its rod. When the rod position exceeded a threshold (i.e., $l_{thre} = 38.0\,\text{mm}$ in Fig. 2.16) due to the external force, the mode transitioned from Mode1 to Pre-Mode2. The air pressures were then tuned in order to function as a passive spring with desired stiffness in Mode2. The desired stiffness and equilibrium point in Mode2 were set at $K_d = 4.00 \cdot 10^3 \text{N/m}$ and l_{eq} =48.0 mm, respectively. In Pre-Mode2, the solenoid valves were opened to the supply pressure source for a certain time (i.e., $t_{v_1 i}$) according to the outputs from the DE algorithm. The mode transitioned from Pre-Mode2 to Mode2 after the pressurization, and both chambers were closed so that the cylinder performed as the passive spring.

Note that the geared motor was persistently actuated to control the rod position in the second experiment. The motor started from $l < l_{thre}$, and it rotated with $\dot{l} > 0$ at a constant speed until the rod position satisfied, $l > l_{thre}$+5 mm. After one second, the motor rotated the opposite direction until the rod position became, $l < l_{thre}$−15 mm. This pattern of movements was repeated for 25 iterations, within 15 seconds per iteration.

In both experiments, the size of the population NP was set to be 25, and the constant values F, CR were determined empirically to be 0.36 and 0.55, respectively. DE algorithm was terminated when the minimum cost among the population $J(\mathbf{u}_{i,G})$ became smaller than the following condition $\bar{J}$:

$$\bar{J} = \sqrt{(0.05 \cdot P_{a_d})^2 + (0.05 \cdot P_{b_d})^2} \tag{2.62}$$

All the parameters explained in the above sections are summarized in Table 2.2.

Experimental Results

In terms of the two experiments with the second experimental setups, it took at most 5 minutes to confirm the cost of all the trial vectors (i.e., $J(\mathbf{u}_G(k))$) in a population $\mathbf{P}_G$. In the first experiment,

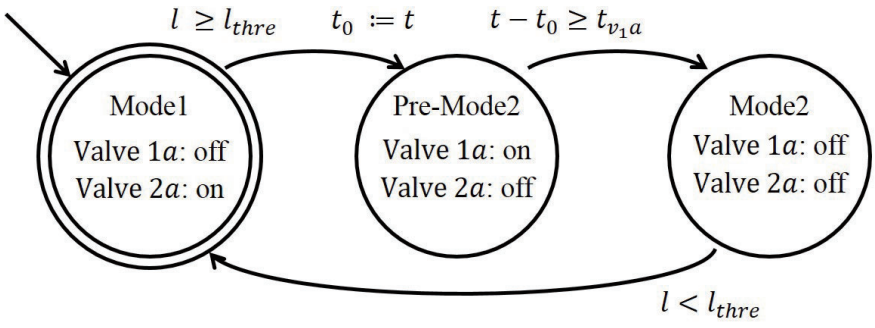

Figure 2.16: Function of solenoid valves for the chamber a in the second experiment.

Table 2.2: Parameters of experimental setups in Fig. 2.15

Params (unit)	Value	Params (unit)	Value
A_a (m^2)	$2.85 \cdot 10^{-4}$	A_b (m^2)	$2.53 \cdot 10^{-4}$
A_r (m^2)	$3.22 \cdot 10^{-5}$	P_{atm} (Pa)	$1.01 \cdot 10^{5}$
R ($\mathrm{J}/(\mathrm{kg} \cdot \mathrm{K})$)	$2.87 \cdot 10^{2}$	T (K)	$2.93 \cdot 10^{2}$
D	2	NP	25
$\bar{t}$ (ms)	$2.00 \cdot 10$	$\underline{t}$ (ms)	0.00
F	$3.60 \cdot 10^{-1}$	CR	$5.50 \cdot 10^{-1}$

the minimum cost J in the third generation became smaller than the requirement (2.62). Fig. 2.17 shows the progress in the population between the first and third generations (i.e., $\mathbf{P}_1$ and $\mathbf{P}_3$). The black plots in Fig. 2.17 (i.e., 25 black dots) indicate each target vector in the population. Fig. 2.17a and 2.17b show the plots in three-dimensional space (cost J as a function of valve opening times $t_{v_1 i}$). Fig. 2.17c and 2.17d show the plots in two-dimensional space of the valve opening times, omitting the vertical axis and associated cost, J. Dotted green squares in these figures indicate borders of the black plot. The best inputs and the corresponding cost were:

$$\mathbf{t}_3(best) = [7.5, 7.1]^T,\ J(\mathbf{t}_3(best)) = 9.41 \tag{2.63}$$

where $\mathbf{t}_3(best)$ is reported in milliseconds. At that time, the desired pressures and the measured values were:

$$\begin{cases} [P_{a_d}, P_{b_d}] = [319, 261]^T \\ [P_a, P_b] = [310, 259]^T \end{cases} \tag{2.64}$$

where the pressures are reported in kilo-pascal.

In the second experiment, the minimum cost J became smaller than (2.62) in the fourth generation. Fig. 2.18 shows the progress of the population between the first and fourth generations. The best inputs and the corresponding cost were:

$$\mathbf{t}_4(best) = [14.6, 15.3]^T,\ J(\mathbf{t}_4(best)) = 9.38 \tag{2.65}$$

The corresponding desired pressures and the measured pressure values were:

$$\begin{cases} [P_{a_d}, P_{b_d}] = [269, 259]^T \\ [P_a, P_b] = [263, 252]^T \end{cases} \tag{2.66}$$

2.5.3 Discussion

Validation of Differential Evolution

Fig. 2.17 and 2.18 show the progress of the population between the first and the last generation in which the best inputs were found. As shown in Fig. 2.17c and 2.18c, the population in the first

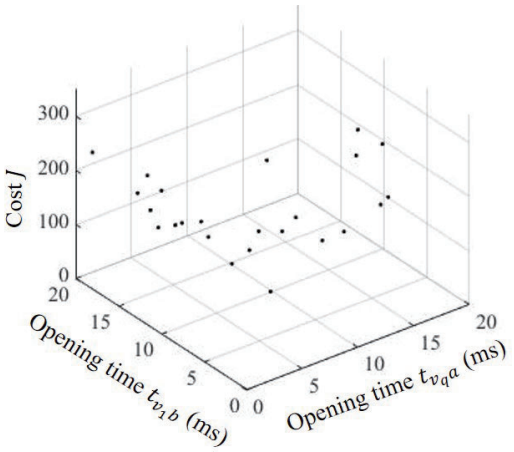

(a) Experimental data of the 1^{st} generation.

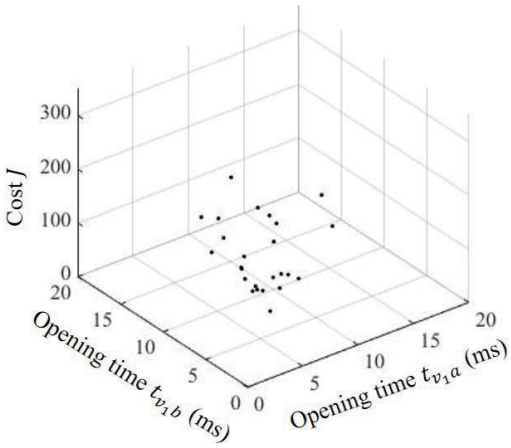

(b) Experimental data of the 3^{rd} generation.

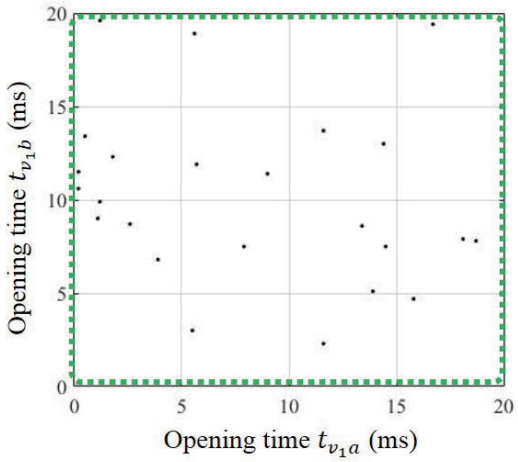

(c) Projection of Fig. 2.17a.

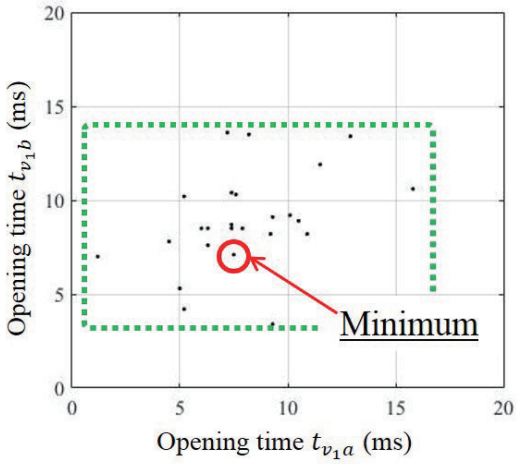

(d) Projection of Fig. 2.17b.

Figure 2.17: Progress of experimental data using the DE while fixing the rod.

generation were uniformly distributed within the range of inputs (i.e., $t_{v_1 i}$) according to (2.56), searching thoroughly for the best inputs. After finding the inputs showing the best performance among the population, the algorithm (DE) started to focus on searching around those inputs based on (2.59). These results can be confirmed by comparing Fig. 2.17c with 2.17d (or Fig. 2.18c with 2.18d) that a border (i.e., a green square) of the plots shrank around the inputs showing the minimum cost.

Performance of Model-free Controller

Empirical results from the first experiment suggest that the proposed control method could be useful to tune the pressures in the chambers. The experimental conditions of the first experiment

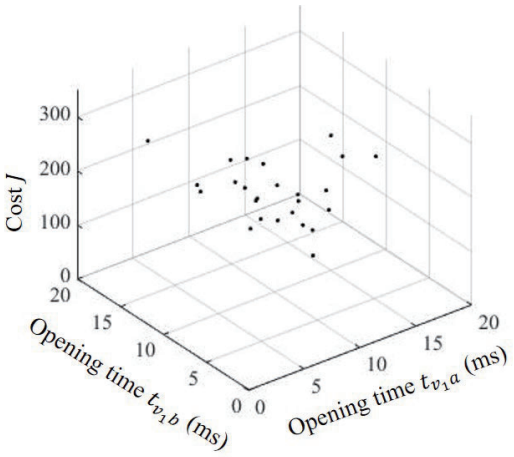

(a) Experimental data of the 1^{st} generation.

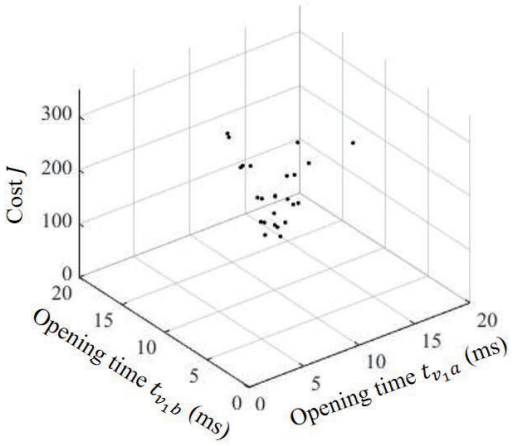

(b) Experimental data of the 4^{th} generation.

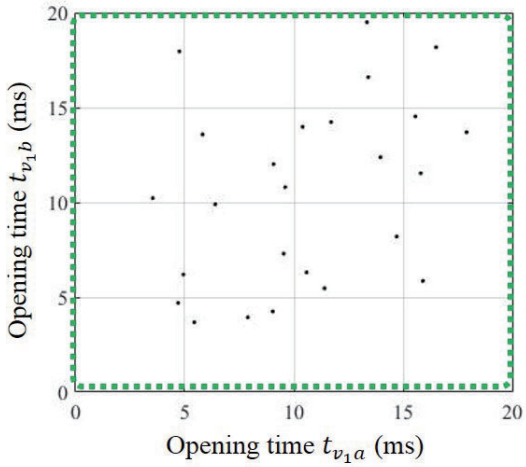

(c) Projection of Fig. 2.18a.

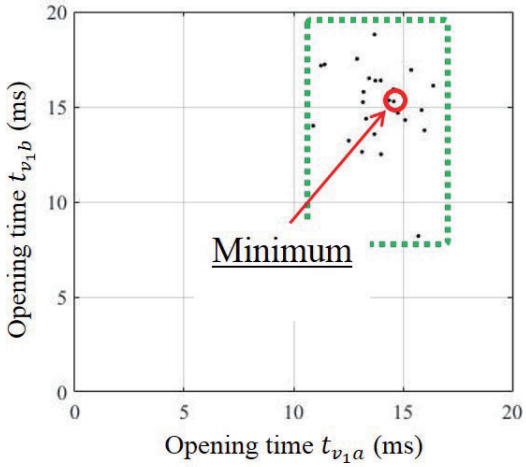

(d) Projection of Fig. 2.18b.

Figure 2.18: Progress of experimental data using the DE while moving the rod.

were similar to those of the experiment conducted in section 2.4, with the exception of the choice of control methods. The desired stiffness and equilibrium point were set to be constant, and the rod position was fixed by the external force provided by the motor during the experiment. In section 2.4, a modified PWM signal designed by the algorithm in Fig. 2.3 was utilized to tune air flow with solenoid valves. The PWM method was able to compensate for uncertainties in the flow model within the feedback loop. However, the rising time of the PWM method was relatively slow (around 50 milliseconds) due to the high frequency of valve opening and closing utilized to achieve the feedback control. In comparison, the proposed method requires less than 10 milliseconds to reach the desired pressures, as shown in (2.63). Beyond this fact, the proposed method was able to switch to the passive mode right after activation without chattering, while the previous method required around 500 milliseconds. In terms of the steady-state errors, both control methods were

able to tune the steady-state pressures within $\pm 5\%$ of desired pressures. These results indicate that the proposed control method could be useful to make the air cylinder work as a passive nonlinear spring.

The second experiment was conducted for further investigation on the abilities of the proposed control method. In section 2.4, an assumption was built that the rod position of the actuator was fixed during the pressure control. The first empirical results such as Fig. 2.17 suggested that, with the model-free control method, the air pressures could reliably be tuned to the desired values under similar experimental conditions in section 2.4. However, in practice, the assumption may not be satisfied when the AP2A is utilized for assistive devices. The second experiment was thus conducted to confirm if the proposed method also works in a dynamic situation. Since the external force controlled the rod position, the dynamics of the cylinder were different from the first experiment based on (2.1) to (2.5). Nonetheless, the steady-state pressures were also within $\pm 5\%$ of the desired pressures as shown in (2.66). In this sense, the proposed method is said to have an ability to tune the pressures both in the static and dynamic situations.

One of the most interesting results is that the best valve opening times (2.65) were longer than that of the first experiment (2.63), though the desired pressures (2.66) were smaller than those of the first experiment (2.64). These results are counter-intuitive, however, the proposed control method could handle unexpected characteristics of hardware and/or software. In this study, the FSM shown in Fig. 2.16 was implemented correctly in the microcontroller. However, there was an additional mode in between Mode 1 and Pre-Mode 2 due to delays in response times (i.e., the mode with Valves 1a and 2a to be *on*). This unexpected characteristics of hardware forced the valve opening time to be longer than the expected time.

Limitation

One of the major limitations of the proposed method is that it requires the collection of empirical data in each situation before using the device. It is made obvious by comparing the first and the second experimental results. The proposed model-free method may be time-consuming and may not be suitable for people with disabilities in some cases. However, it took around 20 minutes to search the optimal inputs in both experiments. Besides, the cylinder may be tuned to perform as the desired passive spring in advance by utilizing the knowledge of human modeling and optimization [114].

Another limitation is that the proposed method is not robust to unexpected motion when compared to the model-based method in section 2.4. Since the air cylinder is expected to work as a passive spring in repetitive tasks, environmental changes (e.g., sudden changes of movements provided by the geared motor) were not considered.

2.6 Summary

This chapter introduced an Active/Passive Pneumatic Actuator (AP2A) whose dynamic responses (i.e., mechanical impedance) can be actively modified according to the desired values. The AP2A consists of a pneumatic actuator and an array of solenoid valves. Section 2.2 described an air flow model with a switching algorithm as well as a mathematical model of a pneumatic actuator. In the following section, a model-based force (i.e., pressure) control was achieved with the models. In section 2.4, the pressure controller was applied to two chambers in order to achieve simultaneous control of equilibrium and stiffness of the actuator. A switching controller was also included in the pressure controller to make the AP2A function as a nonlinear mechanical spring. Experimental results suggest that the chamber pressures were controlled around $\pm 5\%$ of the desired pressures under several conditions. The AP2A could switch its mode to function as a passive spring once both pressures reach within $\pm 5\%$ of the desired value. In the last section 2.5, a model-free controller was further investigated for the switching control with the evolutionary algorithm (i.e., Differential Evolution). This model-free controller enabled the AP2A to switch its mode faster than the model-based controller (i.e., 10 ms and 500 ms, respectively). Besides, the controller did not require the air flow model which takes time to identify under several conditions. From the above, design and low-level controllers of the AP2A were characterized through experiments.

Chapter 3

Active/Passive Switching Control Framework

3.1 Chapter Overview

This chapter introduces a high-level controller of assistive systems utilizing an Active/Passive Pneumatic Actuator (AP2A). A physical plant (i.e., users of assistive devices) may take actions based on its objectives that vary according to situations. In these situations, the high-level controller designs a control law to achieve transparent interaction (i.e., neither to assist nor to disturb the plant). Once the plant engages in specific tasks, these objectives are assumed to be invariant. Under those specific tasks, a computational method is required to search for desired behavior (i.e., mechanical characteristics) of the AP2A to cooperate with the physical plant efficiently. Dynamic responses of the AP2A can be modified according to desired pressures, as discussed in chapter 2. The high-level controller is designed to compute the desired pressures which enable to assist the physical plant while improving the energy efficiency of the actuator. A simulation study is conducted to validate the performance of the high-level controller, utilizing a numerical model of a pendulum which imitates elbow joint movements of a human. The simulation results suggest that the proposed controller can compute desired pressures balancing assistance and energy consumption of the AP2A.

3.2 System Design and Modeling

Fig. 3.1 shows a proposed system that incorporates the AP2A, assuming that the rotational axis of external sources (e.g., human joints or electrical motors of robots) is aligned to that of an orange connector. The AP2A is a linear actuator as described in Fig. 2.1, while mechanical joints actuated by electrical motors or human joints are mainly rotational joints. A movable range of the rod could limit the joint motions. A transmission system is introduced to modify a relation between the linear rod position of the AP2A and the rotational angle. With these setups, a rotation of the joint angle

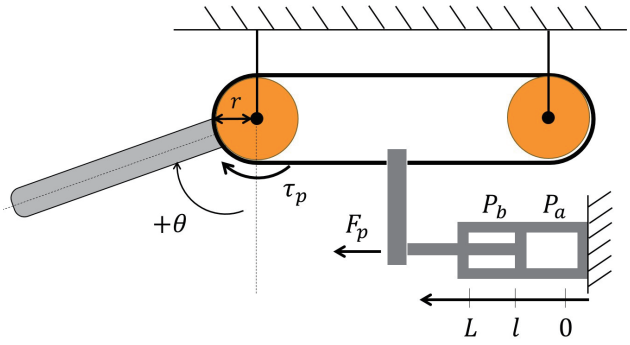

Figure 3.1: Schematics of the connection between the AP2A and a sub-assembly.

θ results in a linear translation of the rod position l via the transmission such as Bowden cables. The relation can be expressed as follows:

$$l := l_0 + r\theta \tag{3.1}$$

where r is a radius of the connector, and an assistive torque τ_p is also dependent on the radius as follows:

$$\tau_p := F_p r \tag{3.2}$$
$$F_p := P_a A_a - P_b A_b - P_{atm} A_r \tag{3.3}$$

where F_p is a force produced by the pneumatic actuator, P_i are pressures in the chamber i, A_i are corresponding effective areas calculated from the bore of the actuator, A_r is a cross-sectional area of a rod, and P_{atm} is atmospheric pressure, respectively. Note that the radius r can be tuned for specific purposes with novel hardware design [115]. The model in Fig. 3.1 can be expressed with a continuous state vector $\mathbf{x} \in \mathbb{R}^5$ as follows:

$$\mathbf{x}(t) := [\theta, \dot{\theta}, l, P_a, P_b]^T \tag{3.4}$$

The dynamics around the joint can be modeled as:

$$I\ddot{\theta} + \tau_f = \tau_p + \tau_g + \tau_{ext} \tag{3.5}$$

where I is the effective inertia of the arm sub-assembly, τ_f is friction in the system, τ_g is a gravitational torque, and τ_{ext} is other external torques applied to the system. Note that the term τ_f includes several nonlinear frictional effects [116] arising in the cable-transmission system. However, these effects are neglected except for dynamic friction in this study. The dynamics can then be simplified as:

$$I\ddot{\theta} + B\dot{\theta} = \tau_p + \tau_g + \tau_{ext} \tag{3.6}$$

where B is the damping coefficient. The gravitational torque τ_g is expressed as:

$$\tau_g := -mgl_f sin(\theta) \tag{3.7}$$

where m is the mass of the arm-assembly and other external loads, g is the gravitational acceleration, and l_f is a length between a rotational axis and an effective center of mass. The external joint torque τ_{ext} is dependent on the system design. The AP2A is applied to a robot arm (i.e., a single joint pendulum) and an exoskeleton (i.e., Active/Passive EXoskeleton, APEX) in this dissertation. In these applications, the external torque is assumed to be a torque provided by an actuator or a human user. More details are described in the following sections and chapter 5, respectively.

The dynamics of the chamber pressures of the AP2A can be described based on the ideal gas law. Under the assumptions of the perfect gas:

$$\begin{aligned} P_i &= m_i RT/V_i \\ V_a &:= A_a l \\ V_b &:= A_b(L-l) \end{aligned} \tag{3.8}$$

where V_i and m_i are a volume and mass of the air in the chamber i, R is the gas constant, T is a temperature of the air, and L is a stroke of the cylinder. Assuming the temperature to be constant (i.e., isothermal condition), derivatives of (3.8) are expressed as:

$$\dot{P}_a = (\dot{m}_a RT - P_a\dot{l})/l \tag{3.9}$$

$$\dot{P}_b = (\dot{m}_b RT + P_b\dot{l})/(L-l) \tag{3.10}$$

where $\dot{m}_i$ is a mass flow of air entering or leaving the chamber i.

A representation of hybrid systems is utilized to describe a numerical model of the AP2A. A state of Valve 1 (V1) in Fig. 2.1 switches dynamics of the chamber pressures, as discussed in section 2.2. It is reasonable to model the AP2A as two different dynamical systems based on the state of V1. Hybrid systems combine discrete and continuous systems [17, 117] and are also called as impulsive/switched systems [118]. They offer a highly versatile method to represent systems whose dynamics change in time such as biped robots. According to definition 3.1 in [117], a hybrid automaton H is a collection $H = (Q, X, f, Init, Dom, E, G, Re)$, where Q is a set of discrete systems, X is a set of continuous states, $f(\cdot,\cdot,\cdot)$ is a vector space, $Init$ is a set of initial states, $Dom(\cdot)$ is a domain, $E(\cdot,\cdot)$ is a set of edges, $G(\cdot,\cdot)$ is a guard condition, and $Re(\cdot,\cdot)$ is a reset map. Fig. 3.2 shows the model which is utilized in the following simulation study. The model is expressed as follows; $Q : q_1, q_2$, X : (3.4), f : (3.11), (3.12), $Init$: (3.13), Dom : (3.14), E : (3.15), G : (3.16), (3.17), (3.18), Re : (3.23), (3.24).

In Fig. 3.2, there are two discrete modes defined as *no-assist* and *passive* mode (i.e., q_1 and q_2). The only difference between these two modes is the discrete state of Valve 1 (i.e., on/off) in Fig. 2.1. In q_1, the pressures are constant at atmospheric pressure as Valve 1 is kept open. Accordingly, there is no torque produced by the AP2A (i.e., $\tau_p = 0$) as derived by (3.2), achieving

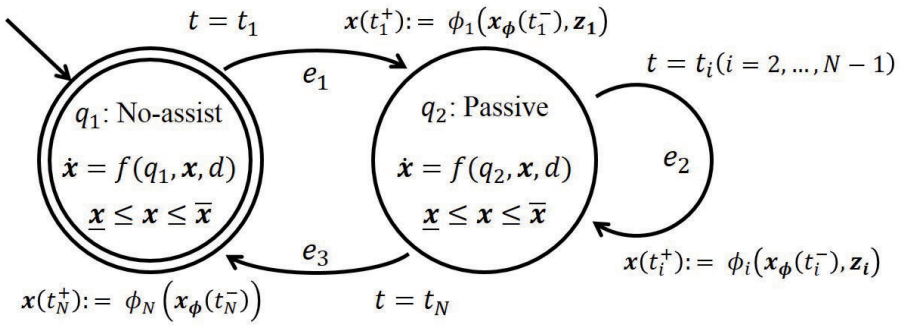

Figure 3.2: Numerical model of the system utilizing the AP2A described with hybrid systems.

transparent interaction with the external torque. On the other hand, the amount of air in each chamber is maintained in q_2. The air mass flow $\dot{m}_i$ in (3.9), (3.10) is equal to zero in q_2. Note that the amount of air is modified instantaneously during every transition (i.e., resets of each edge).

Dynamics in two discrete modes are thus modeled with the continuous state vector $\mathbf{x}$ in (3.4) as follows:

$$\dot{\mathbf{x}} = f(q_1, \mathbf{x}, d) = \begin{bmatrix} \dot{\theta} \\ (-B\dot{\theta} + \tau_p + \tau_g + \tau_{ext})/I \\ r\dot{\theta} \\ 0 \\ 0 \end{bmatrix} \tag{3.11}$$

$$\dot{\mathbf{x}} = f(q_2, \mathbf{x}, d) = \begin{bmatrix} \dot{\theta} \\ (-B\dot{\theta} + \tau_p + \tau_g + \tau_{ext})/I \\ r\dot{\theta} \\ -P_a\dot{l}/l \\ P_b\dot{l}/(L-l) \end{bmatrix} \tag{3.12}$$

where the input d is replaced with the external torque. The initial states $Init(q_1, \mathbf{x}(0))$ is defined as follows:

$$\mathbf{x}(0) := [\theta_0,\ 0,\ l_0 + r\theta_0,\ P_{atm},\ P_{atm}]^T \tag{3.13}$$

Domains of q_1 and q_2 are common and expressed as:

$$\begin{aligned} Dom(q_1) &= Dom(q_2) := \{\mathbf{x} \in \mathbb{R}^5 \mid \underline{\mathbf{x}} \le \mathbf{x} \le \overline{\mathbf{x}}\} \\ \underline{\mathbf{x}} &:= [\underline{\theta},\ -\infty,\ 0,\ P_{atm},\ P_{atm}]^T \\ \overline{\mathbf{x}} &:= [\overline{\theta},\ \infty,\ L,\ P_{supply},\ P_{supply}]^T \end{aligned} \tag{3.14}$$

where $\theta_0, \underline{\theta}, \overline{\theta}$ are initial, lower, and upper bound of the joint angle, and P_{supply} is the supply pressure from a compressor.

The model in Fig. 3.2 has three edges (i.e., three transitions between modes), and these edges are defined as follows:

$$Edge := \{e_1, e_2, e_3\} = \{(q_1, q_2), (q_2, q_2), (q_2, q_1)\} \tag{3.15}$$

For simulation studies[1], guards are defined based on time t to enable the edges as follows:

$$G(e_1) := \{t \in \mathbb{R} \mid t = t_1\} \tag{3.16}$$
$$G(e_2) := \{t \in \mathbb{R} \mid t = t_i\} \tag{3.17}$$
$$G(e_3) := \{t \in \mathbb{R} \mid t = t_N\} \tag{3.18}$$

$$t_0 = 0 \leq t_1 \leq t_2 \leq ... \leq t_N \leq t_{N+1} = T_{end} \tag{3.19}$$

where $i = 2, ..., N-1$, N is the total number of switching, and T_{end} is a termination time, assuming that a physical plant (e.g., users of assistive devices) starts and ends its task at $t = 0$ and $t = T_{end}$. The condition (3.16) suggests that a guard corresponding to e_1 (i.e., $G(e_1)$) is set to be $t = t_1$, and thus, the mode switches from q_1 to q_2 at time t_1. Notice that the assistance provided by the AP2A is implicitly dependent on these guard conditions corresponding to each edge. The switching times are thus chosen as a decision vector $\xi \in \mathbb{R}^N$ as follows:

$$\xi = [t_1, t_2, ..., t_N]^T \tag{3.20}$$

Resets correspond to e_1 and e_2 are designed to optimize the assistance in q_2 (i.e., *passive* mode) during $t \in [t_j, t_{j+1})$ for $j = 1, ..., N-1$. The pneumatic torque τ_p provided by the AP2A is dependent on the pressures P_a and P_b, as described in (3.2). A decision vector $\mathbf{z} \in \mathbb{R}^{2(N-1)}$ is selected, expressing the pressures after transitions as follows:

$$\mathbf{z} := [z_1, z_2, ..., z_{2(N-1)}]^T \tag{3.21}$$

$$\underline{\mathbf{z}} \leq \mathbf{z} \leq \overline{\mathbf{z}} \tag{3.22}$$

where $\underline{\mathbf{z}}, \overline{\mathbf{z}} \in \mathbb{R}^{2(N-1)}$ are the lower and upper bounds of the decision vector and set to be vectors of P_{atm} and P_{supply}, respectively. With the vector of desired pressures $\mathbf{z}$, the resets are defined corresponding to the edges e_1, e_2 at time t_j as $\phi_j : \mathbb{R}^3 \times \mathbb{R}^2 \to \mathbb{R}^5$ such that:

$$Re(e_1, \mathbf{x}) = Re(e_2, \mathbf{x}) := \phi_j(\mathbf{x}_\phi(t_j), \mathbf{z}_j) \tag{3.23}$$

$$\begin{aligned} \phi_j(\mathbf{x}_\phi(t_j), \mathbf{z}_j) &:= [\mathbf{x}_\phi(t_j)^T, \mathbf{z}_j^T]^T \\ \mathbf{x}_\phi &:= [\theta, \dot{\theta}, l]^T \\ \mathbf{z}_j &:= [z_{2j-1}, z_{2j}]^T \end{aligned}$$

[1]For physical assistive devices, the guards in (3.16) and (3.18) can be replaced with sensory feedback from sensor components which detects assistive timings as discussed in Fig. 1.10.

The reset for e_3 at time t_N, $\phi_N : \mathbb{R}^3 \to \mathbb{R}^5$, is defined as:

$$Re(e_3, \mathbf{x}) := \phi_N(\mathbf{x}_\phi) \tag{3.24}$$

$$\phi_N(\mathbf{x}_\phi) := [\mathbf{x}_\phi^T, P_{atm}, P_{atm}]^T$$

Fig. 3.3 shows the relations between the discrete modes (q_1 and q_2) and the decision variables (ξ and $\mathbf{z}$). The vector $\mathbf{z}_j$ is shown in square brackets, and each column suggests chamber pressures $P_a(t_j^+)$ and $P_b(t_j^+)$ in q_2, respectively. The decision variables t_i in ξ are shown on the horizontal axis, and they describe the switching timing. Note that, with this model, the pressures are assumed to be modified to their desired values instantaneously in each transition, as time delay due to these edges is neglected in this study.

Problem Formulation

It is important to decide a cost function governing the optimization of the decision vectors, ξ and $\mathbf{z}$. The traditional controller design of the assistive device reduces the energy expenditure of external actuators or the users (e.g., muscle exertions [76]). At the same time, reducing the energy consumption of the assistive device is essential to prolong operational time. Therefore, two factors are taken into consideration, i.e., the energy cost of the external source J_{ext} and that of the AP2A J_{ap}.

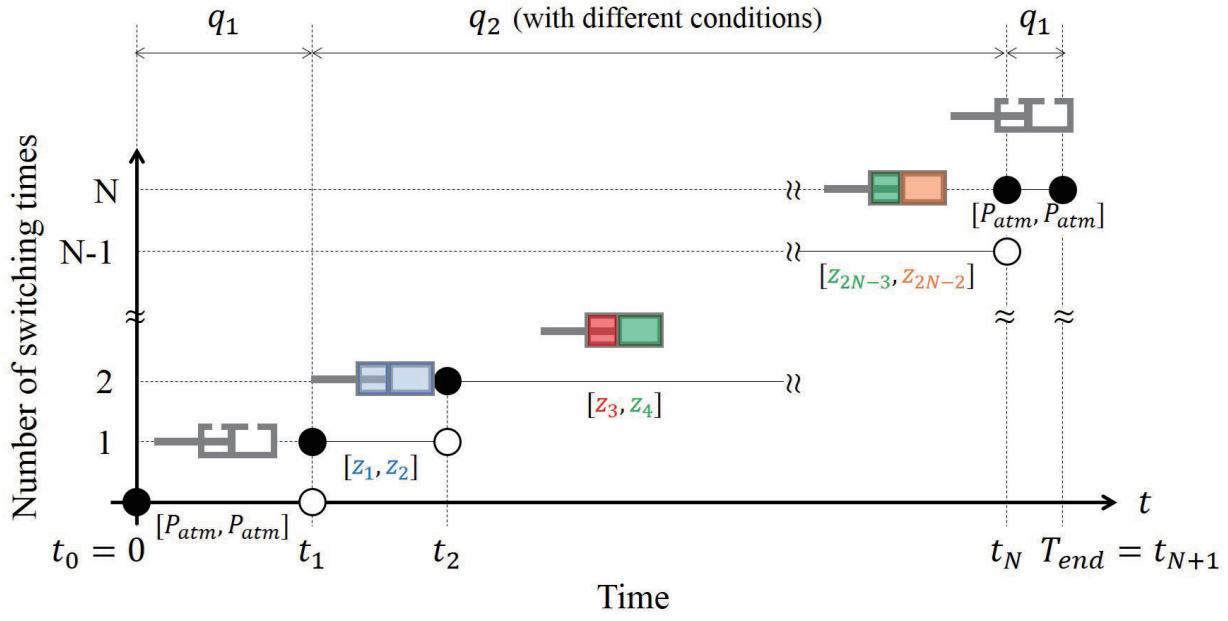

Figure 3.3: Another representation of the model in Fig. 3.2.

The energy cost J_{ext} relates to joint torques, as the external power (e.g., electricity) is converted into the torque to perform tasks via external actuators. In classical physics, work that the torque acts on the joint is equal to the energy consumed by the system such that:

$$W_{t_0 \to t_1} = \int_{t_0}^{t_1} (\tau_{ext} \frac{d\theta}{dt}) dt \tag{3.25}$$

According to this equation, the system neither does any work nor consumes energy when the angular velocity is equal to zero. It means that human does not consume any energy when they flex their elbow joints to lift objects and retain the posture (i.e., $\theta(t) = \theta_0$). This result is not realistic, as work considered in classical physics neglects thermal energy and so forth. From the above, the energy cost of the external source J_{ext} is defined as the amount of torque produced in the task as follows:

$$\begin{aligned} J_{ext}(\xi, \mathbf{z}) &:= \int_0^{T_{end}} L_1(\mathbf{x}(t \mid \xi, \mathbf{z})) dt \\ &= \int_0^{T_{end}} \tau_{ext}^2(t \mid \xi, \mathbf{z}) dt \end{aligned} \tag{3.26}$$

If a task is repetitive (e.g., dumbbell curls), it is reasonable to focus on reducing the joint torque during a single period to optimize the entire amount of the torque. In such a case, T_{end} is defined as a period of repetitive motion.

The energy cost of the AP2A is mainly due to the use of compressed air from a supply pressure source. Increments of the mass of the air for e_1 and e_2 are expressed as:

$$\begin{aligned} \tilde{m}_a(z_{2j-1}, t_j) &:= (z_{2j-1} - P_{atm}) V_a(t_j) / RT \\ \tilde{m}_b(z_{2j}, t_j) &:= (z_{2j} - P_{atm}) V_b(t_j) / RT \end{aligned}$$

From the above, the cost function within a period is defined as follows:

$$\begin{aligned} J_{ap}(\xi, \mathbf{z}) &:= \sum_{j=1}^{N-1} L_2(\mathbf{x}(t_j^+ \mid \xi, \mathbf{z}), \mathbf{z}) \\ &= \sum_{j=1}^{N-1} (\tilde{m}_a + \tilde{m}_b) \end{aligned} \tag{3.27}$$

Note that energy to activate solenoid valves is neglected in this study. The total energy cost can be expressed with weight factors ω_1 and ω_2 such that:

$$J(\xi, \mathbf{z}) := \omega_1 J_{ext} + \omega_2 J_{ap} \tag{3.28}$$

From the above, the problem is summarized as follows:

$$\min_{\xi, \mathbf{z}} \quad J(\xi, \mathbf{z}) \tag{3.29a}$$

$$\text{s.t.} \begin{cases} \mathbf{x}(0) - \mathbf{x}_0 = 0, & (3.29b) \\ \dot{\mathbf{x}} - f = 0 & (3.29c) \\ g(\mathbf{x}, \xi, \mathbf{z}) = 0 & (3.29d) \\ h(\mathbf{x}, \xi, \mathbf{z}) \geq 0 & (3.29e) \end{cases}$$

The equations correspond as follows; Cost: (3.29a) → (3.28), Initial value: (3.29b) → (3.13), ODE model: (3.29c) → (3.11), (3.12), and constraints: (3.29d) → (3.23), (3.24) and (3.29e) → (3.14), (3.19), (3.22), respectively.

Gradient Formula for the Problem

A constrained optimal control problem is formulated, and the termination time T_{end} of the problem is specified while the terminal state is not fixed. Teo et al. have investigated to solve optimal control problems using a direct sequential method, which is called as Control Parameterization Method [119, 120]. Liu et al. utilized the method and investigated a solution to a class of optimal control problems with state jumps [118]. The formulated problem in (3.29) is solved based on these works. Note that the proof of the solution is neglected.

First, a time-scaling transformation [120] is applied to the problem as it requires to optimize the switching timing ξ in (3.20). The transformation works by mapping the variable switching timing t_j to fixed points j in a new time horizon expressed with a new variable $s \in [0,\ N+1]$ as follows:

$$\begin{aligned} \frac{dt(s)}{ds} &:= \sum_{k=1}^{N+1} \eta_k \chi_{[k-1,k)}(s) \\ \eta_k &:= t_k - t_{k-1} \\ \chi_{[k-1,k)}(s) &:= \begin{cases} 1 & \text{if } s \in [k-1, k) \\ 0 & \text{else} \end{cases} \end{aligned}$$

where $k = 1, ..., N+1$, and $s(0) = 0$, $s(N+1) = T_{end}$. The transformation can be expressed equivalently as the following equation:

$$t(s) = \sum_{k'=0}^{\lfloor s \rfloor} \eta_{k'} + \eta_{\lfloor s \rfloor + 1}(s - \lfloor s \rfloor)$$

where $k' = 0, ..., N$, and $\eta_0 = 0$. Fig. 3.4 shows an example of the transformation.

The decision vector ξ and corresponding constraints in (3.19), (3.20) are then replaced with a new decision vector $\eta \in \mathbb{R}^{N+1}$ as:

$$\eta := [\eta_1, ..., \eta_{N+1}]^T, \ \ \eta_k \geq 0 \tag{3.30}$$

Accordingly, a new state vector $\mathbf{y} \in \mathbb{R}^5$ is introduced as follows:

$$\begin{aligned} \mathbf{y}(s) &:= \mathbf{x}(t(s)) \\ \mathbf{y}(0) &= \mathbf{x}(0) \end{aligned}$$

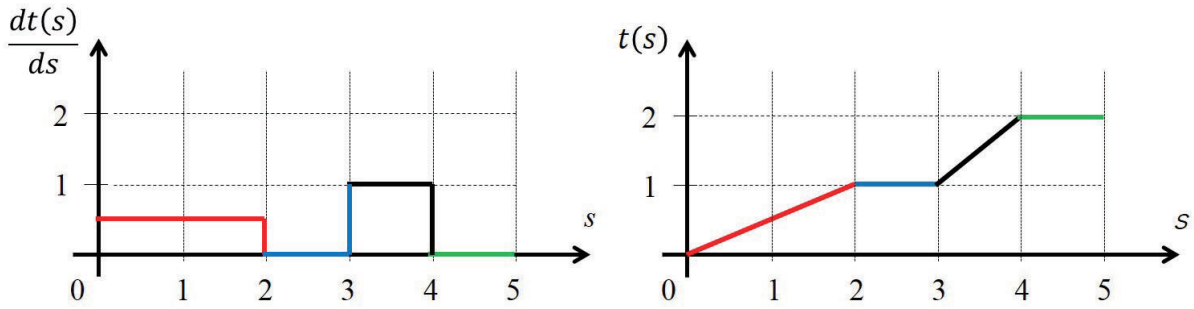

Figure 3.4: Graphical representation of the time-scaling transformation.

Introducing the vector $\mathbf{y}$, the dynamics in (3.11), (3.12) can be expressed for $s \in [k-1,k)$ as follows:

$$\dot{\mathbf{y}} = \begin{cases} \eta_k f(q_1,\mathbf{y}) = \hat{f}_1 \ (k = 1, N+1) \\ \eta_k f(q_2,\mathbf{y}) = \hat{f}_2 \ (else) \end{cases}$$

The original problem is then reformulated to search feasible vectors η and $\mathbf{z}$, which minimize the following cost functional derived from (3.26), (3.27), and (3.28):

$$\begin{aligned} J_{ext}(\eta,\mathbf{z}) &= \sum_{k=1}^{N+1} \int_{k-1}^{k} L_1(\mathbf{y}(s \mid \eta,\mathbf{z}))\eta_k ds \\ J_{ap}(\eta,\mathbf{z}) &= \sum_{j=1}^{N-1} L_2(\mathbf{y}(j^+ \mid \eta,\mathbf{z}),\mathbf{z}) \\ J(\eta,\mathbf{z}) &= \omega_1 J_{ext}(\eta,\mathbf{z}) + \omega_2 J_{ap}(\eta,\mathbf{z}) \end{aligned}$$

Based on [118], the gradients of the cost functional $J_{ext}(\eta,\mathbf{z})$ with respect to η and $\mathbf{z}$ are expressed with the costate vector $\lambda \in \mathbb{R}^5$ of the system as follows:

$$\frac{\partial J_{ext}}{\partial \eta} = \sum_{k'=0}^{N} \left\{ \lambda^T(k'^+ \mid \eta,\mathbf{z}) \frac{\partial \mathbf{y}(k'^+ \mid \eta,\mathbf{z})}{\partial \eta} + \int_{k'}^{k'+1} \frac{\partial H(\mathbf{y}(s \mid \eta,\mathbf{z}),\lambda(s \mid \eta,\mathbf{z}),\eta)}{\partial \eta} ds \right\} \tag{3.31}$$

$$\frac{\partial J_{ext}}{\partial \mathbf{z}} = \sum_{k'=0}^{N} \lambda^T(k'^+ \mid \eta,\mathbf{z}) \frac{\partial \mathbf{y}(k'^+ \mid \eta,\mathbf{z})}{\partial \mathbf{z}} \tag{3.32}$$

where $k' = 0,\ldots,N$, and H is Hamiltonian defined for $s \in [k',k'+1)$ as:

$$H := \begin{cases} \eta_{k'+1} L_1(\mathbf{y}) + \lambda^T \hat{f}_1 \ (k' = 0, N) \\ \eta_{k'+1} L_1(\mathbf{y}) + \lambda^T \hat{f}_2 \ (else) \end{cases} \tag{3.33}$$

The gradients of the cost functional $J_{ap}(\eta, \mathbf{z})$ with respect to η and $\mathbf{z}$ are acquired by computing derivatives of the cost functional and are given as follows:

$$\frac{\partial J_{ap}}{\partial \eta} = \sum_{j=1}^{N-1} \frac{\partial L_2}{\partial \mathbf{y}} \frac{\partial \mathbf{y}(j^+)}{\partial \eta} \tag{3.34}$$

$$\frac{\partial J_{ap}}{\partial \mathbf{z}} = \sum_{j=1}^{N-1} \left(\frac{\partial L_2}{\partial \mathbf{y}} \frac{\partial \mathbf{y}(j^+)}{\partial \mathbf{z}} + \frac{\partial L_2}{\partial \mathbf{z}} \right) \tag{3.35}$$

To compute the gradients (3.31) to (3.35), it is required to compute three terms, the costate vector λ, and partial derivatives of right and left limit of $\mathbf{y}$ (i.e., $\mathbf{y}(s^+)$ and $\mathbf{y}(s^-)$, respectively) with respect to the decision vectors. The costate vector $\lambda(s)$ in $s \in [k', k'+1)$ is derived as a solution of the backward initial-value problem stated as follows:

$$\dot{\lambda}(s) = -\frac{\partial H}{\partial \mathbf{y}}, \quad \lambda((k'+1)^-) = \mathbf{0}_{5\times 1} \tag{3.36}$$

where $\mathbf{0}_{m\times n}$ denotes a m-by-n matrix of zeros. The right limit of partial derivatives $\mathbf{y}(k'^+)$ with respect to the decision vectors is computed based on (3.23) as:

$$\frac{\partial \mathbf{y}(k'^+ \mid \eta, \mathbf{z})}{\partial \eta} = \frac{\partial \phi_{k'}(\mathbf{y}(k'^-), \mathbf{z})}{\partial \eta} = \frac{\partial \phi_{k'}}{\partial \mathbf{y}} \frac{\partial \mathbf{y}(k'^-)}{\partial \eta} \tag{3.37}$$

$$\frac{\partial \mathbf{y}(k'^+ \mid \eta, \mathbf{z})}{\partial \mathbf{z}} = \frac{\partial \phi_{k'}}{\partial \mathbf{y}} \frac{\partial \mathbf{y}(k'^-)}{\partial \mathbf{z}} + \frac{\partial \phi_{k'}}{\partial \mathbf{z}} \tag{3.38}$$

$$\frac{\partial \mathbf{y}(k'^+ \mid \eta, \mathbf{z})}{\partial \eta} = \frac{\partial \phi_{k'}(\mathbf{y}(k'^-), \mathbf{z})}{\partial \eta} = \frac{\partial \phi_{k'}}{\partial \mathbf{y}} \frac{\partial \mathbf{y}(k'^-)}{\partial \eta} \tag{3.39}$$

$$\frac{\partial \mathbf{y}(k'^+ \mid \eta, \mathbf{z})}{\partial \mathbf{z}} = \frac{\partial \phi_{k'}}{\partial \mathbf{y}} \frac{\partial \mathbf{y}(k'^-)}{\partial \mathbf{z}} + \frac{\partial \phi_{k'}}{\partial \mathbf{z}} \tag{3.40}$$

Since the initial conditions are independent on the decision variables, the derivatives at $k' = 0$ are set as follows:

$$\frac{\partial \mathbf{y}(0^+ \mid \eta, \mathbf{z})}{\partial \eta} = \frac{\partial \mathbf{y}(0^- \mid \eta, \mathbf{z})}{\partial \eta} = \mathbf{0}_{5\times(N+1)} \tag{3.41}$$

$$\frac{\partial \mathbf{y}(0^+ \mid \eta, \mathbf{z})}{\partial \mathbf{z}} = \frac{\partial \mathbf{y}(0^- \mid \eta, \mathbf{z})}{\partial \mathbf{z}} = \mathbf{0}_{5\times 2(N-1)} \tag{3.42}$$

The left limit of partial derivatives $\mathbf{y}(k'^-)$ with respect to the decision vectors is expressed as:

$$\frac{\partial \mathbf{y}(k'^- \mid \eta, \mathbf{z})}{\partial \eta} = V(k'), \; \frac{\partial \mathbf{y}(k'^- \mid \eta, \mathbf{z})}{\partial \mathbf{z}} = U(k') \tag{3.43}$$

where $V \in \mathbb{R}^{5\times(N+1)}$ and $U \in \mathbb{R}^{5\times 2(N-1)}$ are computed as solutions to the following matrix initial-value problem in $s \in [k'-1, k')$ such that:

$$\dot{V}(s) = \frac{\partial \hat{f}_2(\mathbf{y},\eta)}{\partial \mathbf{y}} V(s) + \frac{\partial \hat{f}_2(\mathbf{y},\eta)}{\partial \eta} \tag{3.44}$$

$$V(k'-1) = \frac{\partial \mathbf{y}((k'-1)^+ \mid \eta, \mathbf{z})}{\partial \eta} \tag{3.45}$$

$$\dot{U}(s) = \frac{\partial \hat{f}_2(\mathbf{y},\eta)}{\partial \mathbf{y}} U(s) \tag{3.46}$$

$$U(k'-1) = \frac{\partial \mathbf{y}((k'-1)^+ \mid \eta, \mathbf{z})}{\partial \mathbf{z}} \tag{3.47}$$

3.3 Simulation Study

Implementation

The problem was solved by `fmincon` solver (internal point method) based on the computed gradients (3.31) to (3.35) in `MATLAB 2016b` installed in a laptop (Intel Core i-5, RAM 8GB). The pseudo-code shows an abstract of an algorithm used in the simulation to compute the gradients (3.31) to (3.35). The costate trajectory (3.36) was computed backward in time after calculating a partial derivative of (3.33) with respect to $\mathbf{y}$. The partial derivatives of right and left limit of $\mathbf{y}$ with respect to the decision vectors were computed alternately and iteratively with respect to k'. `ODE45` solver was utilized to compute the costate trajectory and the matrix initial-value problem, and the number of steps was 1000. The trapezoidal rule was applied for the integral computation in (3.31) with the same step size.

Algorithm 2 Gradient Computation

```
procedure
    k' ← 0.
    Get λ(s) with (3.36).
    Get elements at k' in (3.31) to (3.35) with (3.41) and (3.42).
    k' ← 1.
    while k' < N + 1 do
        Get λ(s) with (3.36).
        Get ∂y(k'^− | η, z)/∂(η, z) by (3.43) to (3.47).
        Get ∂y(k'^+ | η, z)/∂(η, z) by (3.37) and (3.38).
        Get elements at k' in (3.31) to (3.35).
        k' ← k' + 1.
```

As shown in (3.21) and (3.30), the total number of decision variables is $3N-1$ using the number of switching N. It is obvious that the number of decision variables is proportional to the number of switching, and the computation cost increases as the number of switching increases. A simulation study in this chapter limits the switching time N to be 4.

Conditions of Simulation

Fig. 3.5 shows schematics of experimental environments used in the simulation study. A pendulum in Fig. 3.5 imitates the elbow joint movements of a human. Comparing with Fig. 3.1, an electrical motor and a load were introduced to actuate the system as an external torque and to change a mass of the sub-assembly. The external joint torque τ_{ext} (τ_m in Fig. 3.5) needs to be determined to conduct the simulation as discussed in section 3.2. In this simulation study, an objective of the system was determined to track a given reference θ_d while holding the load, which imitates the simplest motion of robot arms in factories. A simple, proportional position controller was designed as an initial investigation to simplify the computation of gradients as discussed in section 3.2. The desired angle θ_d was assumed to be a sinusoidal wave. The joint torque τ_m provided by the current controlled motor was thus determined as follows:

$$\begin{aligned} \tau_m(i) &= NK_t i && (3.48)\\ i &= -K_p(\theta-\theta_d) - \frac{\tau_{g_{FF}}(\theta_d)}{NK_t} && (3.49)\\ \tau_{g_{FF}} &:= -(m_{arm}+m_{load})gl_f sin(\theta_d) && (3.50)\\ \theta_d(t) &:= \theta_0(1+cos(2\pi ft))/2 \end{aligned}$$

where N is a reduction gear ratio, K_t is a torque constant, i is a current input, K_p is the proportional gain of the controller, m_{arm}, m_{load} are the mass of the arm sub-assembly and the load, and f is the frequency of the motion. A block diagram of this setup is shown in Fig. 3.6 from the viewpoint of

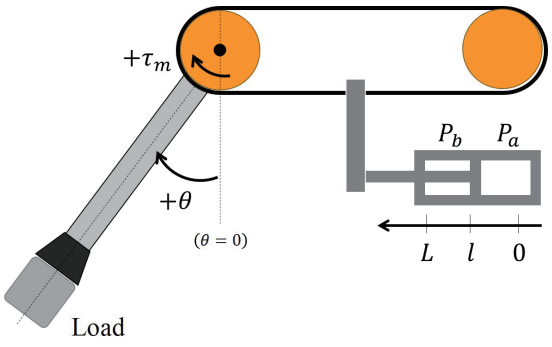

Figure 3.5: Experimental environments for the simulation study.

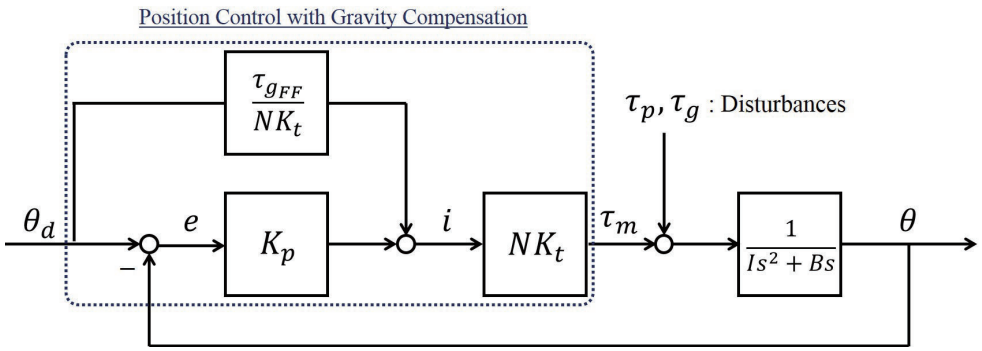

Figure 3.6: Block diagram of a position-controlled motor implemented in the pendulum.

the position-controlled motor. With this control, the dynamics (3.6) can be rewritten as follows:

$$(I_{all} + I_{load})\ddot{\theta} + B\dot{\theta} = \tau_p + \tau_g + \tau_m \tag{3.51}$$
$$\tau_g = -(m_{arm} + m_{load})gl_f sin(\theta) \tag{3.52}$$

where I_{load} is an inertia of the load, and I_{all} includes the inertia of the arm sub-assembly, a rotor of the motor, and a reduction gear.

Five simulations were conducted with four different weights as follows:

$$[\omega_1, \omega_2] = [10^{-3}, 10^6], [2.5 \cdot 10^{-1}, 10^6], [5.0 \cdot 10^{-1}, 10^6], [10^2, 10^6] \tag{3.53}$$

These weights were determined, aligning the number of digits of costs J_{ext} and J_{ap}. The fifth condition was the control condition in which a discrete state stayed in q_1. In all simulations, the decision vectors were initially set as:

$$\eta = 2 \cdot \mathbf{1}_{5\times 1} \tag{3.54}$$
$$\mathbf{z} = 3P_{atm} \cdot \mathbf{1}_{6\times 1} \tag{3.55}$$

The parameters of the optimization problem (3.29) applied in this study are shown in Table 3.1.

Simulation Results

Computational time solving the optimization problem under the four conditions were 720, 600, 230, 630 seconds, respectively. Table 3.2 shows the computed energy costs J_{ext} and J_{ap} under the optimal conditions, which are defined in (3.26) and (3.27), respectively. Note that the control condition was computed by including additional constraints ($\eta_{NA}(1) = 10.0$ and $\eta_{NA}(2)$, $\eta_{NA}(3)$, $\eta_{NA}(4)$, $\eta_{NA}(5) = 0.0$), assuming that the AP2A never switched to q_2 (i.e., *passive* mode). The optimal solutions $\eta^*, \mathbf{z}^*$ to each condition were:

$$\eta_1^* = [1.0, 3.0, 3.8, 1.5, 0.7]^T \tag{3.56}$$
$$\mathbf{z}_1^* = [1.0, 1.0, 1.0, 1.0, 1.0, 1.0]^T P_{atm} \tag{3.57}$$

Table 3.1: Parameters of the numerical model in Fig 3.5

Params (unit)	**Value**	**Params (unit)**	**Value**
l_0 (m)	$3.60 \cdot 10^{-2}$	r (m)	$3.00 \cdot 10^{-2}$
A_a (m^2)	$2.85 \cdot 10^{-4}$	A_b (m^2)	$2.53 \cdot 10^{-4}$
A_r (m^2)	$3.22 \cdot 10^{-5}$	L (m)	$7.56 \cdot 10^{-2}$
R (J/(kgK))	$2.87 \cdot 10^{2}$	T (K)	$2.93 \cdot 10^{2}$
P_{atm} (Pa)	$1.01 \cdot 10^{5}$	P_{supply} (Pa)	$7.09 \cdot 10^{5}$
N	$1.86 \cdot 10^{2}$	K_t (Nm/A)	$1.14 \cdot 10^{-1}$
K_p (Nm/rad)	$1.60 \cdot 10^{1}$	l_f (m)	$3.00 \cdot 10^{-1}$
θ_0 (rad)	1.05	f (Hz)	$1.00 \cdot 10^{-1}$
I_{all} (kgm^2)	4.23	I_{load} (kgm^2)	$2.69 \cdot 10^{-1}$
B (kgm/s)	$2.43 \cdot 10^{1}$	m_{arm} (kg)	$3.24 \cdot 10^{-1}$
m_{load} (kg)	2.97	g (m/s^2)	9.81

Table 3.2: Computed costs in the simulation study

	No Assist	Weight Conditions $[\omega_1, \omega_2]$			
		$[10^{-3}, 10^{6}]$	$[2.5 \cdot 10^{-1}, 10^{6}]$	$[5.0 \cdot 10^{-1}, 10^{6}]$	$[10^{2}, 10^{6}]$
Motor J_{ext} $(10^2(\text{Nm})^2 s)$	2.64	2.63	2.15	1.71	1.25
Exo J_{ap} (10^{-4}kg)	N/A	0.0	0.0	0.23	2.95

$$\eta_2^* = [0.0, 10.0, 0.0, 0.0, 0.0]^T \tag{3.58}$$
$$\mathbf{z}_2^* = [1.0, 1.0, 1.0, 1.0, 1.0, 1.0]^T P_{atm} \tag{3.59}$$

$$\eta_3^* = [0.0, 10.0, 1.0, 0.0, 0.0]^T \tag{3.60}$$
$$\mathbf{z}_3^* = [2.0, 1.0, 1.0, 1.0, 1.0, 1.0]^T P_{atm} \tag{3.61}$$

$$\eta_4^* = [0.0, 2.8, 7.1, 0.0, 0.1]^T \tag{3.62}$$
$$\mathbf{z}_4^* = [6.5, 1.7, 5.1, 1.0, 5.0, 2.3]^T P_{atm} \tag{3.63}$$

Units of η were reported in seconds. Fig. 3.7 to Fig. 3.10 show the assistive torque τ_p produced by the AP2A under the optimal condition (3.57), (3.59), (3.61), and (3.63), respectively. The left and right figures indicate the torque changes in scaled-time s and in time t, respectively. Dotted colored lines suggest the timing at which transitions occurred, and the lines in the left and right figures correspond to each other. Notice that, as shown in Fig. 3.2, the AP2A is modeled as a device that starts and ends its assistance in q_1 (i.e., *no-assist* mode). The assistive torque is, accordingly, equal to zero in $s \in [0, 1)$ and $s \in [4, 5]$ in all the figures.

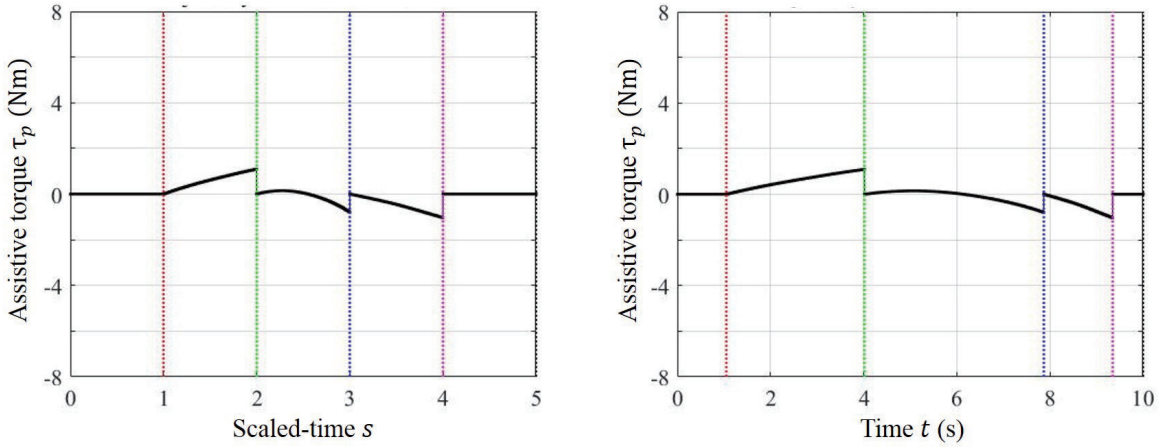

(a) In scaled-time s. (b) In time scale t.

Figure 3.7: Assistive torque simulated under the optimal condition η_1^* and $\mathbf{z}_1^*$.

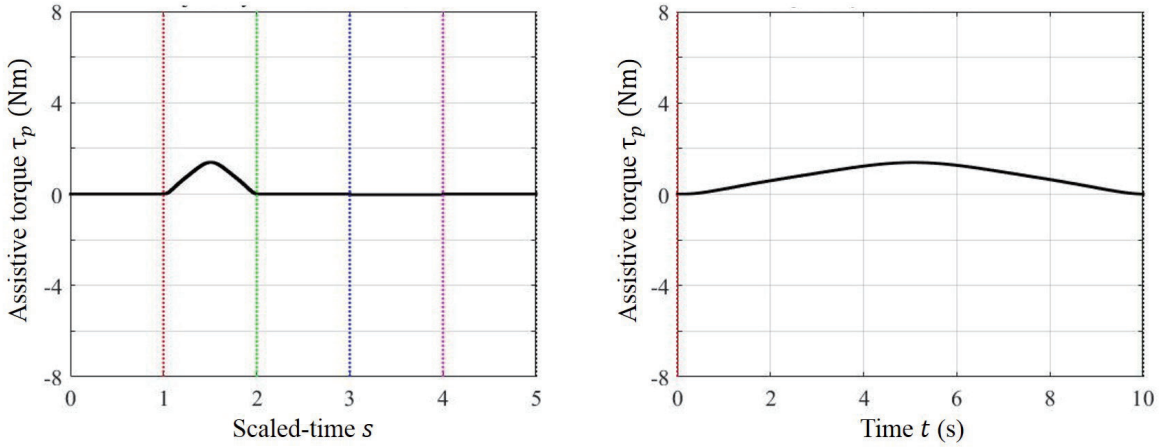

(a) In scaled-time s. (b) In time scale t.

Figure 3.8: Assistive torque simulated under the optimal condition η_2^* and $\mathbf{z}_2^*$.

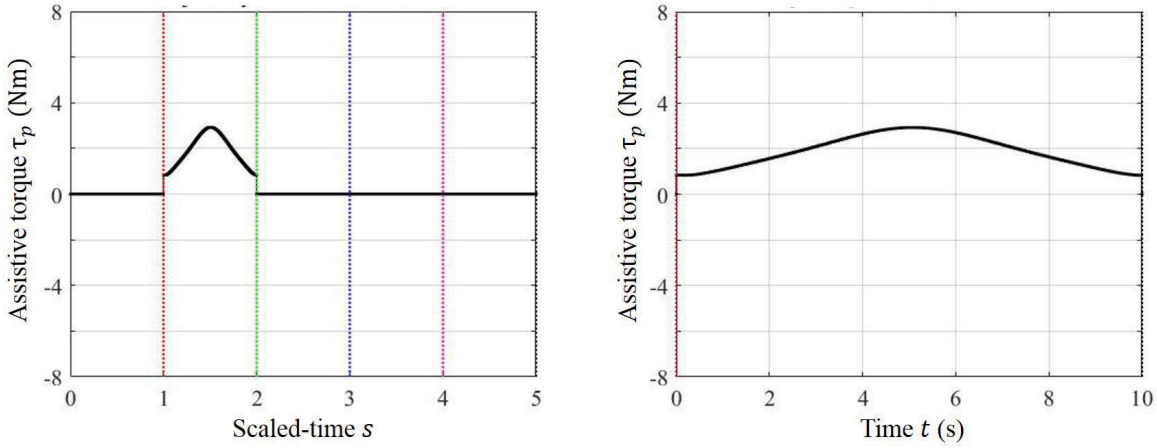

(a) In scaled-time s. (b) In time scale t.

Figure 3.9: Assistive torque simulated under the optimal condition η_3^* and $\mathbf{z}_3^*$.

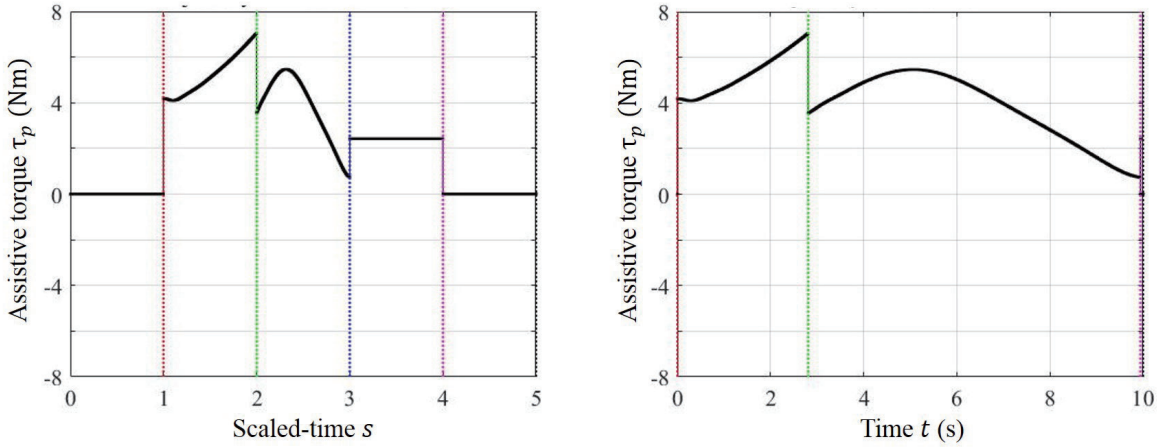

(a) In scaled-time s. (b) In time scale t.

Figure 3.10: Assistive torque simulated under the optimal condition η_4^* and $\mathbf{z}_4^*$.

3.4 Discussion

The proposed control framework optimizes two variables, η and $\mathbf{z}$, based on the weight factor ω_1 and ω_2. Table 3.2 indicates how the weight conditions effect to the cost of J_{ap} as well as J_{ext}. For the long-term usage of the AP2A, it is essential to reduce the consumption of the supply air. By weighting the energy cost J_{ap} with ω_2, the proposed framework provides the optimal result which saves the supply air. Accordingly, the cost J_{ap} was zero under the first weight condition. The vector $\mathbf{z}_1^*$ in (3.57) indicates the AP2A did not use *any* supply air but replaced the air in the chambers with the atmosphere during switching. This replacement is also indicated in Fig. 3.7a, which indicates changes of the torque in scaled time-series s. In the figure, the assistive torque was modified to be zero at the beginning of each switching timings due to the replacement. The other variable ${\eta_1}^*$ was not modified effectively from the initial condition, as indicated in (3.56). Fig. 3.7b suggests that the assistive torque was modified several times by replacing the air in chambers. The cost J_{ext} was equal to the cost under the control condition (i.e., *no-assist* condition). It means that the torque provided by the AP2A under the first weight condition did not assist the pendulum's movement.

Function as Passive Devices to Save Energy

The switching timings η were modified by taking the cost of the pendulum J_{ext} into consideration. Under the second weight condition (i.e., $[\omega_1, \omega_2] = [0.25 \cdot 10^{-1}, 10^6]$), the switching timings η_2 were modified to (3.58) and Fig. 3.8b. Table 3.2 shows that the cost J_{ext} decreased by 18% compared with that of the first condition while maintaining the cost J_{ap} to be zero. The air in the chambers was replaced with the atmosphere (i.e., not with the supply air) during switching under the second condition, as suggested in (3.59). Under the first condition, chamber pressures could not provide the pendulum with the assistive torque effectively, being modified at each switching timing. By optimizing the switching timings η under the second condition, the control framework had the AP2A stay in the *passive* mode during $t \in [0, T_{end})$ to provide the user with assistance effectively.

The function of the AP2A under the second condition was equivalent to a mechanical, nonlinear spring. The proposed control framework had the capability of modifying the chamber pressures (i.e., τ_p) three times in $s \in [1,4)$. Since the number of switching times was preset ($N = 4$), e_1 and e_3 were enabled once, and e_2 was enabled twice. The AP2A was thus able to take three different *passive* modes in which the actuator worked as a mechanical spring with different stiffness and equilibrium. Under the second condition, the controller discarded these two chances and switched *only once* at the beginning of the task to save the energy by working as a mechanical spring, as shown in Fig. 3.8b. Thanks to this decision, the AP2A could store initial potential energy of the load to elastic energy by compressing the air in the chamber (i.e., increasing P_a). Accordingly, the assistive torque shows the positive value in $s \in [2,3)$ to provide the pendulum with assistance.

Function as Active/Passive Device to Enhance Assistance

The proposed framework can also be applied to reduce the energy consumption of the external power source at the expense of the supply air. The framework enables the AP2A to provide the assistive torque as much as possible by further weighting the cost J_{ext}. The larger ω_1 becomes, the larger the proportion of the cost J_{ext} to the total cost J will be. The first column of Table 3.2 suggests that the two costs are different by six orders of magnitude due to differences of units (i.e., $(\mathrm{Nm})^2$s and kg). The supply air starts to be used when the two costs are in the same order under the third condition. The chamber pressures $\mathbf{z}_3^*(3)$ in (3.61) indicates the AP2A used the supply air to provide more assistance, however, the switching timings ${\eta_3}^*$ were not modified from those under the second condition ${\eta_2}^*$ as indicated in (3.58) and (3.60). Fig. 3.9a also indicates these numerical results, as the assistive torque τ_p was modified to be about 1 Nm at $s = 1$. Table 3.2 suggests that the cost J_{ext} decreased along with a slight increase in the cost J_{ap} under the third condition.

The fourth condition was regarded as the case which neglected the cost of the AP2A, J_{ap}. In contrast to Fig. 3.9b, the control framework started to utilize the chances to switch *passive* modes by optimizing η_4 as well as $\mathbf{z}_4$. The pressures in each chamber (i.e., $\mathbf{z}_4$) were tuned by switching the modes to optimize the assistive torque τ_p. Accordingly, the magnitude of the assistive torque τ_p was increased by switching to the next mode if the assistance was not sufficient, which can be confirmed in the transition at $s = 1$ (i.e., around $t = 0.0$ second in Fig. 3.10b). Besides, excessive assistance could be reduced by switching to the next passive mode at $s = 2$ (i.e., around $t = 3.0$ seconds in Fig. 3.10b). It can be confirmed that the cost J_{ext} under the fourth condition becomes the minimum among other conditions while J_{ap} shows the largest value among others.

From the above, the proposed framework could balance the competing goals for reducing the energy consumption and delivering suitable assistance, by optimizing the chamber pressures $\mathbf{z}$ during transitions and the switching timings η.

Limitations

One of the limitations of the numerical method applied to the optimal control problem in (3.29) was found to be slow. In this study, the indirect method was utilized to solve the optimization problem. This method may not be suitable if the plant is modeled as a highly nonlinear system. Recent studies suggest direct methods may solve the problem faster and more robust, which solve it as a nonlinear optimization problem and do not compute the ordinary differential equations such as the costate equations (3.36). These faster and more robust methods need to be investigated further with the existing optimization method.

3.5 Summary

A control framework was introduced as a high-level controller of an assistive system with the AP2A engaging in a repetitive, load manipulation task. A mathematical model of the system was described with hybrid systems, which included *no-assist* and *passive* (i.e., *assist*) modes as well as

the model in Fig. 1.10. This chapter focused on the formulation of optimal control parameterization problem to search for the optimal pressures $\mathbf{z}$ of the AP2A and switching timings η to minimize the energy consumption of the system. These pressures and switching timings can be provided as a reference to the low-level controller in chapter 2.

The simulation study was conducted with a numerical model of a pendulum to evaluate the performance of the control law obtained as the solution of the optimal control problem. A cost function of the problem included energy consumed by the AP2A (i.e., amount of the supply air) and the pendulum (i.e., a joint torque produced by a motor) with weight factors. By weighting the cost of the AP2A J_{ap}, the proposed framework tuned the switching timings η effectively to assist the pendulum passively without any supply air consumption while reducing the joint torque by 18%. On the other hand, by weighting the cost of the pendulum J_{ext}, the proposed framework enabled the AP2A to reduce the motor torque actively by more than half at the expense of the supply air. From these results, the proposed framework has the potential to balance the competing goals of minimizing the energy consumption of the devices while maximizing the user assistance under the specific condition.

Chapter 4

Verification Test of Active/Passive Switching Control Framework

4.1 Chapter Overview

This chapter describes experiments with a pendulum emulating human elbow joint to validate performance of an Active/Passive Pneumatic Actuator (AP2A) confirmed in chapter 3. In particular, this experimental study focuses on the validation of passive assistance (i.e., assistance staying in *passive* mode). A simplified model expressed with hybrid systems is introduced to solve the optimal control problem discussed in section 3.2 efficiently. Section 4.3 describes a simulation study with the introduced model to search for reference pressures. Section 4.4 explains experiments with the pendulum to validate the effects of the passive assistance provided by the AP2A. Experimental results suggest that passive assistance could improve the energy efficiency of the pendulum as well as the AP2A.

4.2 System Identification of Pendulum

Fig. 4.1 and 4.2 show an overview of the experimental setup and its schematic diagram, respectively. It utilizes the same concept, as shown in Fig. 3.1 and 3.5. A geared motor was placed in the middle of the system, which controlled the arm movements by transmitting a torque τ_m with a belt. A pneumatic cylinder working as the AP2A was connected to a geared motor by another transmission belt. A pneumatic force produced by the AP2A in *passive* mode (i.e., q_2 in Fig. 3.2) was expected to reduce the motor torque to save energy of a power supply. In order to modify dynamics around a rotational joint, a load was attached to an arm of the pendulum. Connectors of the belts (orange circles in Fig. 4.2) were identical so that the joint angles/torques between the connectors are assumed to be identical. Note that a direction of rotation was reversed from Fig. 3.5.

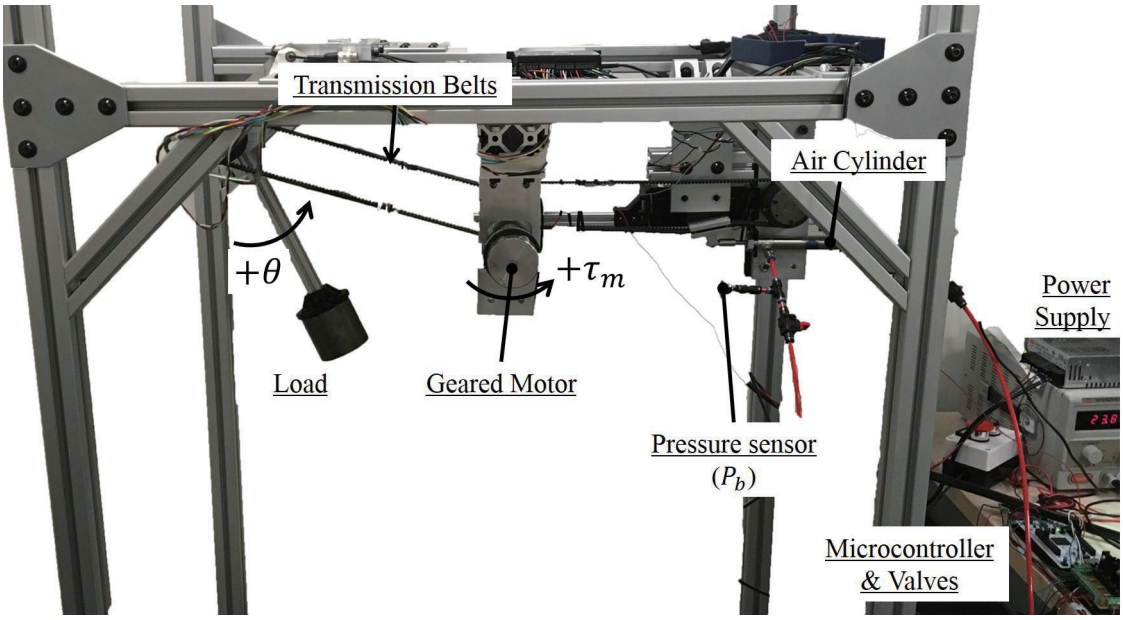

Figure 4.1: Experimental setups.

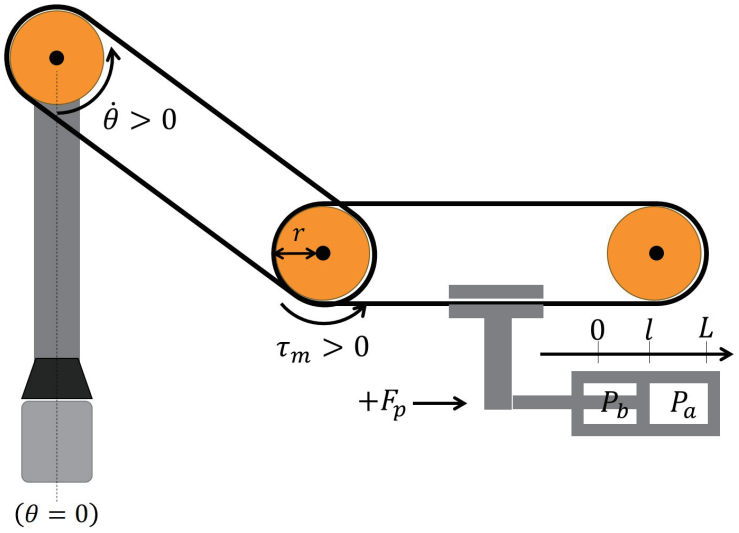

Figure 4.2: Schematics of the experimental setups in Fig. 4.1.

Linearized System Model for Identification

The system model described in section 3.2 is applicable to the pendulum. However, model parameters need to be identified to conduct a simulation and to design controllers for experiments. Detaching the pneumatic actuator and a load from the system, a frequency response analysis was conducted to identify the damping coefficient B in (3.6). The dynamics identified in the experiment is expressed as follows:

$$I\ddot{\theta} + B\dot{\theta} = NK_t i + \tau_g \tag{4.1}$$

$$I := N^2 I_{rot} + I_g + I_{arm} \tag{4.2}$$

where θ is a joint angle of the pendulum, N is a reduction gear ratio, I_{rot}, I_g, I_{arm} are the inertia of a rotor, a gear, an arm sub-assembly, and K_t is a torque constant. Without a load, the gravitational torque τ_g was assumed to be small and neglected in this analysis. The system is thus rewritten as the linear, second-order ordinary differential equation.

Experimental Setups

Experimental setups for the system identification are shown in Fig. 4.1. A joint angle θ was measured by an encoder (US Digital, MA3-A10). A DC geared motor (Maxon, EC60flat with GP52C) with a dedicated motor driver (Maxon, Escon50/5) was introduced to produce a torque τ_m by current control. Simulink Real-Time was introduced to control the motor of the arm. The current i used in the experiments were also logged by Simulink Real-Time. The system ran on the laptop with `MATLAB 2016b`.

Fig. 4.1 also shows setups for the AP2A used for further experiments described in section 4.4. A 0.75 inch bore, 3 inch stroke cylinder (Bimba, SR-043-D) was implemented with a potentiometer measuring a rod position l. The valve array consisted of two 5-port solenoid valves (SMC, SY7340-5GZ). An air compressor with a regulator provided the cylinder with compressed air. Three pressure sensors (Omega, PX40-100G5V) were utilized to measure the supply pressure and pressures in the chambers (i.e., P_{supply}, P_a, and P_b). A microcontroller (Nucleo F746ZG, STM) sampled pressure sensors and the potentiometer and logged the data on a laptop via serial communication. The start timings of the microcontroller and Simulink Real-Time were synchronized.

Experimental Conditions for System Identification

Nominal parameters in (4.1) and (4.2) are shown in Table 4.1. A frequency response analysis was conducted to identify the parameters in (4.1). The motor driver was operated in a current control mode, and sinusoidal signals with multiple frequencies were input to the driver as a reference of the current i in (4.1). Due to the mechanical constraints of the experimental setups, the frequencies f were determined as follows:

$$f = 0.05,\ 0.08,\ 0.1,\ 0.2,\ 0.4,\ 0.5,\ 0.8,\ 1.0,\ 1.2,\ 1.5$$

Table 4.1: Nominal parameters of a geared motor in Fig. 4.1

Params (unit)	Value	Params (unit)	Value
I_{rot} (kgm^2)	$1.21 \cdot 10^{-4}$	I_g (kgm^2)	$1.73 \cdot 10^{-6}$
I_{arm} (kgm^2)	$3.89 \cdot 10^{-2}$	N	$1.86 \cdot 10^{2}$
K_t (Nm/A)	$1.14 \cdot 10^{-1}$	–	–

where the unit of f was hertz (Hz). 30 cycles of steady-state responses were collected via Simulink Real-Time at 2000 Hz for each frequency. The magnitude and phase delay of the measurement data were computed based on the reference inputs. Those parameters were estimated by `lsqnonlin` solver, and `frd` function was utilized to draw a Bode plot. Those functions were used in `MATLAB 2016b`.

Experimental Results & Discussion

Fig. 4.3 shows the Bode diagram according to the experimental results of the system identification. Blue lines with crosses indicate the experimental results. Red lines with dots were obtained by fitting parameters of the linearized second-order model in (4.1) to the results. The model $G(s)$ was estimated as follows:

$$G(s) := \frac{\Theta(s)}{I(s)} = \frac{4.8}{s^2 + 5.75s} \tag{4.3}$$

According to Table 4.1, the nominal inertia I and the numerator of the model $G(s)$ (i.e., NK_t) are computed as follows:

$$I = 4.23,\ NK_t = 21.2 \tag{4.4}$$

With this nominal inertia I, the empirical model $G(s)$ is expressed as:

$$G(s) = \frac{NK_t}{Is^2 + Bs} = \frac{20.3}{4.23s^2 + 24.3s} \tag{4.5}$$

There is only a slight difference (ca. 5%) between nominal and empirical values of the numerator (i.e., NK_t) by comparing (4.4) and (4.5). Based on this observation, the damping factor B in the model is determined as 24.3 kgm/s and the value is utilized in the following simulation study and experiments.

4.3 Simulation Study

Modeling of a Pendulum with AP2A

A numerical model of the pendulum with the AP2A is shown in Fig. 4.4, modified from Fig. 3.2. Considering of passive assistance provided by the AP2A, the number of switching time N is set to be 2 in this study. The edge e_2 is thus neglected in Fig. 4.4 compared to Fig. 3.2. Since motions of

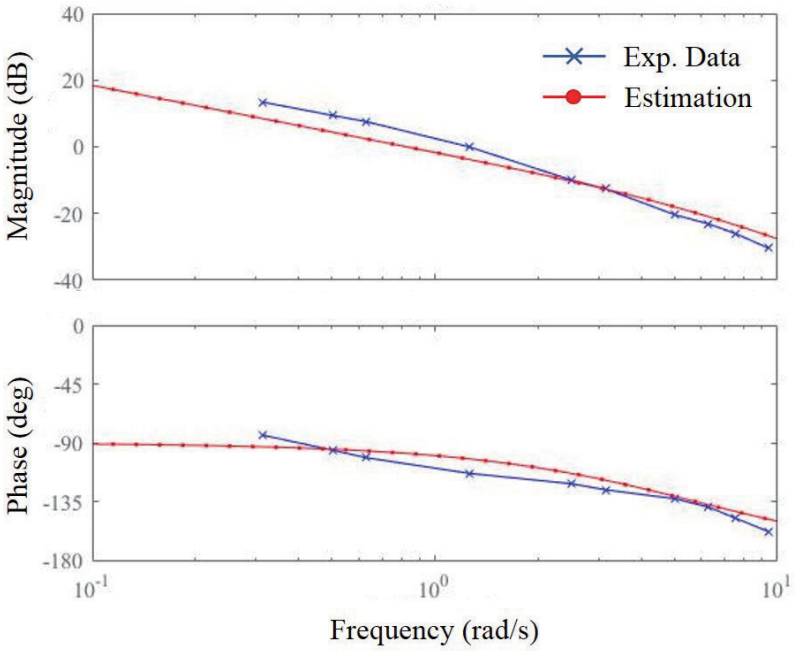

Figure 4.3: Bode plot obtained through the identification process.

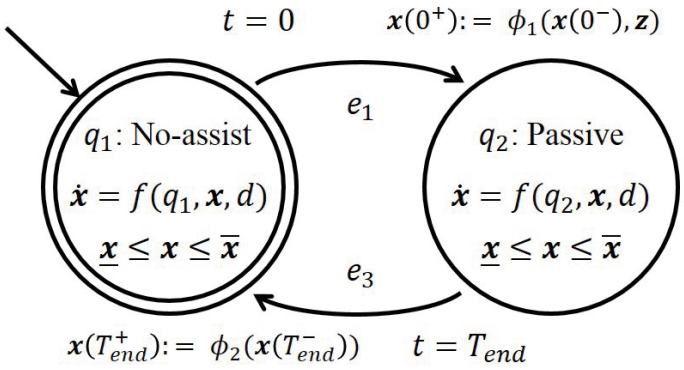

Figure 4.4: Simplified numerical model based on Fig. 3.2, focusing on passive assistance.

the pendulum can be controlled, the passive assistance is assumed to begin and end at $t = 0, T_{end}$ in this simulation study and the following experiments, respectively. A hybrid automation H of the model is expressed as follows; $Q : q_1, q_2$, $X : (4.6)$, $f : (4.13), (4.14)$, $Init : (4.7)$, $Dom : (4.15)$, $E : (4.16)$, $G : (4.17), (4.18)$, $Re : (4.20), (4.21)$.

Two discrete modes (i.e., the *no assist* and *passive* mode) were considered (i.e., q_1 and q_2) in the model. A continuous state vector $\mathbf{x} \in \mathbb{R}^5$ and the initial state $Init(q1, \mathbf{x}(0^-))$ are expressed as:

$$\begin{aligned} \mathbf{x}(t) &:= [\theta, \dot{\theta}, l, P_a, P_b]^T && (4.6) \\ \mathbf{x}(0^-) &:= [\theta_0, 0, l_0 + r\theta_0, P_{atm}, P_{atm}]^T && (4.7) \end{aligned}$$

where $\mathbf{x}(0^-)$ is the left limits of $\mathbf{x}$ at $t = 0$ (i.e., the state just before a transition), l is a rod position of a pneumatic actuator, P_i are pressures in the chamber i, θ_0 and l_0 are the initial angle and rod position, and P_{atm} is atmospheric pressure (=101 kPa), respectively. Each parameter is shown in 4.2, and note that a relation between the joint angle and the rod position is defined as follow:

$$l := l_0 + r\theta \tag{4.8}$$

where r is a radius of the connectors.

The dynamics around the rotation axis in Fig. 4.2 is expressed in the same way as (3.6):

$$\begin{aligned} I_{all}\ddot{\theta} + B\dot{\theta} &= \tau_p + \tau_g + N\tau_m && (4.9) \\ I_{all} &:= N^2 I_{rot} + I_g + I_{arm} + I_{load} && (4.10) \\ \tau_p &= (-P_a A_a + P_b A_b + P_{atm} A_r) r && (4.11) \\ \tau_g &= -mgl_f sin(\theta) && (4.12) \end{aligned}$$

where I_{load} is an inertia of the load, τ_p, and τ_g are the torque provided by the AP2A, and the gravitational torque. The assistive torque τ_p is defined in (3.2) and (3.3). However, the direction of the torque is reversed as shown in Fig. 4.2. The constant, damping coefficient B is the parameter identified in the previous section. Note that m $(:= m_{arm} + m_{load})$ is the mass of the arm-assembly m_{arm} and other external loads m_{load}. The dynamics f in discrete modes are thus written with (3.1), (3.9), (3.10), and (4.9) as follows:

$$\begin{aligned} \dot{\mathbf{x}} &= f(q_1, \mathbf{x}, d) \\ &= \begin{bmatrix} \dot{\theta} \\ (-B\dot{\theta} + \tau_p + \tau_g + N\tau_m)/I_{all} \\ r\dot{\theta} \\ 0 \\ 0 \end{bmatrix} \end{aligned} \tag{4.13}$$

$$\begin{aligned}\dot{\mathbf{x}} &= f(q_2, \mathbf{x}, d) \\ &= \begin{bmatrix} \dot{\theta} \\ (-B\dot{\theta} + \tau_p + \tau_g + N\tau_m)/I_{all} \\ r\dot{\theta} \\ -P_a\dot{l}/l \\ P_b\dot{l}/(L-l) \end{bmatrix}\end{aligned} \tag{4.14}$$

where the input d is replaced with the motor torque $N\tau_m$, and L is a stroke of the cylinder. Note that the processes occurring in the chambers are assumed to be isothermal [69]. Domains of q_1 and q_2 are common and expressed as:

$$Dom(q_1) = Dom(q_2) := \{\mathbf{x} \in \mathbb{R}^5 | \underline{\mathbf{x}} \leq \mathbf{x} \leq \overline{\mathbf{x}}\} \tag{4.15}$$

where $\underline{\mathbf{x}} := [0, -\infty, 0, P_{atm}, P_{atm}]^T$ is the lower bound and $\overline{\mathbf{x}} := [0.7\pi, \infty, L, P_{supply}, P_{supply}]^T$ is the upper bounds of the state.

One of the main differences between Fig. 4.4 and Fig. 3.2 are edges and guards. The model in Fig. 4.4 has two edges, and these edges are defined as follows:

$$Edge := \{e_1, e_3\} = \{(q_1, q_2), (q_2, q_1)\} \tag{4.16}$$

Guards are set based on time t to enable the edges:

$$G(e_1) := \{t \in \mathbb{R} \mid t = t_1 = 0\} \tag{4.17}$$
$$G(e_3) := \{t \in \mathbb{R} \mid t = t_N = T_{end}\} \tag{4.18}$$

where $N = 2$ and T_{end} is an end time of a given task. Corresponding reset maps in Fig. 4.4 are defined as follows:

$$\mathbf{x}_\phi(t) := [\theta, \dot{\theta}, l]^T \tag{4.19}$$
$$\phi_1(\mathbf{x}_\phi, \mathbf{z}) := [\mathbf{x}_\phi^T, z(1), z(2)]^T \tag{4.20}$$
$$\phi_2(\mathbf{x}_\phi) := [\mathbf{x}_\phi^T, P_{atm}, P_{atm}]^T \tag{4.21}$$

where $\mathbf{z} \in \mathbb{R}^2$ is the only decision vector as an initial condition of chamber pressures, $P_a(0^+)$, $P_b(0^+)$. This vector determines an assistive torque τ_p provided by the AP2A in q_2 (i.e., *passive* mode) according to (4.11). The lower and upper bounds of the vector are defined as:

$$\underline{\mathbf{z}} \leq \mathbf{z} \leq \overline{\mathbf{z}} \tag{4.22}$$

where $\underline{\mathbf{z}} = [P_{atm}, P_{atm}]^T$ and $\overline{\mathbf{z}} = [P_{supply}, P_{supply}]^T$.

Problem Formulation

A task in this study was assumed to simulate tasks in factories, as a monotonous, repetitive, heavy load manipulation that is one of the major tasks achieved by industrial robots. An enormous

number of studies have been conducted on the design of motion controllers in this field since 1980s [121, 122, 123]. However, in order to align with the numerical analysis conducted in chapter 3, the motor torque τ_m was simplified to be a sum of a gravity compensation term and the output of proportional control, as described in (3.48) to (3.50). The desired trajectory θ_d is assumed to be the repetitive load manipulation so that it was expressed as a sinusoidal wave:

$$\theta_d(t) \quad := \quad \theta_0(1.5 + cos(2\pi f t)) \tag{4.23}$$

where f is a frequency of the motion.

Assuming a given task for a period T_{end}, a cost function is defined to minimize motor torque as discussed in section 3.2:

$$J(\mathbf{z}) := \int_0^{T_{end}} L(\mathbf{x}(t \mid \mathbf{z}))dt = \int_0^{T_{end}} (N\tau_m)^2 \, dt \tag{4.24}$$

Note that the desired trajectory in (4.23) is repetitive. For computational efficiency, a single period of the task is considered in this study (i.e., $T_{end} = 1/f$).

The whole problem is thus expressed as follows:

$$\min_{\mathbf{z}} \qquad J(\mathbf{z}) \tag{4.25a}$$

$$\text{s.t.} \begin{cases} \mathbf{x}_0 - \mathbf{x}(0) = 0, & (4.25b) \\ \dot{\mathbf{x}} - f(q, \mathbf{x}) = 0 & (4.25c) \\ g(\mathbf{x}, \mathbf{z}) = 0 & (4.25d) \\ h(\mathbf{x}, \mathbf{z}) \geq 0 & (4.25e) \end{cases}$$

The equations correspond as follows: Cost: (4.25a) $\rightarrow$ (4.24), Initial value: (4.25b) $\rightarrow$ (4.7), ODE model: (4.25c) $\rightarrow$ (4.13), (4.14), and constraints: (4.25d) $\rightarrow$ (4.20), (4.21) and (4.25e) $\rightarrow$ (4.15), (4.22), respectively.

Solution and Implementation

The cost (4.24) is implicit to decision variables $\mathbf{z}$. The problem was solved as an optimal parameter selection problem [119], and the same approach was introduced in this study. The derivation/proof of the method is not shown here as it is not the objective of this study.

The gradients of the cost functional J with respect to $\mathbf{z}$ are expressed as follows [119]:

$$\frac{\partial J}{\partial \mathbf{z}} = \lambda^T(t_0^+ \mid \mathbf{z}) \frac{\partial \mathbf{x}(t_0^+ \mid \mathbf{z})}{\partial \mathbf{z}} + \int_{t_0}^{t_f} \frac{\partial H \mathbf{x}(t \mid \mathbf{z}), \lambda(t \mid \mathbf{z}))}{\partial \mathbf{z}} dt \tag{4.26}$$

where t_0^+, t_f are the right limit of initial time and the terminal time, which are identical to $0, T_{end}$, respectively. The costate vector $\lambda \in \mathbb{R}^5$ of the system is derived as a solution of the backward initial-value problem:

$$\dot{\lambda}(t) = -\frac{\partial H}{\partial \mathbf{x}}, \quad \lambda(T_{end}) = 0 \tag{4.27}$$

Hamiltonian of the system H in (4.26) is described as follows:

$$H = L(\mathbf{x}(t \mid \mathbf{z})) + \lambda^T f(q, \mathbf{x}) \tag{4.28}$$

However, the Hamiltonian is not explicit with respect to $\mathbf{z}$ in this problem as shown in (4.24). Thus, (4.26) can be simplified as:

$$\frac{\partial J}{\partial \mathbf{z}} = \lambda^T(t_0^+)\frac{\partial \mathbf{x}(t_0^+ \mid \mathbf{z})}{\partial \mathbf{z}} = \lambda^T(0^+)\frac{\partial \mathbf{x}(0^+ \mid \mathbf{z})}{\partial \mathbf{z}} \tag{4.29}$$

The problem was solved in `MATLAB 2016b` installed in a laptop (Intel Core i-5, RAM 8GB). The derivatives (5.24) were computed as follows: compute the costate trajectory backward in time $t \in [0, T_{end}]$ with (5.25), and then calculate a partial derivative of (5.17) with respect to $\mathbf{z}$. The cost (5.22) was computed as follows: compute the state trajectory forwards in time $t \in [0, T_{end}]$ with (5.10) and (5.11), and then calculate the integral in (5.22) with the trajectory and given $\mathbf{z}$. `ODE45` solver was utilized to compute the state and costate trajectories, and the number of steps was 200. The trapezoidal rule was applied for the integral computation with the same step size. `fmincon` solver (internal point method) was used to solve the optimization problem (5.23) based on the computed gradient.

Initial values of the decision vector were set as mean of its lower and upper bounds:

$$\mathbf{z}_0 = 0.5(\underline{\mathbf{z}} + \overline{\mathbf{z}}) \tag{4.30}$$

In this study, the supply pressure P_{supply} was set at $5P_{atm}$. Tasks were assumed to be modified by changing the frequency f in (4.23), and simulations were conducted under $f = 0.1$,0.3 Hz. Note that Table 4.1 and 4.2 show the parameters of the pendulum used in this study.

Table 4.2: Parameters of the numerical model of the system in Fig. 4.2

Params (unit)	**Value**	**Params (unit)**	**Value**
θ_0 (rad)	0.26	l_0 (m)	$3.78 \cdot 10^{-2}$
I_{load} (kgm^2)	$3.84 \cdot 10^{-2}$	B (kgm^2/s)	$2.43 \cdot 10^{1}$
A_a (m^2)	$2.85 \cdot 10^{-4}$	A_b (m^2)	$2.53 \cdot 10^{-4}$
A_r (m^2)	$3.22 \cdot 10^{-5}$	r (m)	$3.00 \cdot 10^{-2}$
m_{arm} (kg)	$3.24 \cdot 10^{-1}$	m_{load} (kg)	2.97
l_f (m)	$3.00 \cdot 10^{-1}$	L (m)	$7.56 \cdot 10^{-2}$
P_{atm} (Pa)	$1.01 \cdot 10^{5}$	P_{supply} (Pa)	$5.07 \cdot 10^{5}$
K_p (Nm/rad)	$1.60 \cdot 10^{1}$	f (Hz)	$\{1.00, 3.00\} \cdot 10^{-1}$

Simulation Results

The computational time was less than 5 seconds under each condition. The optimal solution $\mathbf{z}^*$ to the problem (4.25) were:

$$\mathbf{z}^* \mid_{f=0.1} = [0.103, 0.472]^T \cdot 10^6 = [1.0, 4.7]^T P_{atm} \tag{4.31}$$

$$\mathbf{z}^* \mid_{f=0.3} = [0.224, 0.506]^T \cdot 10^6 = [2.2, 5.0]^T P_{atm} \tag{4.32}$$

The optimal solutions and the initial conditions (4.30) are shown in Fig. 4.5a and 4.6a. Fig. 4.5a and 4.6a show contours of the cost J in (4.24). Blue dotted lines indicate the range of chamber pressures. Fig. 4.5b and 4.6b show the array of computed cost with brute-force search by gridding the constraints of each decision variable (4.22) into 10 equal sections. Costs under the optimal solutions J^* and the control condition J_0 (i.e., no assistance) were as follows:

$$[J^*, J_0] \mid_{f=0.1} = [118, 232] \tag{4.33}$$

$$[J^*, J_0] \mid_{f=0.3} = [260, 314] \tag{4.34}$$

The costs J_0 are shown in Fig. 4.5b and 4.6b as flat, transparent surfaces.

Fig. 4.7 shows the simulation results in different coordinate systems. The axes are a pneumatic force F_p in (3.3) and stiffness K of the AP2A at the initial position. This transformation was computed as follows [106]:

$$\begin{bmatrix} F_p \\ K \end{bmatrix} = \begin{bmatrix} -A_a & A_b \\ A_a/(L - x_3(0)) & A_b/x_3(0) \end{bmatrix} \mathbf{z} + \begin{bmatrix} P_{atm} A_r \\ 0 \end{bmatrix} \tag{4.35}$$

Note that $\mathbf{z}$ is the decision vector as the initial conditions of chamber pressures, $P_a(0^+)$, $P_b(0^+)$. Dotted blue lines in Fig. 4.7 indicate the range in the transformed coordinate systems. Fig. 4.8 shows a relation between the assistive torque and the joint angle. A solid blue and orange lines show the stiffness curves under the different frequencies ($f = 0.1$ and 0.3 Hz), respectively. Solid black lines are linear approximations of the curves.

4.4 Experimental Validation

Experimental Conditions & Data Analysis

The frequency f of the desired trajectory θ_d in (4.23) was set to be 0.1 and 0.3 Hz in the same way as the simulation study. There were 10 pressure conditions which modifies passive assistance provided by the AP2A, including the control condition (no assistance provided by the AP2A). These 10 conditions were determined based on the simulation study. Considering of the contour and the optimal condition in Fig. 4.5a, the chamber pressure P_a was set as P_{atm}, and P_b was modified around the optimal condition when the frequency was set to be 0.1 Hz. In the other condition (i.e., f =0.3 Hz), P_a was modified around the optimum, while P_b was set around P_{supply} based on Fig. 4.6a.

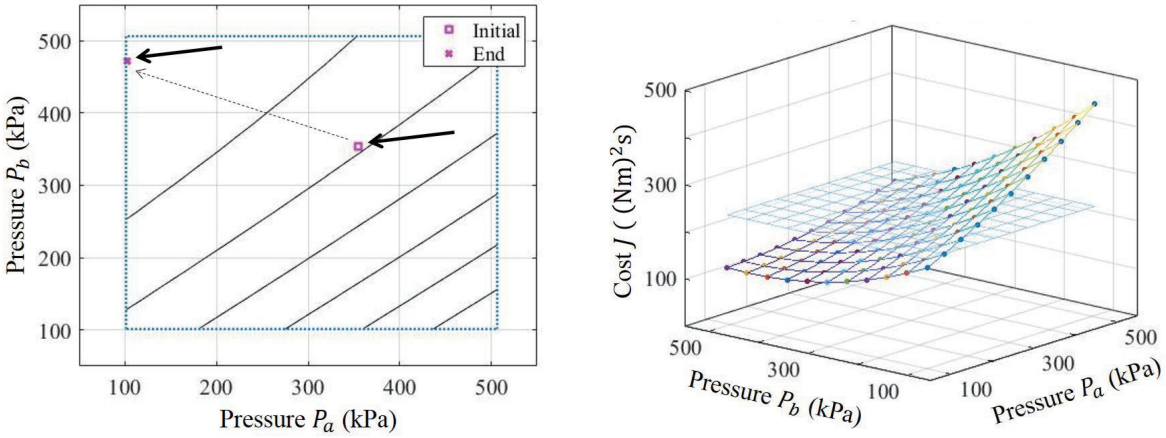

(a) Contour of cost J and the minimum. (b) Cost functions J and J_0.

Figure 4.5: Simulation results (f =0.1 Hz).

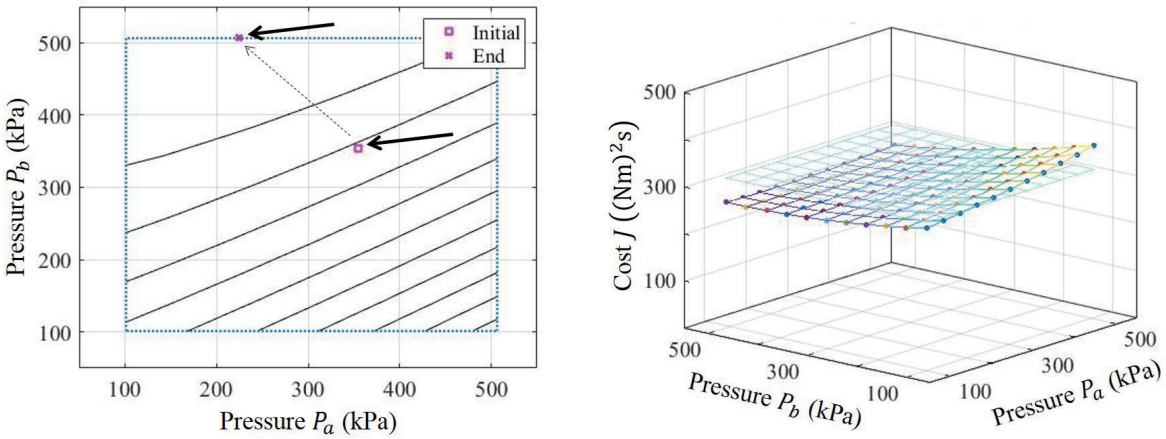

(a) Contour of cost J and the minimum. (b) Cost functions J and J_0.

Figure 4.6: Simulation results (f =0.3 Hz).

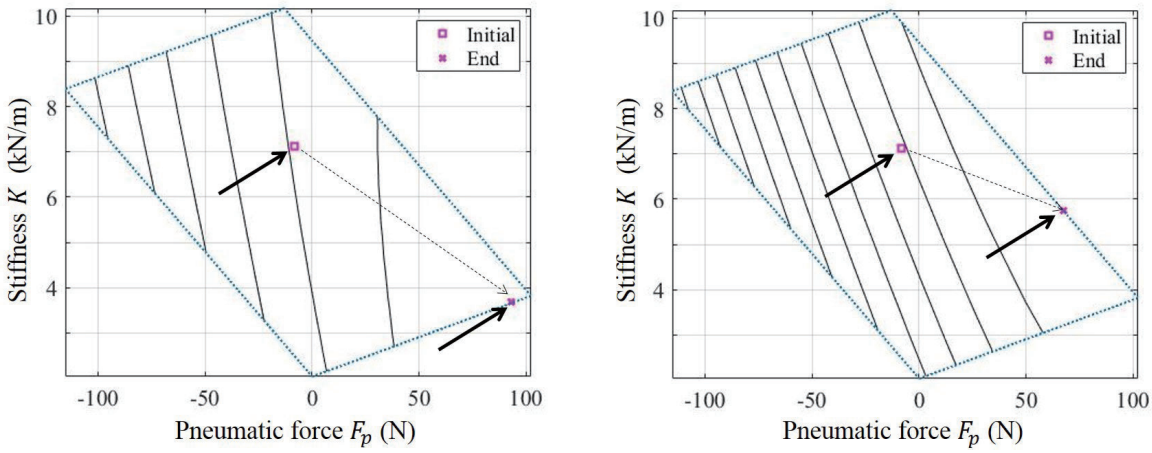

(a) Results of Fig. 4.5a.

(b) Results of Fig. 4.6a.

Figure 4.7: Simulation results of Fig. 4.5a and 4.6a in different coordinate systems.

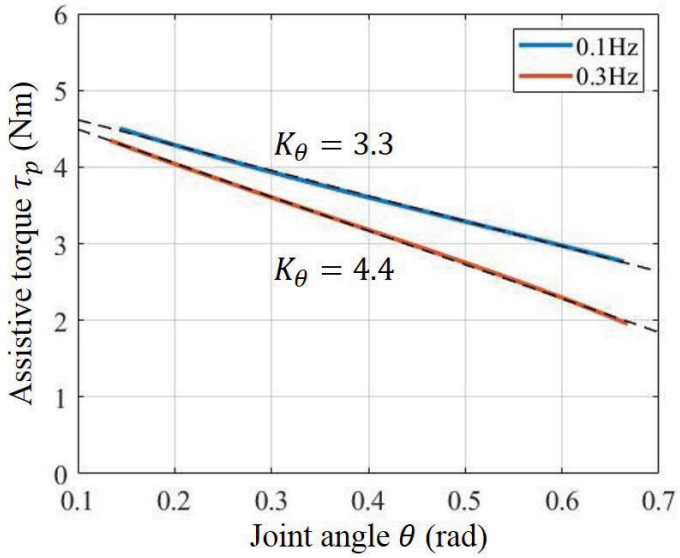

Figure 4.8: Stiffness curves and linear approximation computed in the simulation study.

In the experiments, the arm with an external load was lifted manually to the initial joint angle θ_0. The chamber pressures P_a and P_b were then modified, and the chambers were sealed after the modification. When all the initial conditions were set, the motor was actuated to follow the desired trajectory θ_d in (4.23). The experimental data (i.e., each state in $\mathbf{x}$ and the motor current i) were obtained in the steady-state. 7 cycles of the motion data were collected under each pressure condition. The cost in (4.24) was computed as follows:

$$J = \int_0^{T_{end}} (N\tau_m)^2 \, dt = \int_0^{T_{end}} (NK_t i(t))^2 \, dt \tag{4.36}$$

Note that T_{end} is a period of the task and is dependent on the experimental condition (i.e., $1/f$). An average of the experimental motor current i was used to compute the cost (4.36). A polynomial function of degree two was designed according to the computed costs, which was the minimum bounding plane that lay on the top of the costs [109]. Figures were created using `plot3`, `surf`, and `contour` functions in `MATLAB 2016b`.

Experimental Results

The pressure conditions which indicated the minimum costs J^* in the experiments were:

$$\mathbf{z}^* \mid_{f=0.1} = [0.082, 0.366]^T \cdot 10^6 = [0.81, 3.61]^T P_{atm} \tag{4.37}$$

$$\mathbf{z}^* \mid_{f=0.3} = [0.171, 0.448]^T \cdot 10^6 = [1.69, 4.42]^T P_{atm} \tag{4.38}$$

Empirical costs under the minimum condition J^* and the control condition J_0 (i.e., no assistance) were as follows:

$$[J^*, J_0] \mid_{f=0.1} = [214, 462] \tag{4.39}$$

$$[J^*, J_0] \mid_{f=0.3} = [68, 138] \tag{4.40}$$

All of the experimental conditions and corresponding costs are shown in Fig. 4.9 and 4.10. Black plots in those figures represent 10 pressure conditions confirmed in the experiments. Red plots were the pressure condition which indicated the minimum cost among others. Fig. 4.9a and 4.10a show contours of the estimated polynomial function. The costs J_0 are shown as flat, transparent surfaces in Fig. 4.9b and 4.10b. The experimental costs $\hat{J}$ under the optimal pressure conditions in (4.31) and (4.32) were estimated by the developed polynomial function as follows:

$$\hat{J} \mid_{f=0.1} = 260 \tag{4.41}$$

$$\hat{J} \mid_{f=0.3} = 102 \tag{4.42}$$

4.5 Discussion

Validation of Computational Search Method for Passive Assistance

The global minimum of the optimal control problem in (4.25) was able to find with the gradient method. Fig. 4.5a and 4.6a show the solution to the problem obtained by the gradient method.

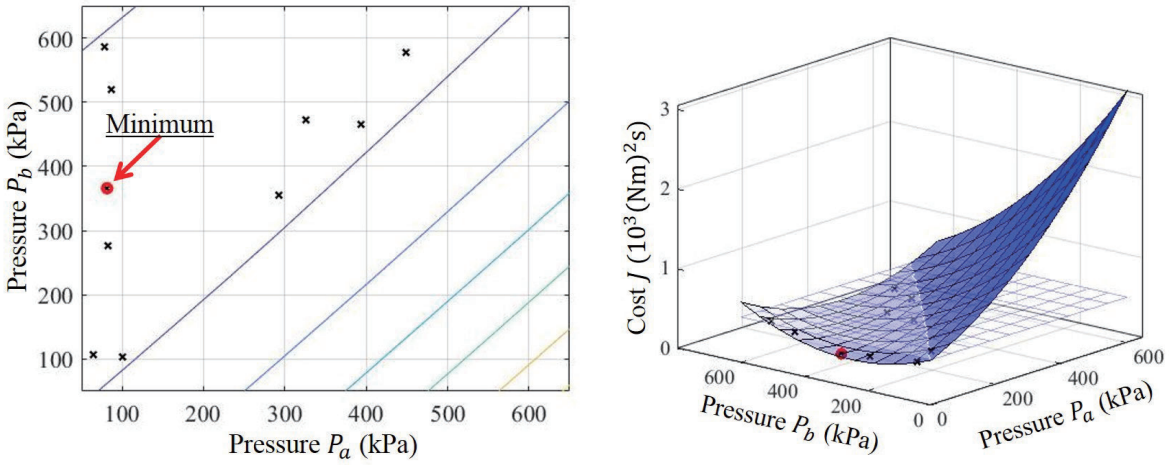

(a) Contour of estimated experimental cost J. (b) Estimated experimental cost function J and J_0.

Figure 4.9: Experimental results (f =0.1 Hz).

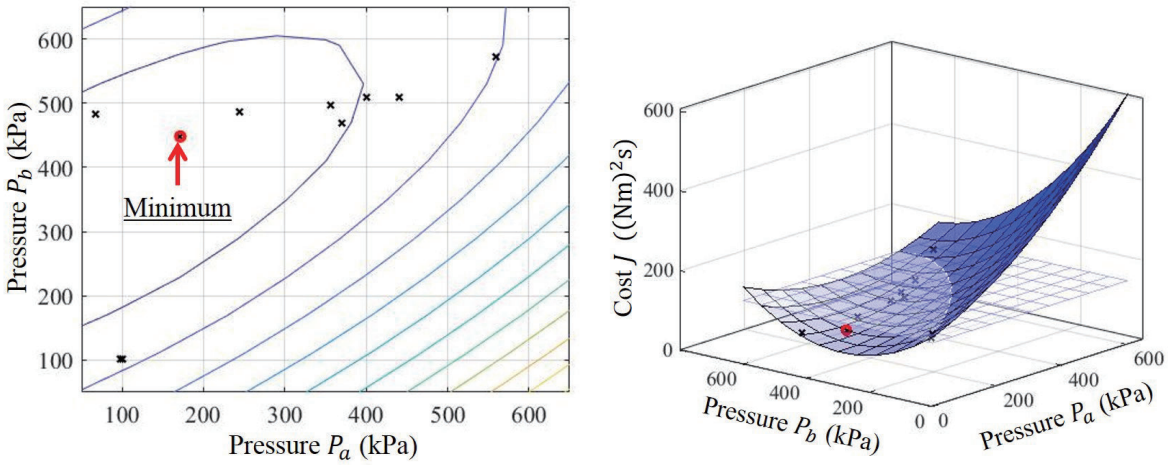

(a) Contour of estimated experimental cost J. (b) Estimated experimental cost function J and J_0.

Figure 4.10: Experimental results (f =0.3 Hz).

Fig. 4.5b and 4.6b provide intuitions of the optimization. Fig. 4.5 and 4.6 suggest that the solver was able to find the global minimum in the range of (4.22). The gradient in (4.26) was well computed and able to search for the minimum with `fmincon` solver. Note that the problem seemed to be a constrained convex problem in the range of (5.19), as shown in these figures. The solution was thus found to be the global optimum in this problem. However, it may be required to combine the gradient method with other searching methods such as Genetic Algorithm to find the global optimum if cost functions become complicated.

Along with the simulation study, the performance of the computational search method was confirmed throughout experiments. According to the experimental results, the minimum condition of a chamber pressure P_b^* in (4.37) was about 4.5 times larger than that of the pressure P_a^* which was close to P_{atm} when the frequency was set to be 0.1 Hz. A ratio of P_b^* to P_a^* reduced to 2.6 in the other condition (i.e., f =0.3 Hz), as P_a^* increased to about $1.5P_{atm}$ in (4.38). The same trends were confirmed in the results obtained from the simulation study. Ratios of P_b^* to P_a^* in (4.31) and (4.32) were about 5 and 2.3, respectively. The optimal condition in the simulation study and the minimum pressure condition found in the experiments were slightly different as suggested in (4.31) and (4.37). One of the reasons being that there were errors between a numerical model and experimental setups as the model neglected several nonlinear effects. However, estimated costs $\hat{J}$ in (4.41) and (4.42) were smaller than the cost without any assistance (i.e., J_0 in (4.39) and (4.40)). This fact suggests that, regardless of errors between the numerical model and the physical plant (i.e., the pendulum), the amount energy consumed by the motor (i.e., the cost J) could be reduced to perform the required tasks by modifying chamber pressures of the AP2A based on solutions of the optimal control problem. Thus, the computational search method successfully found references of chamber pressures for passive assistance to reduce the energy consumption of the pendulum.

The computational method introduced in this chapter may be useful when passive assistance is required rather than active assistance. Compared with the simulation conducted in chapter 3, the computational time decreased from 230 to 5 seconds, while both simulation results provided the optimal pressures for passive assistance. The reason being that the number of decision variables decreased from 11 to 2, such as (3.60) and (4.31). The computational method proposed in this chapter can only be used for passive assistance. However, the method could solve the problem much faster than the one proposed in chapter 3.

Analysis of Passive Assistance as Variable Stiffness Actuator

Passive assistance designed by the search method reduced the energy consumption of a pendulum in the experimental study. It is important to understand how the AP2A assisted the pendulum to reduce energy consumption. Dynamic responses of the AP2A in the *passive* mode are determined by the chamber pressures, $P_a(0^+)$ and $P_b(0^+)$. As discussed above, ratios of P_b^* to P_a^* obtained in the simulation studies were about 5 and 2.3 when the frequencies were set to be 0.1 and 0.3 Hz, respectively. However, these differences between P_a and P_b are not intuitive to understand the effects of passive assistance provided by the AP2A.

The effects of passive assistance can be analyzed from the viewpoint of the pneumatic force F_p and stiffness K of the AP2A by introducing a transformation in (4.35). Fig. 4.7 shows the simulation results in the transformed coordinate systems. The pneumatic force increased from the initial conditions regardless of the frequencies. As shown in Fig. 4.8, an assistive torques τ_p indicated positive values under both conditions. The force was utilized to produce the assistive torque performing gravity compensation of the load. To increase the assistive torque (i.e.,the pneumatic force) as much as possible, the stiffness K decreased to about $4\,\mathrm{kN/m}$ when the frequency f was $0.1\,\mathrm{Hz}$ (Fig. 4.7a). The stiffness indicated about $6\,\mathrm{kN/m}$ under the other condition (Fig. 4.7b). These differences of stiffness were confirmed as slopes of the curves in Fig. 4.8. In Fig. 4.8, the stiffness of the AP2A modified the joint stiffness K_θ (Nm/rad). These results suggest that, by tuning the chamber pressures of the AP2A, the dynamics of the pendulum about the joint was optimized to minimize the energy consumption. From the above, the AP2A worked as a variable stiffness actuator to improve the energy efficiency of the pendulum.

Advantages of Passive Assistance

Experimental results suggest that the AP2A may be able to reduce the energy consumption of a *whole* system by tuning chamber pressures appropriately. As described in (4.24), a cost J is the amount of energy consumed by a pendulum (i.e., a motor) in a single period (i.e., $1/f$) during a repetitive task. For each period, the amount of energy saved by the passive assistance ΔJ can be computed as a difference between costs with the assistance J^* and without any assistance J_0. The energy saved by the AP2A thus increases incrementally during the repetitive task. On the other hand, the energy consumed by the AP2A J_{ap} was defined as the amount of air consumed from the supply power source (i.e., a compressor) as discussed in section 3.2. With this model, the AP2A does not consume *any* energy in each period, as the chamber pressures are modified only *once* at the beginning of the task to provide passive assistance. When the sum of the saved energy ΔJ for each period during the task exceeds the energy consumed by the AP2A J_{ap}, it can be said that the AP2A reduces the energy consumption of the whole system (i.e., a pendulum *and* the AP2A) compared with that of the system without any assistance.

Another advantage of the AP2A is that the effort of replacing hardware may be reduced by implementing the AP2A. Fig. 4.7a and Fig. 4.7b show solutions to the optimization problem (4.25) under different frequency conditions. These figures suggest that the optimal pneumatic force and stiffness were dependent on the frequencies (i.e., task conditions). If assistive devices are developed with mechanical springs, the springs need to be replaced manually according to task conditions. With the AP2A as a variable stiffness actuator, hardware setups did not have to be modified other than chamber pressures in the experiments, while the AP2A could provide passive assistance without modifying hardware setups.

Limitation

There are several limitations in this study, as the performance of the AP2A and its controller were evaluated under limited conditions. First, desired trajectories in (4.23) were designed as sinusoidal waves with two frequencies. In general, desired trajectories of tasks are not limited to the sinusoidal waves. Another limitation is that the number of confirmed pressure condition may not be sufficient (i.e., 10 plots in Fig. 4.9a and 4.10a). As a future work, the numerical model of the hardware setups is required to be improved, and the performance of the AP2A needs to be further verified under various conditions.

4.6 Summary

This chapter empirically verified the performance of an Active/Passive Pneumatic Actuator (AP2A) and its high-level controller discussed in chapter 3. A numerical model of the hardware setups (i.e., a pendulum) was introduced and identified its parameters in section 4.2. A simplified optimal control problem was formulated with the system model by adding constraints to the previous problem. The constraints limited transitions between discrete modes, allowing the AP2A to provide passive assistance. A computational method was proposed to search the optimal pressures efficiently, which minimizes a joint torque produced by an electrical motor under the specific condition. Experimental conditions were determined based on the simulation study, and several pressure conditions were verified with a pendulum in the experiments. Similar trends were confirmed in the simulation and experimental results in terms of the optimal pressures (e.g., (4.31) and (4.37)) and cost functions (e.g., Fig. 4.5 and 4.9). Results from simulation and experimental study suggest that energy consumed by the pendulum was reduced under the optimal condition compared with that under the condition without assistance. From the above, by tuning the chamber pressures of the AP2A once at the beginning, passive assistance could reduce the energy consumption of the external power sources (i.e., a motor torque) while saving the supply air of the AP2A.

Chapter 5

Analysis of Verification Test with Human Subject

5.1 Chapter Overview

Performance of an Active/Passive Pneumatic Actuator (AP2A), as well as the high-level controller, is validated empirically in chapter 4. Experiments conducted in chapter 4 utilize a robotic system (i.e., a pendulum), which makes it possible to model the system and to estimate its energy consumption. Based on these experimental results, this chapter investigates the performance of the AP2A as assistive devices. An Active/Passive EXoskeleton-α (APEX-α) is introduced as an assistive device, which utilizes the active/passive framework [75]. Prior experimental results [74, 110] are reexamined in this chapter by gathering the knowledge acquired through the simulation study in chapter 4.

5.2 Hardware Design of Active/Passive EXoskeleton-α

Matthew et al. developed an Active/Passive EXoskeleton-α (APEX-α) in Fig. 5.1, which utilizes the active/passive framework [75]. The hardware design of the APEX-α is briefly explained in the following paragraphs. More details can be found in references such as [74, 75]. The APEX-α is comprised of two sub-assemblies as shown in Fig. 5.2; an arm and a backplate sub-assembly. A cable-driven system is adopted to connect these two sub-assembly in order to limit variations of the effective limb mass and moment of inertia. As a result, the total mass of the APEX-α is 2.54 kg with only 0.39 kg on the user's arm.

The arm sub-assembly is the cable-driven pulley for the elbow joint. A pair of Bowden cables run through a fixture on the pulley in opposite directions and up through a guide. Crimps at the ends of cables are used to secure the cable tensions. The arm sub-assembly consists of two separate bars, and the bars are attached to the user with adjustable aluminum cuffs around the upper arm and forearm, respectively. Thus, the rotation axis of the pulley is aligned with the user's elbow

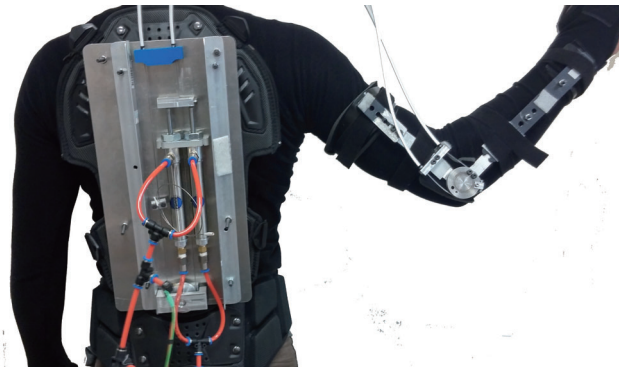

Figure 5.1: User wearing the APEX-α [74].

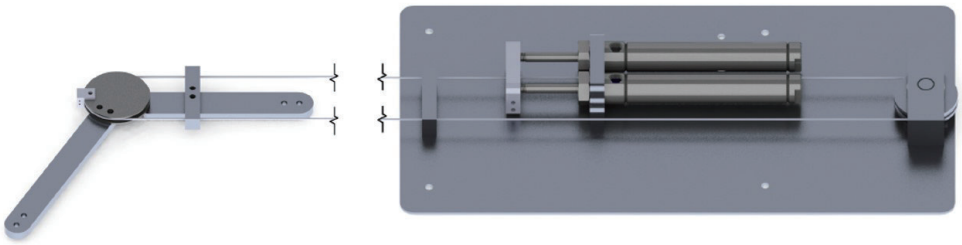

Figure 5.2: CAD design of an arm and a backplate sub-assembly of the APEX-α [74].

joint. The backplate sub-assembly which houses the air cylinders with valves and a pulley for the Bowden cables. Rods of the actuators are fixed to one cable with a clamping mechanism. The clamped cable winds around the stationary pulley on the backplate. The cable is then crimped to the end of the other cable, which creates a closed-loop. Therefore, the linear translation of the rods results in the rotation of the arm pulley via the Bowden cable.

5.3 Description of Prior Experimental Validation

Here experimental setups and conditions are briefly described based on prior work [74, 110].

Subjects

Six healthy individuals (five males, one female, aged 23$\pm$3 years, bodyweight 73.8$\pm$19.44 kg, height 1.77$\pm$0.08 m) were recruited under informed consent to evaluate the performance of the APEX-α. This experiment was approved by the Institutional Review Board of the University of California, Berkeley (IRB: 2012-12-4872).

Assist Conditions

The active/passive control framework was introduced for the APEX-α, which can be modeled as Fig. 4.4. The APEX-α can remain in the *passive* mode without additional power consumption while providing the assistive torque to the user. Its function in the *passive* mode was defined by the initial conditions of chamber pressures (i.e., $P_a(0^+)$ and $P_b(0^+)$). For example, by selecting the initial pressure conditions to have high stiffness around an elbow joint, the condition could imitate devices reducing magnitudes of physiological or pathological tremors [124, 125]. Table 5.1 shows four experimental pressure conditions, which were the combination of atmospheric pressure (P_{atm}) and the maximum supply pressure (P_{supply}), evaluating a wide pressure range of the actuator. Fig. 5.3 describes the pressure conditions in Table 5.1. The initial pressures on flexion and extension chambers (i.e., $P_a(0^+)$ and $P_b(0^+)$) are shown on discs. Initial pressures in sealed chambers are shown in green (P_{atm}) and orange (P_{supply}). Chambers open to the atmosphere (P_{atm}) are shown in blue. One of the control conditions C_{APEX} was defined as a condition activating the two-way valves to keep the atmospheric pressures (i.e., without assistance), and the other (i.e., condition C) was defined as a condition without the APEX-α. A *test* was defined as a trial in each condition.

Tasks

Dumbbell curls were chosen as it concentrates exertion to muscles producing the elbow motion, while the pronation of the wrist allowed for better ergonomic fit to the exoskeleton. A curl was

Table 5.1: Assist conditions of the APEX-α [74, 110]

		P_a	P_b	Valve States
Assist Conditions	1	P_{supply}	P_{atm}	Closed
	2	P_{atm}	P_{atm}	Closed
	3	P_{atm}	P_{supply}	Closed
	4	P_{supply}	P_{supply}	Closed
Control Condition	C_{APEX}	P_{atm}	P_{atm}	Open
	C	N/A	N/A	N/A

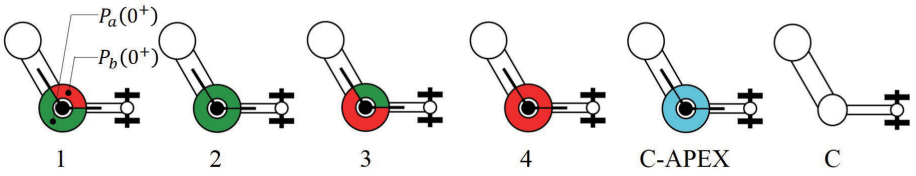

Figure 5.3: Side view of the arm and the load in each experimental condition [74, 110].

defined by a complete flexion and extension of the elbow (i.e., one repetition) with a dumbbell. As shown in Fig. 5.4, subjects sat on a curl weight bench to exclude effects from a shoulder joint, performing curls using their right arm at a frequency of 0.5 Hz. A *set* defined as a series of curls continued until failure, which was determined either objectively or subjectively. Failure was detected when subjects were not able to maintain the pace of 0.5 Hz or when subjects reported discontinuation due to muscular fatigue or discomfort. Three sets were performed with five minutes gap between each set in each test, in one day. Subjects were asked to perform six tests in a randomized order corresponding to the four assist conditions and two control conditions. The six tests were performed in two-day intervals to minimize any carryover fatigue effects between days.

Experimental Setups

Fig. 5.4 shows an overview of the experimental setups. Each subject wore the APEX-α, and an elbow joint of the subject and the exoskeleton were aligned manually. Besides, each subject put on active motion capture markers (Impulse X2, PhaseSpace Inc.). The curls were performed with a dumbbell of 3.59 kg. A metronome was set at 60 bpm in each set to ensure that all subjects moved at the desired frequency.

All subjects were asked to fully flex their elbows and to hold their postures while the actuators were pressurized at the beginning of each test. Chambers of the actuator were then connected to an air compressor, and the chamber pressures were all once pressurized to 446 kPa (i.e., $P_{supply} = 4.4P_{atm}$). According to the conditions in Table 5.1, any valves required to be opened to the atmosphere were opened if needed. In the end, all the valves were closed to maintain the amount of air in the chambers except the control conditions.

Figure 5.4: User performing dumbbell curls with the APEX-α in the experiment [75].

Data Analysis & Results

Fig. 5.5a shows the number of curls measured in each set as experimental results for each test. The investigator counted the number of performed curls and cross-checked against the motion capture data. In Fig. 5.5a, red, green, blue boxes indicate distributions of the first, second, and third sets among the subjects, respectively. Three sets in the same test are plotted next to each other in order, and the figure was plotted by `boxplot` function with `MATLAB 2016b`.

Total curl counts of each subject and each test were computed using results from the second and third sets. Then, those total counts were normalized respectively to their corresponding test of control condition *C* to confirm the effects of assistance in each test. Fig. 5.5b shows the normalized curl count for each test. The figure was also plotted by `boxplot` function. Table 5.2 shows the numerical results of Fig. 5.5b, showing mean and deviations of normalized values obtained under each condition. These results were obtained by `mean` and `std` functions with `MATLAB 2016b`.

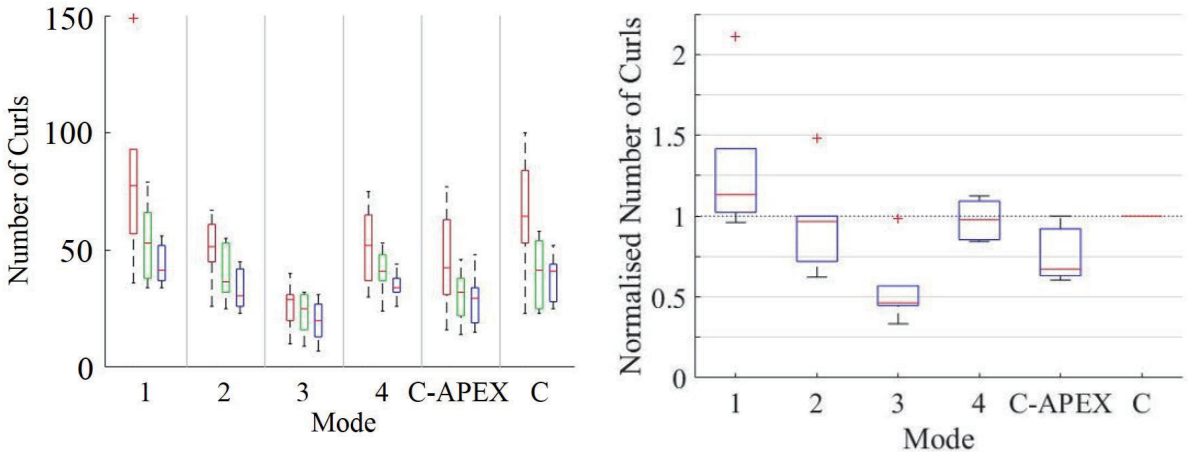

(a) Number of curl counts.

(b) Normalized number of curl counts.

Figure 5.5: Experimental results in each condition shown in Table 5.1.

Table 5.2: Mean and standard deviation of results in Fig. 5.5b

Experimental Conditions					
1	2	3	4	C_{APEX}	C
1.30 ± 0.48	0.96 ± 0.30	0.54 ± 0.23	0.98 ± 0.12	0.75 ± 0.17	1.00 ± 0.00

5.4 Simulation Study

A simulation study was conducted based on the experimental conditions. Compared to the simulation study in section 4.3, it becomes more difficult to model the external torque τ_{ext}. A simplified human elbow joint model is introduced in this study based on literature review.

System Modeling as Hybrid Systems

The model described in Fig. 4.4 is utilized in the following simulation study. Fig. 5.6 shows another representation of Fig. 4.4. The system is expressed as follows: $Q : q_1, q_2$, $X : (5.1)$, $f : (5.10), (5.11)$, $Init : (5.3)$, $Dom : (5.12)$, $E : (5.13)$, $G : (5.14), (5.15)$, $Re : (5.17), (5.18)$. There are two discrete modes, as shown in Fig. 4.4.

Schematics of the APEX-α is shown in Fig. 5.7. To represent the model, a continuous state vector $\mathbf{x} \in \mathbb{R}^5$ is defined as:

$$\mathbf{x}(t) := [\theta, \dot{\theta}, l, P_a, P_b]^T \tag{5.1}$$

$$\tag{5.2}$$

where $\theta, \dot{\theta}$ are the joint angle and angular velocity of an elbow joint, and l is a rod position, respectively. The initial states $Init(q1, \mathbf{x}(0^-))$ is expressed as:

$$\mathbf{x}(0^-) := [\theta_0, 0, l_0 + \theta_0 r, P_{atm}, P_{atm}]^T \tag{5.3}$$

where $\mathbf{x}(0^-)$ is the left limits of $\mathbf{x}$ at $t = 0$ (i.e., the state just before a transition), r is a radius of the connector, and l_0, θ_0 is the offset of the rod position and the initial joint angle, respectively.

As it was described in section 3.2, dynamics around the elbow joint in this model can be expressed as:

$$\begin{aligned} I\ddot{\theta} &= \tau_p + \tau_g + \tau_h && (5.4)\\ \tau_p &= (P_a A_a - P_b A_b - P_{atm} A_r) r && (5.5)\\ \tau_g &= -mgl_f sin(\theta) && (5.6) \end{aligned}$$

where I is the effective inertia of the forearm and exoskeleton including external loads, τ_p is the assistive torque, τ_g is the gravitational torque, and τ_h is the external torque provided by the user. Note that m in (5.6) is the mass of the forearm including exoskeleton and external loads (i.e., m_h and m_{ext}) in this section.

Comparing (5.4) with (3.6), the damping coefficient B is neglected in this model as friction around the arm sub-assembly is small owing to the design. However, the friction caused by the cable-transmission system was taken into consideration. The assistive torque τ_p is dependent on the pneumatic forces F_p produced by each cylinder and the efficiency of the cable-transmission system. With the radius of connector r, the assistive torque is modeled as:

$$\tau_p := 2\varepsilon F_p r \tag{5.7}$$

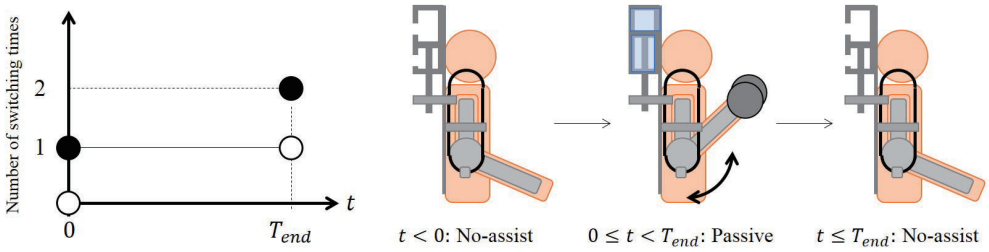

Figure 5.6: Another representation of Fig. 4.4 in the simulation study.

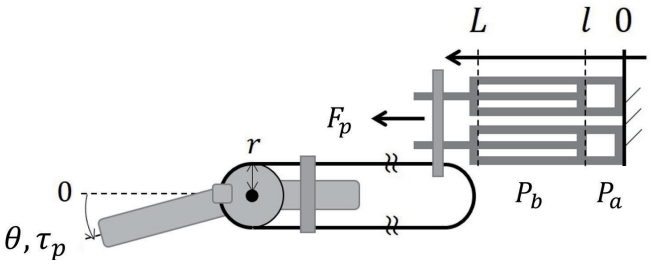

Figure 5.7: Schematics of the APEX-α based on Fig. 5.2.

where ε is a force transmission efficiency. In the previous studies [126, 127], the transmission efficiency ε was dependent on materials of the cable and the sheath (i.e., the coefficient of kinetic friction μ of these materials) as well as the wrapping angle of the cable Θ, which can be modeled as follows:

$$\varepsilon = \exp(-\mu\Theta) \tag{5.8}$$

In terms of the APEX-α, the wrapping angle Θ may not be constant in practice due to the user's shoulder movement, as shown in Fig. 5.1 and 5.4. The parameter is assumed to be constant in this study to focus on the movement engaging one degree of freedom (i.e., elbow motions). Based on the previous study [126], the force transmission efficiency ε is characterized as a ratio of the tension after the sheath T_2 to that before the sheath T_1:

$$\varepsilon = T_2/T_1 \tag{5.9}$$

Empirical trials were conducted to confirm the relation between input torque from the pneumatic actuator and output torque to the arm sub-assembly of the APEX-α. As a result, the coefficient ε in the system was found empirically to be 0.55 when the wrapping angle of the cable Θ was set to be 180 deg. The value seems to be reasonable as Carlson et al. suggested that the coefficient was around 0.6 when they used a steel cable with no lining [126]. The empirical results suggested that there was also static friction. However, it is neglected in this model. Thus, the dynamics in discrete

modes q_1 and q_2 are expressed with (3.1), (3.9), (3.10), and (4.9) as follows:

$$\dot{\mathbf{x}} = f(q_1, \mathbf{x}, d) = \begin{bmatrix} \dot{\theta} \\ (\tau_p + \tau_g + \tau_h)/I \\ r\dot{\theta} \\ 0 \\ 0 \end{bmatrix} \tag{5.10}$$

$$\dot{\mathbf{x}} = f(q_2, \mathbf{x}, d) = \begin{bmatrix} \dot{\theta} \\ (\tau_p + \tau_g + \tau_h)/I \\ r\dot{\theta} \\ -P_a\dot{l}/l \\ P_b\dot{l}/(L-l) \end{bmatrix} \tag{5.11}$$

where the input d is replaced with the user's joint torque τ_h, and L is a stroke of the cylinder. Note that a domain of q_1 and q_2 is common and it is:

$$Dom(q_1) = Dom(q_2) := \{\mathbf{x} \in \mathbb{R}^5 | \underline{\mathbf{x}} \leq \mathbf{x} \leq \overline{\mathbf{x}}\} \tag{5.12}$$

where $\underline{\mathbf{x}} := [0, -\infty, 0, P_{atm}, P_{atm}]^T$ is the lower bound of the states and $\overline{\mathbf{x}} := [7/9\pi, \infty, L, P_{supply}, P_{supply}]^T$ is the upper bound of the states.

The simulation model has two edges as shown in Fig. 4.4 which are defined as follows:

$$Edge \;:=\; \{e_1, e_3\} = \{(q_1, q_2), (q_2, q_1)\} \tag{5.13}$$

Guard conditions of assistive devices are generally dependent on the sensory outputs (e.g., outputs from an estimator [109]) to provide the users with suitable assistance. In order to separate the performance of the estimator, the guards $G(e_1), G(e_3)$ are enabled based on simulation time (Fig. 4.4) as follows:

$$G(e_1) \;:=\; \{t \in \mathbb{R} \mid t = 0\} \tag{5.14}$$

$$G(e_3) \;:=\; \{t \in \mathbb{R} \mid t = T_{end}\} \tag{5.15}$$

where T_{end} is an end time of a given task. There are reset maps ϕ_1, ϕ_2 for each edge that includes the initial conditions of the pressures for each discrete mode. The chamber pressures are assumed to be tuned instantaneously during transitions. The assistive torque provided by the APEX-α in q_2 depends on the chamber pressures, and it is determined by the initial conditions. A decision vector $\mathbf{z} \in \mathbb{R}^2$ is thus set to be the chamber pressures in reset maps ϕ_1 in Fig. 4.4 (i.e., $P_a(0^+)$ and $P_b(0^+)$) for computing suitable assistance during dumbbell curls as follows:

$$\mathbf{x}_\phi(t) \;:=\; [\theta, \dot{\theta}, l]^T \tag{5.16}$$

$$\phi_1(\mathbf{x}_\phi, \mathbf{z}) \;:=\; [\mathbf{x}_\phi^T, z(1), z(2)]^T \tag{5.17}$$

$$\phi_2(\mathbf{x}_\phi) \;:=\; [\mathbf{x}_\phi^T, P_{atm}, P_{atm}]^T \tag{5.18}$$

The lower and upper bounds of the vector are defined as:

$$\underline{\mathbf{z}} \leq \mathbf{z} \leq \overline{\mathbf{z}} \tag{5.19}$$

where $\underline{\mathbf{z}} = [P_{atm}, P_{atm}]^T$ and $\overline{\mathbf{z}} = [P_{supply}, P_{supply}]^T$. As a physical interpretation, this vector $\mathbf{z}$ modifies the assistive torque, which may increase or decrease the user's joint torque τ_h corresponding to the dynamics in (5.11).

Problem Formulation

Modeling the user's joint torque τ_h is a challenging task as it depends on the user's intention. In this study, the user is assumed to perform the repetitive motion (i.e., dumbbell curls) in q_2 when the guard $G(e_1)$ is enabled at $t = 0$. Bennett et al. investigated the stiffness of an elbow joint during cyclic, voluntary movement [128]. The study suggests that, without any loads, the mechanical properties of the joint were compliant ($\leq$15 Nm/rad), and approximated by a quasi-second order model. To move through its range of motion while carrying loads, a joint stability[1] can be increased by co-contraction of agonists and antagonists about the joint [129]. This fact suggests that the mechanical properties of the joint while carrying loads becomes stiffer than those without loads accordingly. The torque τ_h in q_2 is thus assumed to be the sum of outputs of a PD controller with high gains (i.e., high stiffness) and a gravity compensation term of the forearm weight, which performs the given task by following a reference θ_d:

$$\tau_h \;:=\; K_d(\dot{\theta}_d - \dot{\theta}) + K_p(\theta_d - \theta) + \mu m_h g l_f sin(\theta) \tag{5.20}$$

where μ is an error coefficient from the nominal model, K_d and K_p are constant gains representing damping and stiffness factor of the human joint. The given task in q_2 is set to be dumbbell curls, and the desired motion is expressed as follows:

$$\theta_d(t) \;=\; \theta_0(1 + cos(2\pi f t)) \tag{5.21}$$

where f is the frequency of the motion according to the previous experimental conditions [74].

It is important to determine a cost function in order to optimize the decision variables $\mathbf{z}$. The authors measured assistance provided by the APEX-α during dumbbell curls by counting the number of curls within a certain period [74]. The number of curls is assumed to be negatively correlated with the amount of joint torques produced by the muscles (i.e., τ_h). This assumption stems from the known fact that a low muscular force can be maintained longer than a high force. It is reasonable to focus on the joint torque during a single curl to optimize the entire amount of the torque as dumbbell curls are regarded as repetitive motions. From the above, the cost function within a period for a single curl T_{end} $(= 1/f)$ is defined as follows:

$$J(\mathbf{z}) := \int_0^{T_{end}} L(\mathbf{x}(t \mid \mathbf{z}))dt = \int_0^{T_{end}} \tau_h^2(t \mid \mathbf{z})dt \tag{5.22}$$

[1] A joint stability is defined in (section 2.4) of a reference [129] as "the ability of a joint to maintain an appropriate functional position throughout its range of motion".

The whole problem is expressed as follows:

$$\min_{\mathbf{z}} \quad J(\mathbf{z}) \tag{5.23a}$$

$$\text{s.t.} \begin{cases} \mathbf{x}_0 - \mathbf{x}(0) = 0, & (5.23b) \\ \dot{\mathbf{x}} - f(q,\mathbf{x}) = 0 & (5.23c) \\ g(\mathbf{x},\mathbf{z}) = 0 & (5.23d) \\ h(\mathbf{x},\mathbf{z}) \geq 0 & (5.23e) \end{cases}$$

The equations correspond as follows: Cost: (5.23a) $\rightarrow$ (5.22), Initial value: (5.23b) $\rightarrow$ (5.3), ODE model: (5.23c) $\rightarrow$ (5.10), (5.11), and path constraints: (5.23d) $\rightarrow$ (5.17), (5.18) and (5.23e) $\rightarrow$ (5.12), (5.19), respectively.

Gradient Formula for the Problem and Implementation

As well as the problem (4.25), the problem (5.23) was also solved by `fmincon` solver (internal point method) in `MATLAB 2016b`. Gradients of the cost functional J with respect to the decision variables $\mathbf{z}$ can be computed according to the prior work [119]:

$$\frac{\partial J}{\partial \mathbf{z}} = \lambda^T(0)\frac{\partial \mathbf{x}(0^+ \mid \mathbf{z})}{\partial \mathbf{z}} \tag{5.24}$$

The costate vector $\lambda \in \mathbb{R}^5$ in (5.24) is derived as a solution of the backward initial-value problem:

$$\dot{\lambda}(t) = -\frac{\partial H}{\partial \mathbf{x}}, \quad \lambda(T_{end}) = \mathbf{0}_{5\times 1} \tag{5.25}$$

where H is Hamiltonian of the system defined as:

$$H = L(\mathbf{x}(t \mid \mathbf{z})) + \lambda^T f(q,\mathbf{x}) \tag{5.26}$$

The costate trajectory was computed backward in time $t \in [0, T_{end}]$ with (5.25), and the result was multiplied with the partial derivative with respect to $\mathbf{z}$ to compute the gradients (5.24).

The cost (5.22) was calculated by computing the state trajectory forwards in time $t \in [0, T_{end}]$ with (5.11) with `ODE45` solver. The number of steps was set to 200. The integral in (5.22) was computed with the trajectory and given $\mathbf{z}$. The trapezoidal rule was applied for the integral computation with the same step size. Figures were created using `plot3`, `mesh`, `contour` functions. The initial values were set as mean of its upper and lower bounds as follows:

$$\mathbf{z}_0 = 0.5(\underline{\mathbf{z}} + \overline{\mathbf{z}}) \tag{5.27}$$

Parameters implemented in the simulation are shown in the following Table 5.3.

Table 5.3: Parameters of the numerical model in Fig. 5.7

Params (unit)	Value	Params (unit)	Value
P_{atm} (Pa)	$1.01 \cdot 10^5$	P_{supply} (Pa)	$7.09 \cdot 10^5$
θ_0 (rad)	1.22	l_0 (m)	$1.10 \cdot 10^{-2}$
r (m)	$2.00 \cdot 10^{-2}$	A_r (m^2)	$3.22 \cdot 10^{-5}$
A_a (m^2)	$2.85 \cdot 10^{-4}$	A_b (m^2)	$2.53 \cdot 10^{-4}$
I (kgm^2)	$6.00 \cdot 10^{-2}$	l_f (m)	$3.00 \cdot 10^{-1}$
m_h (kg)	1.50	m_{ext} (kg)	3.59
ε	$5.50 \cdot 10^{-1}$	L (m)	$7.62 \cdot 10^{-2}$
K_d (Nms/rad)	$4.00 \cdot 10^1$	K_p (Nm/rad)	$1.20 \cdot 10^2$
μ	$9.00 \cdot 10^{-1}$	f (Hz)	$5.00 \cdot 10^{-1}$

Simulation Results

The computational time was about 25 seconds, and the optimal solution $\mathbf{z}^*$ to the problem (5.23) were:

$$\mathbf{z}^* = [0.418, 0.101]^T \cdot 10^6 = [4.12, 1.00]^T P_{atm} \tag{5.28}$$

Fig. 5.8a shows a contour of the cost (5.22) and plots under the initial and optimal conditions that correspond to (5.27) and (5.28). Fig. 5.8b shows the array of computed costs (5.22) with brute-force search by gridding the constraints of each decision variable (5.19) into ten equal sections. Fig. 5.9a shows a relationship between the joint angle θ and the user's torque τ_h computed by (5.20). Fig. 5.9b shows a relationship between the angle and the computed assistive torque τ_{exo} provided by the APEX-α during a single curl. In both figures, a solid black line represents the data computed under the experimental condition *C*. Solid, red, green, and blue lines represent the data computed under the optimal condition (5.28) and the experimental conditions 1, 3 in Table 5.1.

Table 5.4 shows computed costs (5.22) under the optimal condition (5.28) and other empirical conditions. Table 5.5 shows the costs under condition *C* divided by that of each condition in Table 5.4.

5.5 Discussion

Test Validation

Fig. 5.5a shows the results of every set in all tests observed from all the subjects. A general trend can be confirmed that the number of curls decreased by repeating the sets. Comparing median values, it can also be confirmed that decreases between the first and second sets were more significant than those between the second and third sets. On the other hand, the standard deviations of the second and third sets among the subjects were significantly lower than that of the first set for all

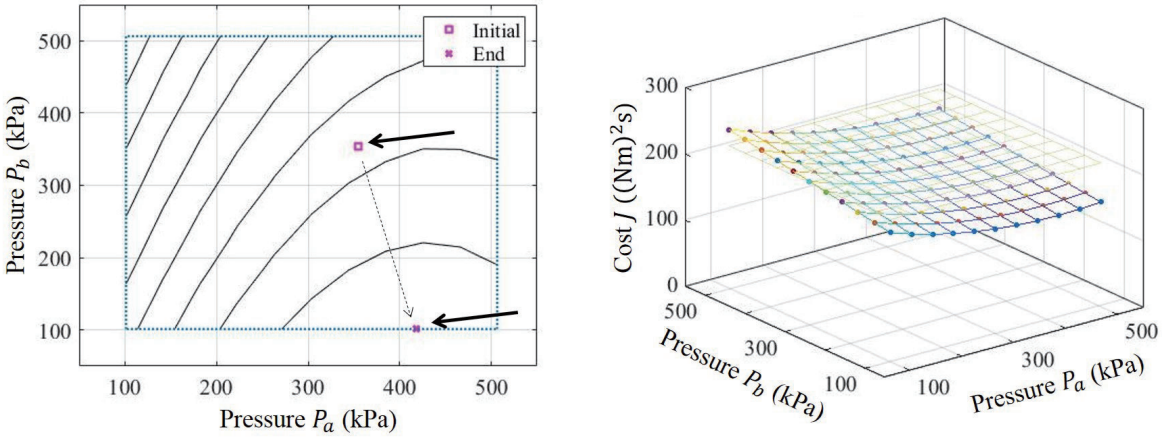

(a) Contour of cost J and the minimum.

(b) Cost function J in (5.22).

Figure 5.8: Simulation results as a solution to the problem (5.23).

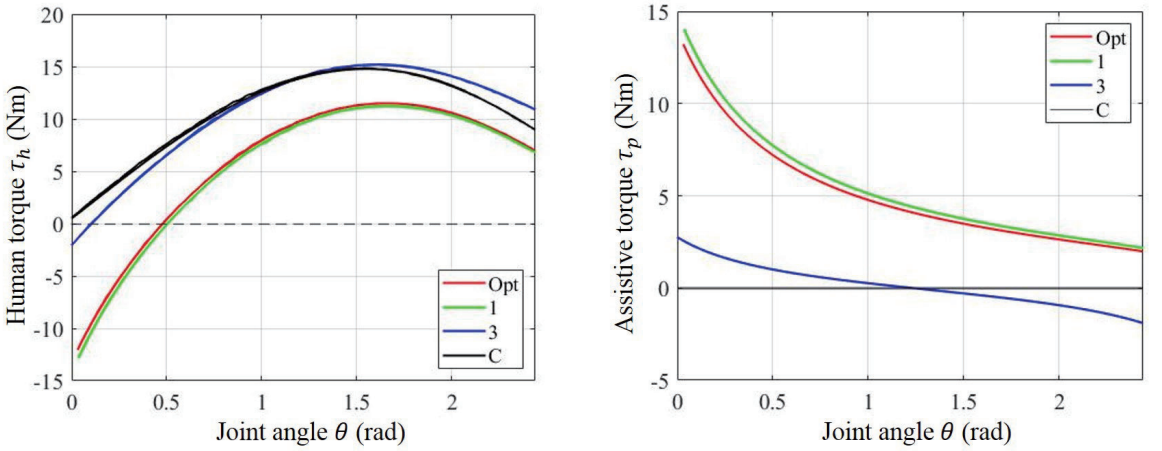

(a) Human joint torque.

(b) Assistive torque provided by the AP2A.

Figure 5.9: Stiffness curves during a curl under the optimal and other conditions.

Table 5.4: Computed costs by (5.22) for experimental conditions

	Experimental Conditions					
Opt	1	2	3	4	C_{APEX}	C
151	151	193	230	178	213	213

Table 5.5: Costs J_C divided by each cost in Table 5.4

	Experimental Conditions					
Opt	1	2	3	4	C_{APEX}	C
1.41	1.41	1.10	0.93	1.20	1.00	1.00

tests. These results suggest that the initial test was assumed to have variability. Based on these observations, the results of the first set were neglected as they may not be suitable to evaluate the performance of the APEX-α which is designed for long-term use in daily lives. Besides, each subject's curl counts were normalized to the corresponding test of control condition C, as reductions of curl counts were dependent on the subjects. The results in Fig. 5.5b and Table 5.2 are discussed as experimental results for further discussion.

Validation of Simulation Study for Optimality

As a simulation result shown in (5.28), assist condition 1 can be said to the optimal condition. Although a performance index of the experiments (i.e., the number of curls) was different from that of the simulation study (i.e., the user's joint torque), it is speculated that the better the APEX-α assisted the user in the experiments, the more the number of curls increased. Now the empirical result under assist condition 1 is compared with those under the other three modes (i.e., $2,3,4$). Fig. 5.5b suggests that the largest normalized number of curls was observed under the assist condition 1. This result suggests that the APEX-α provided the best assistance under the assist condition 1 among other conditions, which was identical to the simulation result. Therefore, it can be said that the optimal condition could be found through the simulation study.

Validation of Assistance with APEX-α

The experimental study suggests that the APEX-α could adapt to the user's task by optimizing the initial pressures with the proposed control framework. When an assistive device is not optimized, the user's performance may degrade by wearing the device. For example, comparing the results of two control conditions (i.e., C_{APEX} and C) in Fig. 5.5b, the normalized number of curls decreases when subjects just wore the APEX-α. This result is most likely due to the low transmission efficiency caused by frictions of Bowden cables, as described in (5.9). However, the median

value observed in condition 1 was larger than one, which is the value for the control condition C. The mean value of assist condition 1, including an outlier in Fig. 5.5b, was found to be 1.30. These results suggest that the APEX-α was able to provide the subjects with assistance improving performances of dumbbell curls in the experiments while compensating effects of the frictions.

As is the case with Fig. 5.5b, Table 5.2 indicates its quantitative results. All conditions except condition 3 were able to assist the user appropriately (i.e., increasing the number of curls compared to the control condition C_{APEX}). As a physical interpretation of Table 5.2, the assistive torque τ_p produced under condition 1 helped the user with flexing their elbow joints. Since $P_a(0^+)$ is larger than $P_b(0^+)$, the APEX-α started to provide a positive assistive torque. It can be said that the subjects were assumed to have a lighter load during dumbbell curls under condition 1, and accordingly, the subjects could save some amount of their joint torques required to achieve the task. From this point of view, it is reasonable that the ratio of the cost J_C to the cost J_1 in Table 5.5 becomes larger than one, as the APEX-α reduces the user's joint torque (i.e., the cost J in (5.19)). Fig. 5.9a obtained from the simulation study suggests that the user's torques τ_h were decreased under the optimal and the condition 1 compared to the torque under the condition C. The APEX-α is assumed to have provided a positive assistive torque in the experiments as suggested in the simulation results Fig. 5.9b under the optimal and condition 1. Fig. 5.9b also supports discussion in previous chapters that the APEX-α can tune its dynamic properties (e.g., stiffness) in the *passive* mode just by modifying the initial chamber pressures.

Aside from the optimal assistance, the median value observed under condition 2 was almost equal to one. Chamber pressures under the condition 2 saved the amount of air from a supply pressure source, as the condition was identical to atmospheric pressure (i.e., $P_a(0^+) = P_b(0^+) = P_{atm}$). The APEX-$\alpha$ did not consume *any* air from the compressor under this experimental condition. Based on these observations, it is interesting to note that the frictions were compensated just by closing the two-way valves of the APEX-α in the same way as the results discussed in section 3.4. Notice that Table 5.1 shows that the only difference between condition 2 and the control condition C_{APEX} was the valve states. When the valves were kept open, pressures did not change in both chambers of the AP2A. By closing the valves, the AP2A worked as a nonlinear spring, which enabled the AP2A to store potential energy of the load during extension and to convert the energy to kinetic energy as assistance during flexion. Besides, it is important to mention that only a little amount of supply air was consumed at the beginning of every pressure condition. The compressor can thus be replaced by a portable cartridge system, and the devices could be suitable for long-term operation used in daily life. From the above discussion, the APEX-α has the potential to function as a mechanical spring that can adapt to the user's task.

Comparison between Simulation and Experimental Results

A similar tendency can be confirmed in numerical and experimental results. When comparing Table 5.5 with Table 5.2, the best performance can be confirmed under condition 1 (1.30 in Table 5.2 and 1.41 in Table 5.5, respectively). The worst performance can be confirmed under the same assist condition 3 in both simulation and empirical results (0.93 and 0.54, respectively), as it is the

only condition that is assumed to resist the subject's motion. Note that the performance index of the simulation study in Table 5.5 was different from that of the experiments in Table 5.2. As mentioned above, the values in Table 5.2 indicate the normalized number of curls in the experiments. Instead, the values in Table 5.5 show the normalized, squared user's joint torque during a single curl. It is speculated that the more the number of curls increased, the better the APEX-α assisted the user in the experiments. It means that the number of curls decreases if the user is required to produce more joint torque in each curl due to insufficient/exceed assist torque provided by the APEX-α. The amount of the squared user's torque during a single curl is thus assumed to be negatively correlated with the number of curl in the experiments. However, there is still no meaning to compare the magnitudes of the values in Table 5.2 with those in Table 5.5. If a function that indicates a relation between the user's joint torque and the number of curls is discovered, it may support and reinforce the discussion above.

Limitation

There are several limitations in terms of experimental conditions and the simulation. First, the performance of the APEX-α was only confirmed when the task was set to be dumbbell curls. It is required to validate the performance of the device in other tasks/movements if the APEX-α is aimed to use in daily life. Second, curl counts were only used as an index to evaluate the performance of the APEX-α. It may be also important to consider the effects on a shoulder joint and/or a low back as well as the elbow joint. Third, some experimental results were not able to explain with the simulation study. For example, some subjects did not improve their performance under the optimal assist condition (i.e., assist condition 1), as shown in Fig. 5.5b. One of the reasons may be that individual differences were not taken into consideration in the simulation. A human kinematic and dynamic modeling [130, 131] will be developed in conjunction with improving the accuracy of the simulation study.

5.6 Summary

This chapter analyzed the prior experimental study [74, 110], utilizing a control framework proposed in chapter 4. An Active/Passive EXoskeleton-α (APEX-α) was introduced as the hardware design that utilizes an Active/Passive Pneumatic Actuator (AP2A). The prior experimental conditions and the results were described briefly in the following section. A simulation study was conducted to analyze the effects of passive assistance in the experiments. A mathematical model of the APEX-α was described with the friction caused by the cable and the sheath. Besides, a human joint torque was modeled based on the knowledge from prior work. An optimal control problem was formulated and solved in the same way as chapter 4 in order to search the optimal pressures for suitable assistance of the APEX-α. Experimental results suggested that the AP2A could improve the users' performance (i.e., increased the number of curls) under the optimal pressure condition. Other similar trends were also confirmed between the experimental and the simulation results by

comparing 5.2 with 5.5. From the above, the proposed high-level controller of the AP2A may be useful for assistive devices to find suitable assistance under specific conditions.

Chapter 6

Intention Estimation using Bio-signals

6.1 Chapter Overview

This chapter introduces a framework to design a binary classifier with surface electromyography (sEMG) for the assistive devices. Performance of an Active/Passive Pneumatic Actuator and its high-level controller are validated with a pendulum and human subjects in chapters 4 and 5. In terms of the high-level controller in Fig. 4.4, there is an assumption that the pendulum starts and finishes its task at time $t = 0$ and T_{end}, respectively. This assumption is no longer satisfied when assistive devices are used in daily lives.

This chapter proposes a framework for assistive devices such as an exoskeleton to develop a sEMG classifier that detects the assistive timing. Based on the experimental condition in chapter 5, this sEMG classifier aims to detect if its user performs dumbbell curls or not. The framework reduces the number of tasks to collect training data before using the devices. Experiments are conducted to validate the performance of the classifier, and results suggest that the classifier can detect the assist timing accurately.

6.2 Classification Framework with Less Training Data

Concepts of Proposed Classification Framework

Surface electromyography (sEMG) is one of the most popular bio-signals to estimate human motions. It is natural to select physiological signals related to muscular activation in order to classify the movements. In this study, the movements are classified into two classes; movements with and without a load. Larger joint torques are required to achieve the movements with the load (i.e., dumbbell curls) compared to those without the load. Muscles are largely activated to produce large joint torques, as the muscles are actuators of the human body. Spatiotemporal summation of the muscular activation can be measured as sEMG with appropriate sensors. The upper figure in Fig. 6.1 conceptually indicates differences of sEMG confirmed in the movements with and without

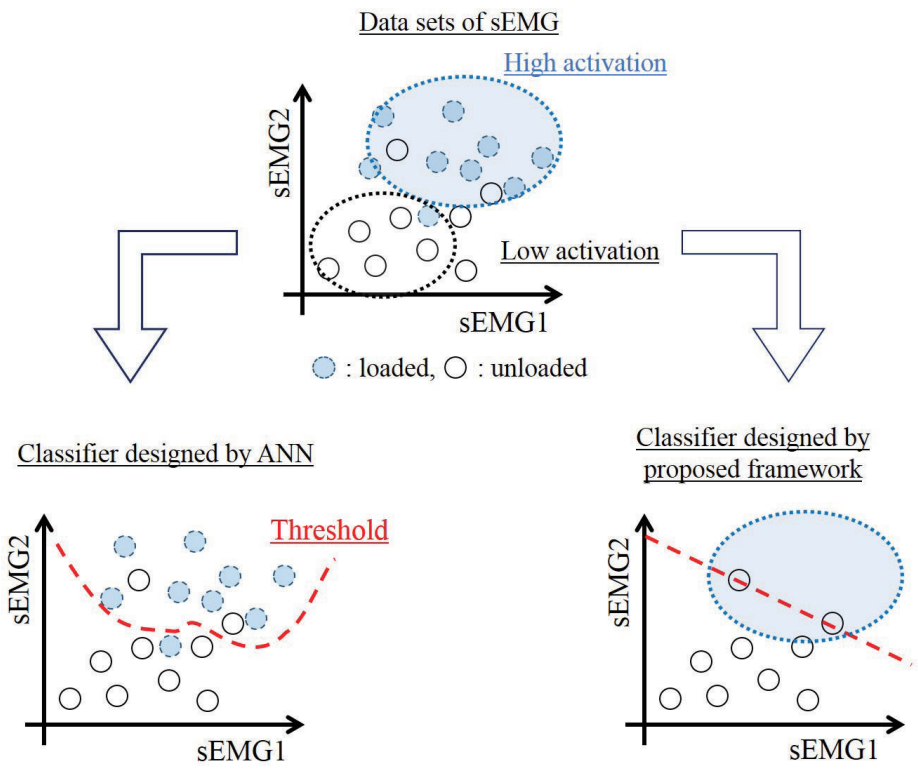

Figure 6.1: Difference of classifiers designed by the ANN and the proposed framework.

a load. In the figure, sEMG under loaded/ unloaded muscular states are shown in blue and white circles. These plots are assumed to show a trend according to the above discussion.

The lower figures in Fig. 6.1 outline differences of classifiers designed by an artificial neural network (ANN) and a proposed framework. Dotted red lines suggest threshold functions designed by each algorithm to classify these muscular states. Since the ANN is designed for *any* inputs to develop a function that classifies several data, all the data are required to train the ANN. For example, the ANN requires two different training data to solve the binary classification problem in Fig. 6.1, which is defined as S and $\neg S$. S are training data obtained during a repetitive load-lifting motion (i.e., blue circles in Fig. 6.1). $\neg S$ are training data except the data obtained in the condition of S (i.e., white circles as unloaded muscular states). Based on the data S and $\neg S$, the ANN can find a function as a threshold that classifies these two data. On the other hand, the proposed framework utilizes the data $\neg S$ to develop the threshold function. As discussed above, the sEMG data in this problem are assumed to show a trend. Based on this assumption, the threshold function is set to be the minimum bounding plane that lies on all the observed data in the unloaded muscular state ($\neg S$). The use of prior knowledge may enable the device users to reduce procedures to obtain training data S while the function classifies S and $\neg S$ as well as the function designed by the ANN.

Sensors and Tasks for Collection of Training Data

The performance of the proposed framework depends on the choice of training data $\neg S$. The data $\neg S$ in Fig. 6.1 only include sEMG. However, measurable data are not limited to the sEMG signals. Based on the Hill muscle model, a joint angle and the angular velocity are utilized as training data in addition to sEMG. The muscle model can be divided into an active contractile element and passive elastic elements [132]. A muscular force F_{ce} produced by the active contractile element can be expressed as follows:

$$F_{ce} = f(l, \dot{l})a \tag{6.1}$$

where $f(l, \dot{l})$ is a function of a muscular length and contraction velocity, and a is series of neural signals which activate the muscle. However, this muscular length l and contraction velocity $\dot{l}$ can not be measured from the body surface. Considering of an analogy between the flexor/extensor muscle groups and the elbow joint dynamics, the above three parameters F_{ce}, l and $\dot{l}$ are assumed to be related to the joint torque τ_h, the joint angle θ, and the angular velocity $\dot{\theta}$, respectively. Then, (6.1) can be modified as follows:

$$\tau_h \approx f_h(\theta, \dot{\theta}) \cdot sEMG \tag{6.2}$$

Note that sEMG is assumed to be a spatiotemporal summation of the neural signal a. Based on this assumption, sEMG is expected to show a larger value with fixed $\theta, \dot{\theta}$ when the user is in the loaded muscular state compared to the unloaded state.

Tasks for obtaining training data $\neg S$ determine the performance of classifiers as well as the classifier designed by the proposed framework. The binary classifier in this problem is required to distinguish the loaded/unloaded muscular states. With the proposed framework in Fig. 6.1, it is reasonable to obtain training data $\neg S$ which indicate the largest sEMG in order to improve the classification accuracy. Based on (6.2), sEMG has a positive relation with joint torques τ_h. sEMG is expected to have a positive relation with angular acceleration and shows the largest value during the fastest motion. Thus, the task to obtain the training data is decided to be the motion without a dumbbell at the highest frequency (i.e., the fastest motion).

6.3 Experimental Validation

Subjects

A cohort of three healthy individuals (three males, mean age 26.3 years) was recruited under informed consent to evaluate the performance of the classifier developed by the proposed framework. This experiment was approved by the Institutional Review Board of the University of California, Berkeley (IRB: 2012-12-4872).

Experimental Conditions for Collection of Training Data

Frequencies of the task were determined empirically, confirming that all subjects were able to perform elbow flexion and extension using the full range of motion. The fastest motion was set to

be at 1.0 Hz to obtain training data (i.e., $\neg S$) in this experiment. On the other hand, a frequency for testing data during a repetitive motion with a dumbbell of 3.59 kg (i.e., the loaded muscular state) was defined at 0.25 Hz. Based on the frequency, the other frequencies for testing data obtained in the unloaded muscular state were determined at 0.25 and 0.5 Hz. Summarizing the experimental conditions, subjects performed elbow flexion and extension using the full range of motion 5 times in each of the conditions in Table 6.1. Fig. 6.2 shows a subject's motion during the experimental task (iv). A metronome was used to ensure subjects moved at the desired frequency during the experiments. Subjects were asked to be relaxed and perform naturally so as not to co-contract their muscles intentionally.

Data Collection

An overview of the experimental setup is shown in Fig. 6.3. Each subject wore the devices on their right arm. All sensors used in the experiment were connected to a PC for synchronized sampling. MYO (Thalmic Labs [133]) were used to measure sEMG in this experiment. MYO consists of eight dry sEMG electrodes. One of the electrodes placed on the top of biceps by locating MYO on the upper arm, as shown in Fig. 6.3. sEMG was sampled at 50 Hz providing eight channels of 8-bit, with the data transferred to the computer via Bluetooth. Note that, in terms of quantitative

Table 6.1: Experimental conditions for each task

	Tasks			
	(i)	**(ii)**	**(iii)**	**(iv)**
Frequency (Hz)	0.25	0.5	1.0	0.25
Load (Dumbbell)	×	×	×	◯
Used as Test Data?	◯	◯	×	◯
Used as Training Data?	×	×	◯	×

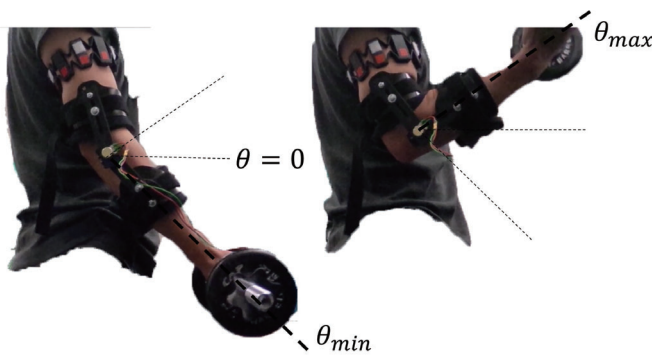

Figure 6.2: Elbow flexion and extension performed by subjects during the experimental task (iv).

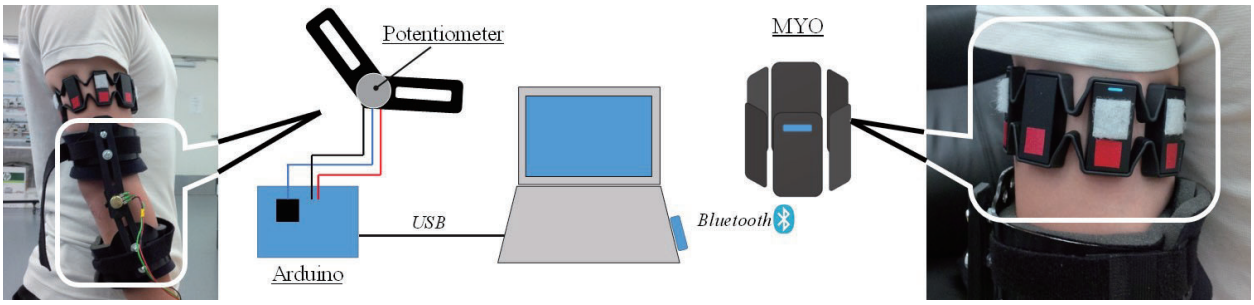

Figure 6.3: Overview of the experimental setups.

sEMG analysis, it is important to follow the guidelines (e.g., [134]) to certify several conditions, such as the sampling rate and placements of electrodes. MYO did not have enough sampling rate (i.e., up to 200 Hz) for the analysis, and it was not suitable to place its electrodes properly to target muscles. However, the aim of this experimental study was not focusing on sEMG analysis such as signal processing. The aim was to validate the performance of the sEMG classifier designed by the proposed framework. Thus, a simple wireless measurement device, MYO, was introduced in this experiment, which has been exploited in the fields of assistive devices [135]. A 3D printed device with a potentiometer measured an elbow joint angle during experiments. The potentiometer was aligned with a rotation axis of the subject's elbow. A voltage of the potentiometer was sampled by a micro-controller (Arduino Leonardo) at 50 Hz. A resolution of the angle was found to be 0.3 deg.

Data Processing and Analysis

The Euclid-norm of eight sEMG signal from MYO was calculated, and the fifth order moving average filter was then applied to the norm for smoothing. The measurement noise in the angular data was removed using the third-order low-pass Butterworth filter with cut-off frequency at 4 Hz (`MATLAB 2016b`). The angular velocity was estimated from the filtered joint angle by discretization.

According to the proposed framework in section 6.2, an algorithm to design the threshold function was interpreted into the following constrained optimization problem:

$$\min_{\Theta} \quad J(\Theta) = \sum_{i=1}^{m} \frac{1}{2m} (h(\Theta, x^{(i)}) - y^{(i)})^2 \tag{6.3a}$$

$$\text{s.t.} \begin{cases} h(\Theta, x^{(i)}) = X^{(i)}\Theta & (6.3b) \\ h(\Theta, x^{(i)}) \geq y^{(i)} & (6.3c) \end{cases}$$

where m is the size of training data, $x^{(i)} \in \mathbb{R}^2$ is the i^{th} sample from the training data for the joint angle and angular velocity, $y^{(i)} \in \mathbb{R}$ is the i^{th} sEMG sample, Θ is the coefficients of the function, and $h(\Theta, x^{(i)})$ is a polynomial function in the two variables with the coefficients. The joint angle

and angular velocity were used as features in this study since these two parameters were assumed to be related to sEMG as explained in (6.2).

The dimensions of Θ and $X^{(i)}$ are dependent on the degree of polynomial function $h(\Theta, x^{(i)})$. The degree of polynomial $h(\Theta, x^{(i)})$ was varied from zero to three to compare the classification accuracy with different orders as described in section 6.4. For example, if $h(\Theta, x^{(i)})$ is a polynomial function of degree two, then $\Theta \in \mathbb{R}^6$, and $X^{(i)} \in \mathbb{R}^{1\times 6}$ can be expressed as follows:

$$X^{(i)} = [1, \theta^{(i)}, \dot{\theta}^{(i)}, \theta^{(i)}\dot{\theta}^{(i)}, (\theta^{(i)})^2, (\dot{\theta}^{(i)})^2] \tag{6.4}$$

The optimization problem was solved by `fmincon` solver in `MATLAB 2016b`. The initial values for the coefficient vector were all set to be one.

To compare the performance of the proposed framework with a popular classifier, an artificial neural network (ANN) was introduced to classify the loaded/unloaded muscular states. Two tests were conducted to confirm the performance of the ANN in this study. For the first test, as a conventional manner, the test data obtained in tasks (i.e., tasks (i), (ii), and (iv) in Table 6.1) were applied to Neural Pattern Recognition (`nprtool`, NN Toolbox in `MATLAB 2016b`) as *Inputs*. A two-column vector for *Targets* was defined appropriately to indicate the loaded/unloaded muscular states (i.e., S and $\neg S$). The number of hidden neurons was set to be ten. 70% of *Inputs* were used for Training, and 15% for Validation, 15% for Testing, respectively. The initial settings were utilized to set these parameters. The classification results in *TestConfusionMatrix* were shown as results in the next section.

For the other tests, training data obtained in the task (iii) were applied as *Inputs* (i.e., only the data obtained for the unloaded muscular state were provided to train the ANN). A two-column vector for *Targets* was defined to indicate all the data were obtained for the unloaded muscular state (i.e.,$\neg S$ only). The number of hidden neurons, the percentages of Training, Validation, and Testing were set as same as the first test. Additional tests with a new set of data were conducted in the evaluation phase. In this phase, test data obtained in the tasks (i), (ii) and (iv) were applied as *Inputs*. The vector for *Targets* was defined appropriately to indicate loaded/unloaded muscular states. The results in *ConfusionMatrix* were shown as results in the next section.

Accuracy, precision, recall, and F-measure were calculated based on the classification results. Based on a conventional manner, the loaded/unloaded muscular states were set as positive/negative in true condition, respectively. With this notation, precision is the proportion of the data truly positive in the data predicted as positive (i.e., the proportion of the data actually obtained in the loaded muscular state among the data classified as the loaded muscular state). Recall is the proportion of the data predicted as positive in the data truly positive (i.e., the proportion of the data classified as the loaded muscular state among the data obtained in the loaded muscular state). F-measure shows the harmonic mean of precision and recall and indicates the performance of the classification function.

Results

Validation of Experimental Data for Comparison

Fig. 6.4 shows processed experimental data of one subject. Red, yellow, magenta and green plots represent the data obtained from the task (i) to (iv) in Table 6.1, respectively. Fig. 6.4a shows the experimental result plotted in three-dimensional space (joint angle/angular velocity/sEMG) during five repetitions of the subject's elbow flexion and extension. Fig. 6.4b shows a projection of the three-dimensional space into the two-dimensional plane (joint angle/angular velocity). It can be noticed that the subject performed the motions at different frequencies as explained in Table 6.1, as each plot suggests different sizes of minor axis (i.e., magnitudes of the angular velocity) of ellipses. The other two subjects showed similar performance to the subject shown in Fig. 6.4.

Classification Results

Fig. 6.5 shows the experimental data of Fig. 6.4 with black planes which indicate different degrees of polynomial functions developed by the proposed framework. From Fig. 6.5a to Fig. 6.5d, each graph shows polynomial functions of order zero to three, respectively. Table 6.2 shows the results of mean values of the data for all three subjects, representing the cost, accuracy, precision, recall, and F-measure. The costs were calculated by (6.3a) for each function. As described in section 6.2, these black surfaces lie on all the training data (i.e., magenta) in the three-dimensional space. Note that, as a graphical interpretation, points above the black plane were classified as the loaded muscular state. Table 6.3 shows the classification results of classifiers designed by the ANN and the proposed framework. The first two-column describes the ANN trained in the first and the second tests (details in section 6.3), and the last column indicates the proposed framework (the polynomial function of degree two, Fig. 6.5c).

6.4 Discussion

Classification Performance of Proposed Framework

According to Table 6.2, the performance of the proposed framework was dependent on the degree of a polynomial function in (6.3). A polynomial of degree zero had the highest mean precision of 1.00, and all the test data obtained in the unloaded muscular states were classified correctly. This result suggests that the polynomial was equal to the maximum sEMG value observed in the training data when a degree of a polynomial function was zero. As discussed in section 6.2, the training sEMG data are assumed to be larger than testing sEMG data in unloaded muscular states. Thus, all the test data obtained in the unloaded muscular states were smaller than the polynomial (i.e., the black plane) regardless of frequencies, as shown in Fig. 6.5a. However, it misclassifies about half of the test data in the loaded states, as recall shows only 0.479.

The proposed framework developed polynomials in different orders to increase recall. It can be confirmed in Table 6.2 that increasing the degree of polynomials increased recall and decreased

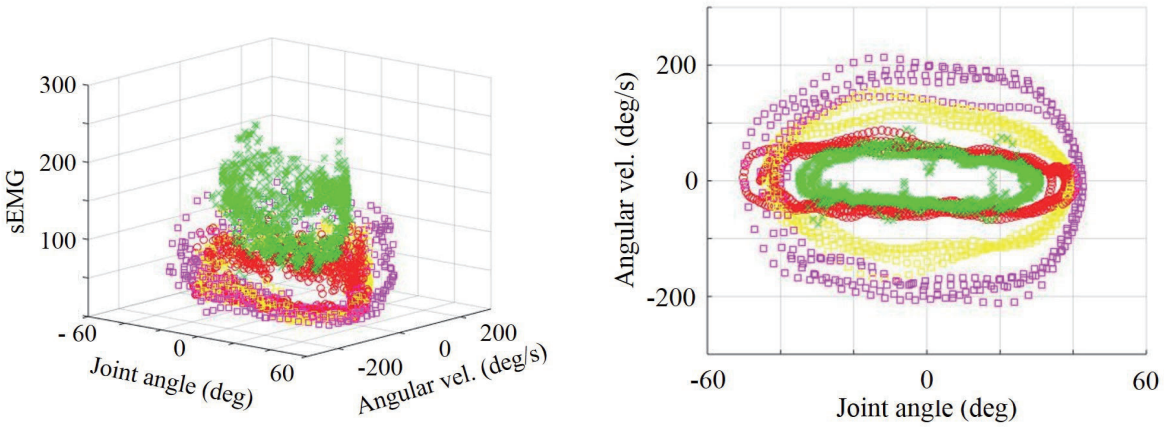

(a) In three-dimensional space.

(b) Projection of Fig. 6.4a.

Figure 6.4: Experimental relations of three features collected in all the tasks.

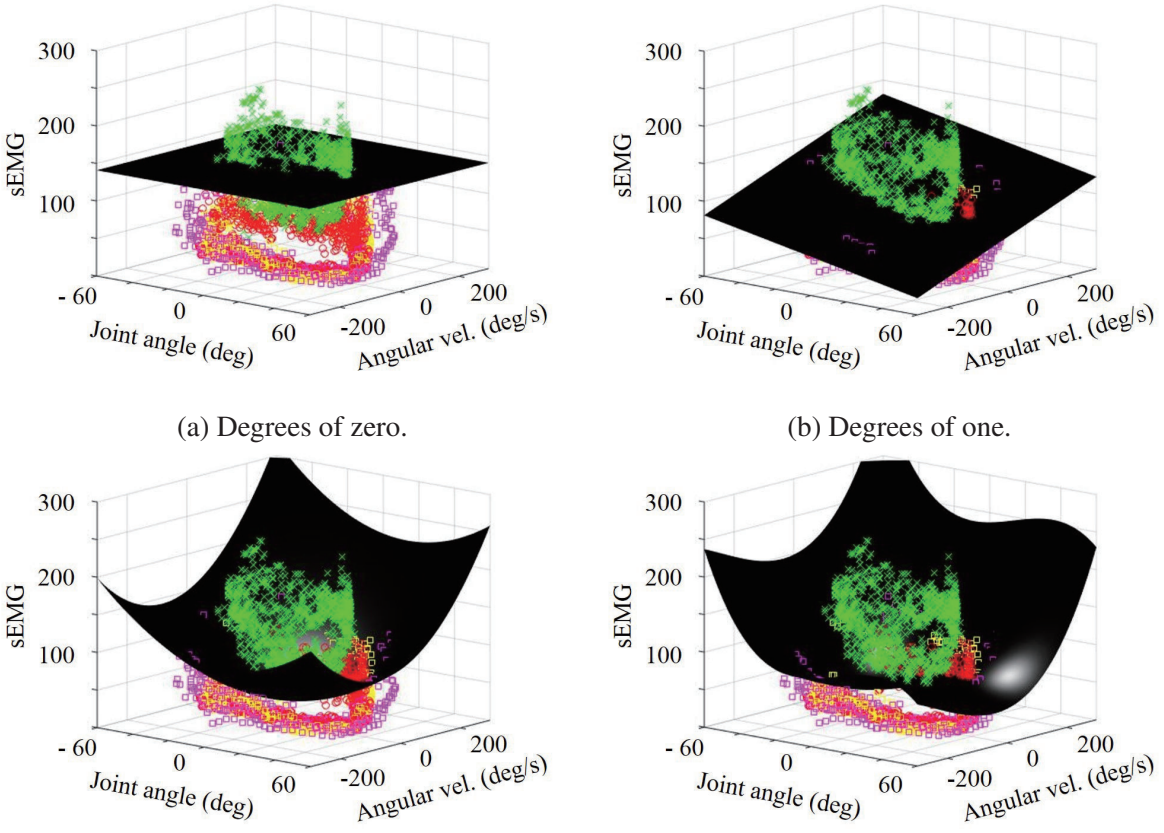

(a) Degrees of zero.

(b) Degrees of one.

(c) Degrees of two.

(d) Degrees of three.

Figure 6.5: Experimental data with different degrees of polynomial functions as thresholds.

Table 6.2: Performance of each function designed by the proposed framework

	Degree of the polynomial function			
	0	**1**	**2**	**3**
Cost	$3.52 \cdot 10^3$	$1.11 \cdot 10^3$	$8.79 \cdot 10^2$	$6.93 \cdot 10^2$
Accuracy	0.793	0.952	0.957	0.935
Precision	1.00	0.984	0.944	0.889
Recall	0.479	0.894	0.952	0.957
F-measure	0.633	0.937	0.946	0.921

Table 6.3: Comparison of performance of two algorithms

		Algorithm		
		ANN		**Proposed**
Used as Training Data	**Task (i)**	◯	×	×
	Task (ii)	◯	×	×
	Task (iii)	×	◯	◯
	Task (iv)	◯	×	×
Measure for Analysis	**Accuracy**	0.996	0.656	0.957
	Precision	1.00	0.00	0.944
	Recall	0.991	0.00	0.952
	F-measure	0.995	0.00	0.946

precision. However, a polynomial function of degree three may not necessarily be the best classifier. The reason is that F-measure, a harmonic mean of precision and recall, decreased above the degree of two. The polynomial function of degree three had the best fit to data obtained in the unloaded muscular state, as shown by the smallest mean costs in Table 6.2. Therefore, the polynomials above the degree of two were assumed to be overfitting functions to training data. Fig. 6.5 suggests visually that increasing the degree of polynomials deformed shapes of functions intricately within the ellipse composed of the training data shown in Fig. 6.4. Above all, a quadratic function had the highest mean accuracy and F-measure according to Table 6.2, and thus, the quadratic function was taken to be the optimal function for this classification problem.

Comparison with Artificial Neural Network

Table 6.3 shows the classification results of the ANN and the proposed framework. The experimental data obtained in the tasks (i), (ii), and (iv) were used as testing data to compute the results. When the ANN was trained in a conventional manner (i.e., the first column in the ANN in Ta-

ble 6.3), then the performance of the ANN was better than the proposed framework. However, the performance reversed when the number of tasks was reduced (i.e., less training data) to train the classifier designed by the ANN (i.e., the second column in the ANN in Table 6.3). The precision, recall, and F-measure of the ANN were all zero, and these figures suggest that the function was not able to predict positive at all. It suggests that all data were classified as the unloaded muscular state as there was no training data obtained in the loaded muscular state, i.e., task (iv). This result supports the known fact that the ANN requires training data which include both positive and negative data (i.e., data obtained in loaded *and* unloaded muscular states) in order to improve performance. Therefore, the proposed framework could design a better classifier compared to the ANN though less training data are available (i.e., the third column in Table 6.3).

Limitation

The number of subjects and experimental conditions were not sufficient to validate that the proposed framework can be utilized in daily living. More experiments need to be conducted over different loading conditions, motions, and individuals. The effects of muscle fatigue on the recovered classifier also need to be determined.

6.5 Summary

This chapter proposed a framework to design a classifier for assistive devices to detect assistive timing of a load-lifting task (i.e., dumbbell curls). The framework could design the binary sEMG classifier, which required fewer tasks to collect its training data compared to an artificial neural network (ANN). The proposed framework developed a polynomial function that lay on top of the training data collected in the unloaded muscular state at the highest frequency.

The performance of the framework was validated through experiments. A quadratic polynomial was found to be optimal among the other three different polynomials developed by the proposed framework. The proposed framework could design the classifier with the optimal polynomial, which achieved a high accuracy (i.e., 95.7%) with fewer number of tasks to train the classifiers. The performance of the optimized classifier was compared with the ANN which was trained with data obtained from several tasks. The results suggested that the classifier was found to be comparable to the ANN in this problem (i.e., 95.7% and 99.6%). From the above, the proposed framework may be useful for assistive devices to detect the assistive timing while reducing the efforts of the users.

Chapter 7

Conclusion

7.1 Concluding Remarks

This dissertation investigated technical issues in the development of intelligent assistive devices for daily living. Demands for the devices and state-of-the-art technologies in the related field were discussed in chapter 1, where the assistive devices were modeled as the Cyber-Physical-Systems (CPS). One of the limitations of the CPS model was the disregard of energy efficiency, which is a critical issue in the development of assistive devices for daily living. To address this issue, literature reviews were conducted from the viewpoint of three main components of the CPS model; actuators, controllers, and sensors with estimators. This dissertation contributed to improving three components in the development of energy-efficient, assistive devices.

Design and Control of Variable Stiffness Actuators with Pneumatic Systems

Chapter 2 introduced an Active/Passive Pneumatic Actuator (AP2A) whose stiffness (i.e., mechanical impedance) can be actively modified according to the desired values[1]. Several actuators, such as series elastic actuators and pneumatic actuators, have been investigated for effective physical human-robot interaction. These actuators can modify their mechanical characteristics at the expense of energy from external power sources (e.g., electrical batteries). Passive components, such as springs and elastic bands, do not require any energy. However, their mechanical characteristics are not able to change without manual replacements. The AP2A has advantages of both active and passive components, which consists of an air cylinder and an array of solenoid valves. The AP2A neither assists nor disturbs external forces applied to a rod when both chambers are open to the atmosphere (i.e., the *no-assist* mode in Fig. 3.2). A reaction force produced by the cylinder can be modified by sealing chambers with valves after tuning air pressures. Once the chambers are sealed, the cylinder reacts to the external forces passively as a mechanical spring without any energy consumption (i.e., the *assist* mode in Fig. 1.10 or the *passive* mode in Fig. 3.2).

[1]These works were published in [105, 106].

Chapter 2 introduced two controllers that utilize these characteristics of the AP2A. Experimental results suggest that the model-based, switching controller enabled the AP2A to function as a mechanical spring with desired stiffness and equilibrium. A model-free controller was investigated in parallel with the model-base controller to modify the stiffness and equilibrium without the identification of complex, nonlinear models of the air mass flow. Thus, this dissertation contributed to characterizing the AP2A that can modify its mechanical characteristics with less energy consumption.

Control Strategies for Variable Stiffness Actuators

Chapter 3 introduced a high-level controller which outputs the desired stiffness and equilibrium (i.e., desired chamber pressures) of the AP2A as a reference[2]. Most of the controllers developed in prior work focus on assistance under a specific condition (e.g., gait assistance). A control framework proposed in Fig. 1.10 has the potential to handle multiple tasks carried out in daily activities. This framework is applied to the AP2A, as the low-level controller can handle both *no-assist* and *assist* modes with the valves. This dissertation investigated the *assist* mode for a load-lifting task (e.g., dumbbell curls). Optimal control problems were formulated in chapters 3, 4, and 5, searching for a reference that is optimized for the task in terms of the energy efficiency while maintaining task performance.

In chapter 3, a simulation study was conducted with a numerical model of a pendulum with a load to evaluate the performance of references obtained as the solutions to the optimal control problem. A cost function of the problem included energy consumed by the AP2A (i.e., amount of supply air) and the pendulum (i.e., a joint torque produced by a motor) with weighting factors. When the cost of the pendulum had a significant weighting factor, the controller designed a reference that reduced the motor torque by tuning pressures *actively* at the expense of the supply air. On the other hand, the controller designed a reference that tuned the AP2A to assist the pendulum *passively* with less energy consumption when the cost of the AP2A had a significant weighting factor. From the simulation results, this dissertation contributed to developing a control structure of the AP2A to balance the competing goals of minimizing the energy consumption of the AP2A while maximizing the assistance.

The performance of passive assistance was further investigated with the pendulum and an exoskeleton in chapters 4 and 5. Chapter 4 described experiments with the pendulum, which is generally concise and straightforward to model and analyze the performance of the whole system compared to the system including human subjects. Chapter 5 introduced an Active/Passive EXoskeleton-α (APEX-α), which utilized the AP2A [74]. Experimental results obtained in prior work [74, 110] were reexamined along with numerical analysis based on chapter 3. These experimental results and analysis indicated that the reference designed for passive assistance could improve the energy efficiency of the AP2A as well as the task performance of the pendulum and

[2]These works were published in [107, 108].

the human subjects. Thus, this dissertation contributed to validating performance of the controller of the AP2A in application to the pendulum and the APEX-α.

A Task Classifier for Assistive Timing Detection

Chapter 6 introduced a framework to design a classifier for assistive devices to detect changes in users' behavior for assistive timing[3]. When the assistive devices with the high-level controller in Fig. 1.10 are utilized in daily life, the controller requires guards G which enable transitions from *no-assist* to *assist* mode and vice versa. In other words, the control framework needs an estimator (i.e., a classifier) to detect assistive timing from sensory feedback signals.

Several estimators have been investigated with machine learning (ML) algorithms. These algorithms with signal processing techniques make assistive devices recognize and classify patterns of physiological signals (e.g., surface electromyography). These ML algorithms require training data obtained through several procedures to improve the performance of the classifier. Chapter 6 introduced a framework that reduces the number of procedures to develop the classifier without degradation of the performance. Experiments were conducted to validate the performance of two classifiers that were developed by the proposed framework and the artificial neural network. The experimental results suggested that the performance of the classifiers was found to be equivalent to each other. Thus, this dissertation contributed to developing an estimator as guards of the high-level controller.

7.2 Open Issues

As discussed above, this dissertation made a significant contribution to the development of intelligent assistive devices. However, there are several open issues. A few of them are discussed in the following paragraphs.

Analysis of Active Assistance

A simulation study in Chapter 3 indicated that the high-level controller could design a reference for passive assistance to save energy of the AP2A (e.g., Fig. 3.8 and 3.9). The performance of the passive assistance was further investigated in experiments, as described in chapters 4 and 5. In chapter 3, the high-level controller could also generate a reference for active assistance (e.g., Fig. 3.10), which reduced a motor torque by tuning pressures actively at the expense of supply air. Since active assistance utilized all the chances (i.e., $N = 4$ in the simulation study) to switch the modes, chamber pressures were modified three times, as shown in Fig. 3.10b. When the number of switching times is increased, the reference may differ from the result shown in Fig. 3.10. Further simulation analysis, as well as experimental validations, are required to validate the performance of active assistance.

[3]This work was published in [109].

Increase of the Number of Assist Modes

The performance of the high-level controller was evaluated under limited experimental conditions. Two discrete modes (i.e., *no-assist* and *assist* modes) were considered in this dissertation as shown in Fig. 1.10. In particular, a task in the *assist* mode was set to be a repetitive load manipulation such as dumbbell curls. As stated above, the proposed framework in Fig. 1.10 has the potential to handle multiple tasks. The number of tasks (i.e., *assist* modes) needs to be increased to develop intelligent assistive devices for daily living. In each task, experiments are required to validate the performance of an augmented high-level controller with several indexes, which can estimate the energy consumption or the metabolic cost, such as maximal oxygen consumption (VO_2max).

Validation with Human Subjects

In chapter 5, the performance of the high-level controller was confirmed with young, healthy subjects (aged 23 ± 3 years) by reexamining experimental results from prior work [74, 110]. These results suggested that the control framework and the assistive device with the AP2A (i.e., an Active/Passive EXoskeleton-α) may be useful in workplaces such as assembly lines to remedy muscular fatigue or to prevent injuries during load-lifting tasks. However, further experiments need to be conducted with the elderly and people with disabilities in order to proof the performance as assistive devices. Human modeling techniques also need to be investigated in parallel with these experiments, which represent the physical abilities of individuals. The human models can be implemented as constraints of the optimal control problem to prescribe assistive devices that are suitable for each individual.

Bibliography

[1] Quanhe Yang et al. “Vital Signs: Recent Trends in Stroke Death Rates — United States, 2000–2015”. In: *MMWR Morb Mortal Wkly Rep* 66 (2017), pp. 933–939.

[2] Benjamin EJ et al. “Heart disease and stroke statistics—2017 update: a report from the American Heart Association”. In: *Circulation* 135 (2017), pp. 229–445.

[3] National Spinal Cord Injury Statistical Center (NSCISC). *Spinal Cord Injury Facts and Figures at a Glance*. retrieved: June 2019. URL: https://www.nscisc.uab.edu/Public/Facts%20and%20Figures%20-%202018.pdf.

[4] US Census Bureau. May 2019, retrieved. URL: https://www.census.gov/.

[5] Ministry of internal affairs and communications. *WHITE PAPER Information and Communications in Japan*. May 2019, retrieved. URL: http://www.soumu.go.jp/johotsusintokei/whitepaper/ja/h28/html/nc111110.html.

[6] H.F. Machiel Van der Loos and David J. Reinkensmeyer. “Rehabilitation and Health Care Robotics”. In: *Springer Handbook of Robotics*. Ed. by Bruno Siciliano and Oussama Khatib. Berlin, Heidelberg: Springer Berlin Heidelberg, 2008, pp. 1223–1251. ISBN: 978-3-540-30301-5. DOI: 10.1007/978-3-540-30301-5_54. URL: https://doi.org/10.1007/978-3-540-30301-5_54.

[7] Ford Motor Company. *FORD PILOTS NEW EXOSKELETON TECHNOLOGY TO HELP LESSEN CHANCE OF WORKER FATIGUE, INJURY*. 2017 (retrieved: Aug. 2019). URL: https://media.ford.com/content/fordmedia/fna/us/en/news/2017/11/09/ford-exoskeleton-technology-pilot.html.

[8] Hyundai. *Hyundai Motor Group Ventures Further Into New Robotics Industry*. 2018 (retrieved: Aug. 2019). URL: https://www.hyundai.news/uk/brand/hyundai-motor-group-ventures-further-into-new-robotics-industry/.

[9] Homayoon Kazerooni. “Exoskeletons for Human Performance Augmentation”. In: *Springer Handbook of Robotics*. Ed. by Bruno Siciliano and Oussama Khatib. Berlin, Heidelberg: Springer Berlin Heidelberg, 2008, pp. 773–793. ISBN: 978-3-540-30301-5. DOI: 10.1007/978-3-540-30301-5_34. URL: https://doi.org/10.1007/978-3-540-30301-5_34.

[10] N. Hogan et al. “MIT-MANUS: a workstation for manual therapy and training. I”. In: *Proceedings IEEE International Workshop on Robot and Human Communication*. 1992, pp. 161–165. DOI: 10.1109/ROMAN.1992.253895.

[11] Krebs HI et al. “Robot-aided neurorehabilitation”. In: *IEEE Trans Rehabil Eng.* 6.1 (1998), pp. 75–87.

[12] Colombo G et al. “Treadmill training of paraplegic patients using a robotic orthosis”. In: *J Rehabil Res Dev.* 37.6 (2000), pp. 693–700.

[13] Krebs HI et al. “Increasing productivity and quality of care: robot-aided neuro-rehabilitation”. In: *J Rehabil Res Dev.* 37.6 (2000), pp. 639–652.

[14] Prange GB et al. “Systematic review of the effect of robot-aided therapy on recovery of the hemiparetic arm after stroke”. In: *J Rehabil Res Dev.* 43.2 (2006), pp. 171–184.

[15] Eva Swinnen et al. “Effectiveness of Robot Assisted Gait Training in Persons with Spinal Cord Injury: A Systematic Review”. In: *Journal of Rehabilitation Medicine* 42.6 (2010), pp. 520–526. DOI: doi:10.2340/16501977-0538.

[16] Jan Mehrholz and Marcus Pohl. “Electromechanical-assisted gait training after stroke: A systematic review comparing end-effector and exoskeleton devices”. In: *J Rehabil Med* 44.3 (2012), pp. 193–199. DOI: 10.2340/16501977-0943.

[17] Edward A Lee and Sanjit A. Seshia. *Introduction to Embedded Systems, A Cyber-Physical Systems Approach*. MIT Press, 2017. ISBN: 978-0-262-53381-2.

[18] Wenlong Zhang. “Design and Control of a Network-based Gait Rehabilitation System: A Cyber-Physical System Approach”. PhD thesis. ME Department, University of California, Berkeley, May 2015.

[19] S. K. Au, J. Weber, and H. Herr. “Biomechanical Design of a Powered Ankle-Foot Prosthesis”. In: *2007 IEEE 10th International Conference on Rehabilitation Robotics*. June 2007, pp. 298–303. DOI: 10.1109/ICORR.2007.4428441.

[20] Exact Dynamics BV. *Product Overview*. 2012 (retrieved: Aug. 2019). URL: http://iarmrobot.com/overview.shtml.

[21] E. A. Lee, A. L. Sangiovanni-Vincentelli, and S. A. Seshia. *EECS 149/249A Lecture Notes*. retrieved: Aug. 2019. URL: https://ptolemy.berkeley.edu/projects/chess/eecs149/lectures/index.html.

[22] Joan Lobo-Prat et al. “Non-invasive control interfaces for intention detection in active movement-assistive devices”. In: *J. of NeuroEngineering and Rehabilitation* 11.1 (Dec. 2014), p. 168. ISSN: 1743-0003. DOI: 10.1186/1743-0003-11-168. URL: https://doi.org/10.1186/1743-0003-11-168.

[23] Masayoshi Tomizuka. *Advance Control Systes I: Class Notes for ME C232/EE C220A*. 2014.

[24] B. W. Gasser et al. “Design and preliminary assessment of Vanderbilt hand exoskeleton”. In: *Proc. IEEE Int. Conf. on Rehabilitation Robotics (ICORR)*. July 2017, pp. 1537–1542. DOI: 10.1109/ICORR.2017.8009466.

[25] Y. Matsumoto, T. Ino, and T. Ogsawara. “Development of intelligent wheelchair system with face and gaze based interface”. In: *Proceedings 10th IEEE International Workshop on Robot and Human Interactive Communication. ROMAN 2001 (Cat. No.01TH8591)*. Sept. 2001, pp. 262–267. DOI: 10.1109/ROMAN.2001.981912.

[26] Gabriel Pires and Urbano Nunes. “A Wheelchair Steered through Voice Commands and Assisted by a Reactive Fuzzy-Logic Controller”. In: *Journal of Intelligent and Robotic Systems* 34.3 (July 2002), pp. 301–314. ISSN: 1573-0409.

[27] S. R. Soekadar et al. “Hybrid EEG/EOG-based brain/neural hand exoskeleton restores fully independent daily living activities after quadriplegia”. In: *Science Robotics* 1.1 (2016). DOI: 10.1126/scirobotics.aag3296.

[28] S. Miura et al. “Using Brain Activation to Evaluate Arrangements Aiding Hand–Eye Coordination in Surgical Robot Systems”. In: *IEEE Transactions on Biomedical Engineering* 66.8 (Aug. 2019), pp. 2352–2361. ISSN: 0018-9294. DOI: 10.1109/TBME.2018.2889316.

[29] T. Ando, M. Watanabe, and M. G. Fujie. “Extraction of voluntary movement for an EMG controlled exoskeltal robot of tremor patients”. In: *2009 4th International IEEE/EMBS Conference on Neural Engineering*. Apr. 2009, pp. 120–123. DOI: 10.1109/NER.2009.5109249.

[30] Kyoungchul Kong and Masayoshi Tomizuka. “Control of exoskeletons inspired by fictitious gain in human model”. In: *IEEE/ASME Trans. on Mechatronics* 14.6 (2009), pp. 689–698.

[31] H. Kazerooni et al. “On the Control of the Berkeley Lower Extremity Exoskeleton (BLEEX)”. In: *Proc. IEEE Int. Conf. on Robotics and Automation (ICRA)*. Apr. 2005, pp. 4353–4360. DOI: 10.1109/ROBOT.2005.1570790.

[32] R. Robert Rosenberg and Dean C. Karnopp. *Introduction to Physical System Dynamics*. 1st. New York, NY, USA: McGraw-Hill, Inc., 1983. ISBN: 0070539057.

[33] Cyberdyne. *HAL FOR WELL-BEING (SINGLE JOINT TYPE)*. retrieved: Aug. 2019. URL: https://www.cyberdyne.jp/english/products/SingleJoint.html.

[34] ATOUN. *ATOUN MODEL Y*. retrieved: Aug. 2019. URL: http://atoun.co.jp/products/atoun-model-y.

[35] Haoyong Yu et al. “Control design of a novel compliant actuator for rehabilitation robots”. In: *Mechatronics* 23.8 (2013), pp. 1072–1083. ISSN: 0957-4158. DOI: https://doi.org/10.1016/j.mechatronics.2013.08.004. URL: http://www.sciencedirect.com/science/article/pii/S0957415813001542.

[36] Vincent Duindam et al. *Modeling and Control of Complex Physical Systems: The Port-Hamiltonian Approach*. Springer, Berlin, Heidelberg, 2009. ISBN: 978-3-642-03195-3.

[37] Koichi Osuka. *Chinou ha Dokokara Umarerunoka? Mukaderobotto to Sagasu "Kakureta Nou" (Author's translation: How dose intelligence arise from nothing? Consideration of Secrets of Brains using a Centipede Robot)*. Kindaikagaku, 2018, (written in Japanese). ISBN: 978-4-7649-0581-8 C3050.

[38] B. Vanderborght et al. "A strategy to combine active trajectory control with the exploitation of the natural dynamics to reduce energy consumption for bipedal robots". In: *2007 7th IEEE-RAS International Conference on Humanoid Robots*. Nov. 2007, pp. 7–12. DOI: 10.1109/ICHR.2007.4813842.

[39] A. Velasco et al. "Soft-actuators in cyclic motion: Analytical optimization of stiffness and pre-load". In: *2013 13th IEEE-RAS International Conference on Humanoid Robots (Humanoids)*. Oct. 2013, pp. 354–361. DOI: 10.1109/HUMANOIDS.2013.7029999.

[40] S. Srivastava et al. "Assist-as-Needed Robot-Aided Gait Training Improves Walking Function in Individuals Following Stroke". In: *IEEE Transactions on Neural Systems and Rehabilitation Engineering* 23.6 (Nov. 2015), pp. 956–963. ISSN: 1534-4320. DOI: 10.1109/TNSRE.2014.2360822.

[41] S. Hashimoto et al. "Humanoid Robots in Waseda University—Hadaly-2 and WABIAN". In: *Autonomous Robots* 12.1 (Jan. 2002), pp. 25–38. ISSN: 1573-7527. DOI: 10.1023/A:1013202723953. URL: https://doi.org/10.1023/A:1013202723953.

[42] Tad McGeer. "Passive Dynamic Walking". In: *The International Journal of Robotics Research* 9, 2 (1990), pp. 62–82.

[43] Steve Collins et al. "Efficient Bipedal Robots Based on Passive-Dynamic Walkers". In: *Science* 307.5712 (2005), pp. 1082–1085. ISSN: 0036-8075. DOI: 10.1126/science.1107799. eprint: https://science.sciencemag.org/content/307/5712/1082.full.pdf.

[44] Jacquelin Perry and Judith Burnfield. *Gait Analysis: Normal and Pathological Function*. Slack Incorporated, 2010. ISBN: 978-1556427664.

[45] K. Endo, D. Paluska, and H. Herr. "A quasi-passive model of human leg function in level-ground walking". In: *2006 IEEE/RSJ International Conference on Intelligent Robots and Systems*. Oct. 2006, pp. 4935–4939. DOI: 10.1109/IROS.2006.282454.

[46] R. Riener et al. "Patient-cooperative strategies for robot-aided treadmill training: first experimental results". In: *IEEE Transactions on Neural Systems and Rehabilitation Engineering* 13.3 (Sept. 2005), pp. 380–394. ISSN: 1534-4320. DOI: 10.1109/TNSRE.2005.848628.

[47] A. Duschau-Wicke et al. "Path Control: A Method for Patient-Cooperative Robot-Aided Gait Rehabilitation". In: *IEEE Transactions on Neural Systems and Rehabilitation Engineering* 18.1 (Feb. 2010), pp. 38–48. ISSN: 1534-4320. DOI: 10.1109/TNSRE.2009.2033061.

[48] H. J. Asl, T. Narikiyo, and M. Kawanishi. "An Assist-as-Needed Velocity Field Control Scheme for Rehabilitation Robots". In: *2018 IEEE/RSJ International Conference on Intelligent Robots and Systems (IROS)*. Oct. 2018, pp. 3322–3327. DOI: 10.1109/IROS.2018.8594244.

[49] S. K. Banala, S. K. Agrawal, and J. P. Scholz. "Active Leg Exoskeleton (ALEX) for Gait Rehabilitation of Motor-Impaired Patients". In: *2007 IEEE 10th International Conference on Rehabilitation Robotics*. June 2007, pp. 401–407. DOI: 10.1109/ICORR.2007.4428456.

[50] Conor James Walsh, Ken Endo, and Hugh Herr. "A quasi-passive leg exoskeleton for load-carrying augmentation". In: *International Journal of Humanoid Robotics* 4.3 (2007), pp. 487–506. DOI: 10.1142/S0219843607001126. eprint: https://doi.org/10.1142/S0219843607001126. URL: https://doi.org/10.1142/S0219843607001126.

[51] S. H. Collins, M. B. Wiggin, and G. S. Sawicki. "Reducing the energy cost of human walking using an unpowered exoskeleton". In: *Nature* 522.212 (Apr. 2015), pp. 1786–1793. ISSN: 1070-9932. DOI: 0.1038/nature14288.

[52] Charles L. Phillips and Royce D. Harbor. *Feedback Control Systems*. Prentice Hall; 4th edition, 2000. ISBN: 978-0139490903.

[53] Koh Hosoda. *Yawaraka Humanoids: Robot ga Chinou no Nazo wo Tokiakasu (Author's translation: Soft Humanoid Robotics - a study on intelligence with humanoid robots)*. Kagakudoujin, 2016, (written in Japanese). ISBN: 9784759816709.

[54] Gill A Pratt and Matthew M Williamson. "Series elastic actuators". In: *Proc. IEEE/RSJ Int. Conf. on Intelligent Robots and Systems (IROS)*. 1995, pp. 399–406.

[55] Kyoungchul Kong, J. Bae, and Masayoshi Tomizuka. "Control of Rotary Series Elastic Actuator for Ideal Force-Mode Actuation in Human–Robot Interaction Applications". In: *IEEE/ASME Trans. on Mechatronics* 14.1 (2009), pp. 105–118.

[56] J. F. Veneman et al. "Design and Evaluation of the LOPES Exoskeleton Robot for Interactive Gait Rehabilitation". In: *IEEE Trans. on Neural Systems and Rehabilitation Engineering* 15.3 (Sept. 2007), pp. 379–386. ISSN: 1534-4320. DOI: 10.1109/TNSRE.2007.903919.

[57] Junkai Lu et al. "Design and torque-mode control of a cable-driven rotary series elastic actuator for subject-robot interaction". In: *Proc. IEEE Int. Conf. on Advanced Intelligent Mechatronics (AIM)*. 2015, pp. 158–164.

[58] R. V. Ham et al. "Compliant actuator designs". In: *IEEE Robotics Automation Magazine* 16.3 (Sept. 2009), pp. 81–94. ISSN: 1070-9932. DOI: 10.1109/MRA.2009.933629.

[59] B. Vanderborght et al. "Variable impedance actuators: A review". In: *Robotics and Autonomous Systems* 61.12 (2013), pp. 1601–1614. ISSN: 0921-8890. DOI: https://doi.org/10.1016/j.robot.2013.06.009. URL: http://www.sciencedirect.com/science/article/pii/S0921889013001188.

[60] A. Toedtheide, T. Lilge, and S. Haddadin. "Antagonistic Impedance Control for Pneumatically Actuated Robot Joints". In: *IEEE Robotics and Automation Letters* 1.1 (Jan. 2016), pp. 161–168. ISSN: 2377-3766. DOI: 10.1109/LRA.2015.2511663.

[61] G. Tonietti, R. Schiavi, and A. Bicchi. "Design and Control of a Variable Stiffness Actuator for Safe and Fast Physical Human/Robot Interaction". In: *Proc. IEEE Int. Conf. on Robotics and Automation (ICRA)*. 2005, pp. 526–531. DOI: 10.1109/ROBOT.2005.1570172.

[62] Jun Zhu et al. "Unidirectional variable stiffness hydraulic actuator for load-carrying knee exoskeleton". In: *International Journal of Advanced Robotic Systems* 14.1 (2017). DOI: 10.1177/1729881416686955.

[63] J. Wang et al. "Comfort-Centered Design of a Lightweight and Backdrivable Knee Exoskeleton". In: *IEEE Robotics and Automation Letters* 3.4 (Oct. 2018), pp. 4265–4272. ISSN: 2377-3766. DOI: 10.1109/LRA.2018.2864352.

[64] H. Zhu et al. "Design and Validation of a Partial-Assist Knee Orthosis with Compact, Backdrivable Actuation". In: *2019 IEEE 16th International Conference on Rehabilitation Robotics (ICORR)*. June 2019, pp. 917–924. DOI: 10.1109/ICORR.2019.8779479.

[65] Panagiotis Polygerinos et al. "Soft robotic glove for combined assistance and at-home rehabilitation". In: *Robotics and Autonomous Systems* 73 (2015), pp. 135–143. ISSN: 0921-8890. DOI: https://doi.org/10.1016/j.robot.2014.08.014.

[66] Yasmin Ansari et al. "Towards the development of a soft manipulator as an assistive robot for personal care of elderly people". In: *Int. J. of Advanced Robotic Systems* 14.2 (2017), pp. 1–17. DOI: 10.1177/1729881416687132.

[67] Nelson Costa et al. "Joint motion control of a powered lower limb orthosis for rehabilitation". In: *Int. J. of Automation and Computing* 3.3 (July 2006), pp. 271–281. ISSN: 1751-8520. DOI: 10.1007/s11633-006-0271-x.

[68] T. Abe et al. "Muscle textile to implement soft suit to shift balancing posture of the body". In: *Proc. IEEE/RSJ Int. Conf. on Soft Robotics (RoboSoft)*. 2018, pp. 572–578. DOI: 10.1109/ROBOSOFT.2018.8405387.

[69] Xiangrong Shen and Michael Goldfarb. "Simultaneous force and stiffness control of a pneumatic actuator". In: *J. of Dynamic Systems, Measurement, and Control* 129.4 (2007), pp. 425–434.

[70] Behzad Taheri, David Case, and Edmond Richer. "Force and stiffness backstepping-sliding mode controller for pneumatic cylinders". In: *IEEE/ASME Trans. on Mechatronics* 19.6 (2014), pp. 1799–1809.

[71] Tariq Rahman et al. "Passive exoskeletons for assisting limb movement". In: *J. of rehabilitation research and development* 43.5 (2006), p. 583.

[72] S. Diller, C. Majidi, and S. H. Collins. “A lightweight, low-power electroadhesive clutch and spring for exoskeleton actuation”. In: *Proc. IEEE Int. Conf. on Robotics and Automation (ICRA)*. 2016, pp. 682–689. DOI: 10.1109/ICRA.2016.7487194.

[73] H. Herr and A. Wilkenfeld. “User-adaptive control of a magnetorheological prosthetic knee”. In: *Industrial Robot* 30.1 (2003), pp. 42–55.

[74] R. P. Matthew et al. “Introduction and initial exploration of an Active/Passive Exoskeleton framework for portable assistance”. In: *Proc. IEEE/RSJ Int. Conf. on Intelligent Robots and Systems (IROS)*. 2015, pp. 5351–5356. DOI: 10.1109/IROS.2015.7354133.

[75] Robert Matthew. “Better, Faster, Stronger: Measuring and Transcending Your Physical Limits with Wearable Robots”. PhD thesis. EECS Department, University of California, Berkeley, Dec. 2018.

[76] B. K. Dinh et al. “Hierarchical Cascade Controller for Assistance Modulation in a Soft Wearable Arm Exoskeleton”. In: *IEEE Robotics and Automation Letters* 2.3 (July 2017), pp. 1786–1793. ISSN: 2377-3766. DOI: 10.1109/LRA.2017.2668473.

[77] Hiroaki Kawamoto and Yoshiyuki Sankai. “EMG-based Hybrid Assistive Leg for Walking Aid using Feedforward Controller”. In: *Proc. of IEEE International Conference on Control, Automation and System (ICCAS)*. 2001, pp. 190–193.

[78] Neville Hogan. “Impedance control: An approach to manipulation: Part II Implementation”. In: *J. of Dynamic Systems, Measurement, and Control* 107.1 (1985), pp. 8–16.

[79] S. Lee and Y. Sankai. “Power assist control for walking aid with HAL-3 based on EMG and impedance adjustment around knee joint”. In: *IEEE/RSJ International Conference on Intelligent Robots and Systems*. Vol. 2. Sept. 2002, 1499–1504 vol.2. DOI: 10.1109/IRDS.2002.1043967.

[80] E. T. Wolbrecht et al. “Control of a Pneumatic Orthosis for Upper Extremity Stroke Rehabilitation”. In: *Proc. Int. Conf. of the IEEE Engineering in Medicine and Biology Society (EMBC)*. Aug. 2006, pp. 2687–2693. DOI: 10.1109/IEMBS.2006.259941.

[81] S. K. Banala et al. “Robot Assisted Gait Training With Active Leg Exoskeleton (ALEX)”. In: *IEEE Transactions on Neural Systems and Rehabilitation Engineering* 17.1 (Feb. 2009), pp. 2–8. ISSN: 1534-4320. DOI: 10.1109/TNSRE.2008.2008280.

[82] Xiang Li et al. “Multi-modal control scheme for rehabilitation robotic exoskeletons”. In: *The International Journal of Robotics Research* 36.5-7 (2017), pp. 759–777. DOI: 10.1177/0278364917691111.

[83] R. Ronsse et al. “Adaptive oscillators with human-in-the-loop: Proof of concept for assistance and rehabilitation”. In: *2010 3rd IEEE RAS EMBS International Conference on Biomedical Robotics and Biomechatronics*. Sept. 2010, pp. 668–674. DOI: 10.1109/BIOROB.2010.5628021.

[84] X. Zhang and M. Hashimoto. "SBC for motion assist using neural oscillator". In: *2009 IEEE International Conference on Robotics and Automation*. May 2009, pp. 659–664. DOI: 10.1109/ROBOT.2009.5152411.

[85] Y. Ding et al. "Estimating wrist joint angle with limited skin deformation information". In: *Science Robotics* 3.15 (2018). DOI: 10.1299/jbse.17-00596.

[86] J. R. Koller et al. "'Body-in-the-Loop' Optimization of Assistive Robotic Devices: A Validation Study". In: *Robotics: Science and Systems (RSS)*. 2016.

[87] Juanjuan Zhang et al. "Human-in-the-loop optimization of exoskeleton assistance during walking". In: 356.6344 (2017), pp. 1280–1284. ISSN: 0036-8075. DOI: 10.1126/science.aal5054. eprint: http://science.sciencemag.org/content/356/6344/1280.full.pdf.

[88] D. Ben-Dov and S. E. Salcudean. "A force-controlled pneumatic actuator". In: *IEEE Transactions on Robotics and Automation* 11.6 (Dec. 1995), pp. 906–911. ISSN: 1042-296X. DOI: 10.1109/70.478438.

[89] E. Richer and Y. Hurmuzlu. "A High Performance Pneumatic Force Actuator System: Part-I Nonlinear Mathematical Model". In: *J. of Dynamic Systems, Measurement, and Control* 122.3 (1999), pp. 416–425. DOI: 10.1115/1.1286336.

[90] I. Kato. "Trends in powered upper limb prostheses". In: *Prosthetics and Orthotics International* 2.2 (1978). PMID: 214752, pp. 64–68. DOI: 10.1080/03093647809177769. eprint: https://doi.org/10.1080/03093647809177769. URL: https://doi.org/10.1080/03093647809177769.

[91] M. Zecca et al. "Control of Mutifunctional Prosthetic Hands by Processing the Electromyographic Signal". In: *Critical Reviews and Trade; in Biomedical Eng.* 30.4-6 (2002), pp. 459–485. ISSN: 0278-940X.

[92] P. Parker, K. Englehart, and B. Hudgins. "Myoelectric signal processing for control of powered limb prostheses". In: *Journal of Electromyography and Kinesiology* 16.6 (2006). Special Section (pp. 541–610): 2006 ISEK Congress, pp. 541–548. ISSN: 1050-6411. DOI: https://doi.org/10.1016/j.jelekin.2006.08.006. URL: http://www.sciencedirect.com/science/article/pii/S1050641106001027.

[93] Ortiz-Catalan M., Brånemark R., and Håkansson B. "BioPatRec: A modular research platform for the control of artificial limbs based on pattern recognition algorithms." In: *Source Code Biol Med.* 8.11 (2013). DOI: doi:10.1186/1751-0473-8-11.

[94] Weidong Geng et al. "Gesture recognition by instantaneous surface EMG images". In: *Scientific Reports* 16 (Nov. 2016). DOI: https://doi.org/10.1038/srep36571.

[95] P. M. Pilarski et al. "Online human training of a myoelectric prosthesis controller via actor-critic reinforcement learning". In: *2011 IEEE International Conference on Rehabilitation Robotics*. June 2011, pp. 1–7. DOI: 10.1109/ICORR.2011.5975338.

[96] Jacob Rosen, Moshe B. Fuchs, and Mircea Arcan. "Performances of Hill-Type and Neural Network Muscle Models—Toward a Myosignal-Based Exoskeleton". In: *Computers and Biomedical Research* 32.5 (1999), pp. 415–439. ISSN: 0010-4809. DOI: https://doi.org/10.1006/cbmr.1999.1524. URL: http://www.sciencedirect.com/science/article/pii/S0010480999915240.

[97] Y. Yun et al. "Maestro: An EMG-driven assistive hand exoskeleton for spinal cord injury patients". In: *Proc. IEEE Int. Conf. on Robotics and Automation (ICRA)*. May 2017, pp. 2904–2910. DOI: 10.1109/ICRA.2017.7989337.

[98] Hill Archibald Vivian. "The heat of shortening and the dynamic constants of muscle". In: *Proc. R. Soc. Lond. B* 126 (1938 (published online: 1997)), pp. 136–195. DOI: https://doi.org/10.1098/rspb.1938.0050.

[99] F. E. Zajac. "Muscle and tendon: properties, models, scaling, and application to biomechanics and motor control". In: *Crit Rev Biomed Eng.* 17.4 (1989), pp. 359–411.

[100] D. G. Thelen. "Adjustment of Muscle Mechanics Model Parameters to Simulate Dynamic Contractions in Older Adults". In: *ASME. J Biomech Eng* 125.1 (2003), pp. 70–77. DOI: 10.1115/1.1531112.

[101] Michael Damsgaard et al. "Analysis of musculoskeletal systems in the AnyBody Modeling System". In: *Simulation Modelling Practice and Theory* 14.8 (2006). SIMS 2004, pp. 1100–1111. ISSN: 1569-190X. DOI: https://doi.org/10.1016/j.simpat.2006.09.001. URL: http://www.sciencedirect.com/science/article/pii/S1569190X06000554.

[102] S. L. Delp et al. "Passive exoskeletons for assisting limb movement". In: *IEEE Trans. on Biomedical Eng.* 54.11 (2007), pp. 1940–1950.

[103] Ahmet Erdemir et al. "Model-based estimation of muscle forces exerted during movements". In: *Clinical Biomechanics* 22.2 (2007), pp. 131–154. ISSN: 0268-0033.

[104] C. Fleischer, C. Reinicke, and G. Hommel. "Predicting the intended motion with EMG signals for an exoskeleton orthosis controller". In: *2005 IEEE/RSJ International Conference on Intelligent Robots and Systems*. Aug. 2005, pp. 2029–2034. DOI: 10.1109/IROS.2005.1545504.

[105] D. Kaneishi, R. P. Matthew, and M. Tomizuka. "Characterization of Active/Passive Pneumatic Actuators for Assistive Devices". In: *Proc. IEEE/RSJ Int. Conf. on Intelligent Robots and Systems (IROS)*. Oct. 2018.

[106] D. Kaneishi et al. "A SemiActive Control Method for Pneumatic Actuators with Evolutionary Algorithm". In: *Proc. IEEE Int. Conf. on Soft Robotics (RoboSoft)*. Apr. 2019, pp. 428–433.

[107] D. Kaneishi, R. P. Matthew, and M. Tomizuka. "Active/Passive Switching Control Framework for Assistive Devices with Variable Stiffness Actuator". In: *Proc. American Control Conf. (ACC)*. July 2019, pp. 5240–5246.

[108] D. Kaneishi, R. P. Matthew, and M. Tomizuka. "Optimal Control Parameterization for Active/Passive EXoskeleton with Variable Impedance Actuator". In: *Proc. IEEE RAS & EMBS Int. Conf. on Biomedical Robotics and Biomechatronics (BioRob)*. 2018, pp. 713–719.

[109] D. Kaneishi, R. P. Matthew, and M. Tomizuka. "A sEMG Classification Framework with Less Training Data". In: *Proc. Int. Conf. of the IEEE Engineering in Medicine and Biology Society (EMBC)*. July 2018, pp. 1680–1684. DOI: 10.1109/EMBC.2018.8512623.

[110] R. P. Matthew et al. "Initial investigation into the effect of an Active/Passive exoskeleton on hammer curl performance in healthy subjects". In: *Proc. Int. Conf. of the IEEE Engineering in Medicine and Biology Society (EMBC)*. Aug. 2015, pp. 3607–3610. DOI: 10.1109/EMBC.2015.7319173.

[111] M. Taghizadeh, A. Ghaffari, and F. Najafi. "Modeling and identification of a solenoid valve for PWM control applications". In: *Comptes Rendus Mecanique* 337.3 (2009), pp. 131–140. ISSN: 1631-0721. DOI: https://doi.org/10.1016/j.crme.2009.03.009.

[112] Rainer Storn and Kenneth Price. "Differential Evolution - A Simple and Efficient Heuristic for global Optimization over Continuous Spaces". In: *J. of Global Optimization* 11.4 (Dec. 1997), pp. 341–359. ISSN: 1573-2916. DOI: 10.1023/A:1008202821328.

[113] M. S. Saad, Hishamuddin Jamaluddin, and Intan Z. Mat Darus. "PID Controller Tuning Using Evolutionary Algorithms". In: *WSEAS Trans. on Systems and Control* 7.4 (2012), pp. 139–149. ISSN: 2224-2856.

[114] Robert Peter Matthew et al. "Optimal Design for Individualised Passive Assistance". In: *Proc. Int. Conf. on Augmented Human (AH)*. AH '15. Singapore, Singapore: ACM, 2015, pp. 69–76. ISBN: 978-1-4503-3349-8. DOI: 10.1145/2735711.2735793.

[115] X. Sun et al. "Variable Transmission Series Elastic Actuator for Robotic Prosthesis". In: *2018 IEEE International Conference on Robotics and Automation (ICRA)*. May 2018, pp. 2796–2803. DOI: 10.1109/ICRA.2018.8460796.

[116] Brian Armstrong-Hélouvry, Pierre Dupont, and Carlos Canudas De Wit. "A survey of models, analysis tools and compensation methods for the control of machines with friction". In: *Automatica* 30.7 (1994), pp. 1083–1138. ISSN: 0005-1098. DOI: https://doi.org/10.1016/0005-1098(94)90209-7. URL: http://www.sciencedirect.com/science/article/pii/0005109894902097.

[117] John Lygeros, Shankar Sastry, and Claire Tomlin. "Hybrid Systems: Modeling, Analysis and Control". In: (Feb. 2012). checked on 2018/09/09. URL: https://inst.eecs.berkeley.edu/$%5Csim$ee291e/sp18/.

[118] Y Liu et al. "On a class of optimal control problems with state jumps". In: *J. of Optimization Theory and Applications* 98.1 (1998), pp. 65–82.

[119] Kok Lay Teo, C Goh, and K Wong. *A unified computational approach to optimal control problems*. Longman Scientific & Technical, 1991.

[120] Qun Lin, Ryan Loxton, and Kok L Teo. "The control parameterization method for nonlinear optimal control: A survey". In: *J. of Industrial & Management Optimization* 10 (2014), p. 275. ISSN: 1547-5816. DOI: 10.3934/jimo.2014.10.275.

[121] S. Arimoto, S. Kawamura, and F. Miyazaki. "Bettering operation of Robots by learning". In: *J. Robotic Syst.* 1.1 (1984), pp. 123–140.

[122] Tomizuka M. "Zero Phase Error Tracking Algorithm for Digital Control". In: *ASME. J. Dyn. Sys., Meas., Control* 109.1 (1987), pp. 65–68.

[123] K. Ohnishi, M. Shibata, and T. Murakami. "Motion control for advanced mechatronics". In: *IEEE/ASME Transactions on Mechatronics* 1.1 (Mar. 1996), pp. 56–67. ISSN: 1083-4435. DOI: 10.1109/3516.491410.

[124] Yuya Matsumoto et al. "Development of an Exoskeleton to Support Eating Movements in Patients with Essential Tremor". In: *Journal of Robotics and Mechatronics* 25.6 (2013), pp. 949–958. DOI: 10.20965/jrm.2013.p0949.

[125] Yuya Matsumoto et al. "Development of an elbow-forearm interlock joint mechanism toward an exoskeleton for patients with essential tremor". In: *Proc. IEEE/RSJ Int. Conf. on Intelligent Robots and Systems (IROS)*. IEEE. 2014, pp. 2055–2062.

[126] Lawrence E Carlson, Bradley D Veatch, and Daniel D Frey. "Efficiency of prosthetic cable and housing". In: *J. of Prosthetics and Orthotics (JPO)* 7.3 (1995), pp. 96–99.

[127] Dongyang Chen, Youngmok Yun, and Ashish D Deshpande. "Experimental characterization of bowden cable friction". In: *Proc. IEEE Int. Conf. on Robotics and Automation (ICRA)*. IEEE. 2014, pp. 5927–5933.

[128] D. J. Bennett et al. "Time-varying stiffness of human elbow joint during cyclic voluntary movement". In: *Experimental Brain Research* 88.2 (Feb. 1992), pp. 433–442. ISSN: 1432-1106. DOI: 10.1007/BF02259118. URL: https://doi.org/10.1007/BF02259118.

[129] Donald L. Bartel, Dwight T. Davy, and Tony M. Keaveny. *Orthopaedic Biomechanics: Mechanics and Design in Musculoskeletal Systems*. Pearson, 2007. ISBN: 978-0130089090.

[130] Robert Peter Matthew et al. "Calculating reachable workspace volume for use in quantitative medicine". In: *European Conf. on Computer Vision*. Springer. 2014, pp. 570–583.

[131] Gentiane Venture, Ko Ayusawa, and Yoshihiko Nakamura. "Real-time identification and visualization of human segment parameters". In: *Proc. Int. Conf. of the IEEE Engineering in Medicine and Biology Society (EMBC)*. IEEE. 2009, pp. 3983–3986.

[132] George I. Zahalak. "Modeling Muscle Mechanics (and Energetics)". In: *Multiple Muscle Systems: Biomechanics and Movement Organization*. Ed. by Jack M. Winters and Savio L-Y. Woo. New York, NY: Springer New York, 1990, pp. 1–23. ISBN: 978-1-4613-9030-5. DOI: 10.1007/978-1-4613-9030-5_1. URL: https://doi.org/10.1007/978-1-4613-9030-5_1.

[133] Thalmic Labs. Feb. 2018, retrieved. URL: https://www.myo.com/.

[134] Seniam. *Recommendations for sensor locations in shoulder or neck muscles*. Feb. 2019, retrieved. URL: http://seniam.org/shoulder_location.htm.

[135] M. Rossi et al. "Preliminary results toward a naturally controlled multi-synergistic prosthetic hand". In: *2017 International Conference on Rehabilitation Robotics (ICORR)*. July 2017, pp. 1356–1363. DOI: 10.1109/ICORR.2017.8009437.